University of California
Santa Barbara

# Nonuniform buckled beam energy harvesting: experimental validation, modeling, and dynamic analysis

A dissertation submitted in partial satisfaction
of the requirements for the degree

Doctor of Philosophy
in
Mechanical Engineering

by

Louis Van Blarigan

Committee in charge:

Jeff Moehlis (Advisor), Chair
Robert McMeeking (Committee Member)
Igor Mezic (Committee Member)
Brad Paden (Committee Member)
Katie Byl (Committee Member)

June 2016

The Dissertation of Louis Van Blarigan is approved.

---

Robert McMeeking (Committee Member)

---

Igor Mezic (Committee Member)

---

Brad Paden (Committee Member)

---

Katie Byl (Committee Member)

---

Jeff Moehlis (Advisor), Committee Chair

May 2016

Nonuniform buckled beam energy harvesting: experimental validation, modeling, and dynamic analysis

Copyright © 2016

by

Louis Van Blarigan

# Acknowledgements

I would like to acknowledge the enduring patience of my wife and children, and my advisor's eternal understanding of balancing the challenges of combining academic study with family life.

I would also like to acknowledge the supporting help of many along the way, Bob McMeeking helped me understand the fundamentals of solid mechanics which proved invaluable in producing a model of this system. Dave Bothman and Kirk Fields were of assistance on many occasions, and especially when I found myself in need of a new lab space during the middle of a set of experiments. Kim Turner for allowing me to use her lab space, and for taking the heat when other building occupants expressed concern.

# Curriculum Vitæ
Louis Van Blarigan

## Education

| | |
|---|---|
| 2016 | Ph.D. in Mechanical Engineering (Expected), University of California, Santa Barbara. |
| 2011 | B.S. in Mechanical Engineering, University of California, Santa Barbara. |

## Publications

A broadband vibrational energy harvester.
L. Van Blarigan, P. Danzl, J. Moehlis
*App. Phys. Lett.* 100,253904: 2012.

Series-elastic actuation prototype for rough terrain hopping.
K. Byl, M. Byl, M. Rutschmann, B. W. Satzinger,L. Van Blarigan, J. Cortell.
*TePRA* 2012: 103-110.

Low dimensional modeling of a non-uniform, buckled piezoelectric beam for vibrational energy harvesting.
L. Van Blarigan, J. Moehlis, R. McMeeking.
*Smart Mater. Struct* 24,065012: 2015.

Dynamic analysis of a buckled asymmetric piezoelectric beam for energy harvesting.
L. Van Blarigan, J. Moehlis.
*Chaos* 26,033107: 2016.

**Abstract**

Nonuniform buckled beam energy harvesting: experimental validation, modeling, and dynamic analysis

by

Louis Van Blarigan

Vibrational energy harvesting is a subject that has received much attention as a possible replacement for remote battery-operated sensor networks. We describe a vibrational energy harvester with an asymmetric buckled beam which is constructed out of commercially available components, and has demonstrated a significantly increased bandwidth compared to a device exhibiting linear resonance. This particular beam could not be mathematically modeled by existing analytic techniques, so a method is developed to produce a reduced order analytic model based on a finite element representation of the system. Moreover, we present an argument for why common single-mode Galerkin projection models are incapable of accurately reproducing snap-through behavior at higher than infinitesimal buckling levels. The model developed here demonstrates good agreement with the behavior exhibited by the experimental system around the parameter region of high power output, as evidenced by similar phase portraits and frequency response plots. Further, an argument is presented for why current trends towards testing non-linear systems with constant acceleration frequency sweeps are misleading, and an alternative comparison platform is suggested. The model is analyzed from a dynamical systems perspective, and it is shown that the transitions between high and low power output can be associated with a period doubling cascade or a boundary crisis where a chaotic attractor stabilizes through an intermittency transition. Chaotic behavior is observed to be closely related to the high power output region, but it is possible to have

appreciable power output with a periodic response. Potential future work involves analyzing alternate beam configurations in search of an *optimal* solution to the high power output bandwidth problem.

# Contents

**Curriculum Vitae** **v**

**Abstract** **vi**

**1 Introduction** **1**

**2 Background** **7**
2.1 Basics of Piezoelectricity . . . . . 7
2.2 Solid Mechanics . . . . . 11
2.3 Beam Development . . . . . 19

**3 Experimental Demonstration** **22**
3.1 Experimental Setup . . . . . 22
3.2 Experimental Results . . . . . 27
3.3 Further Experimental Exploration . . . . . 32

**4 Modeling** **36**
4.1 Analytic Attempts . . . . . 36
4.2 Finite Element Representation . . . . . 44
4.3 Energy Projection . . . . . 48
4.4 EOM and Testing . . . . . 56
4.5 Comparison with Experimental Results . . . . . 60

**5 Analysis of the Model** **64**
5.1 Bifurcation Diagrams . . . . . 67
5.2 Periodic Windows . . . . . 72
5.3 Wideband Forcing . . . . . 75

**6 Conclusions and Future Work** **79**

**A Finite Element Setup Process** **81**

**B Labview** **84**
B.1 Power Level Adjustment Controller . . . . . 84
B.2 Raw Data Collection . . . . . 87
B.3 Amplitude Extraction Program . . . . . 88

**C Model Matrices** **89**
C.1 "b" matrix . . . . . 89
C.2 "d" vector . . . . . 90
C.3 "h" vector . . . . . 90

**D Mathematica** **91**
D.1 Mathematica EOM . . . . . 91

**E Matlab programs** **107**
E.1 FEA integral computation . . . . . 107
E.2 Model Time Simulation . . . . . 110

**Bibliography** **113**

# Chapter 1

# Introduction

There are many environmental situations where energy is wasted in the form of vibrations. These vibrations can be due to imperfect mechanical parts, resonances in otherwise rigid structures, or as a result of ambient non-linear phenomena such as friction and slippage. Often, the primary consideration is eliminating the source of the vibration, but this may require excessive time and cost to realize, leading to diminishing returns where rising costs associated with eliminating undesired vibrations outweigh potential benefits. In other words, a practicing engineer performs reasonable actions to prevent the vibrations, but realizes that we are going to have to live with them to some extent. As a result, ambient vibrations can be found in many situations, particularly in proximity to moving mechanical structures.

Operation of these structures often demands a method of monitoring activity either for control or upkeep purposes. Electrical control and monitoring devices have traditionally required a power source, which means either using batteries which must be regularly replaced, or investing in wiring to supply all electrical devices. Recent advances in wireless low power electrical systems have produced a situation where providing power becomes a major challenge and expense. In response to this need, vibrational energy

harvesting devices are able to provide power without the need for batteries or wires, and simply require an ambient vibration source to provide power for milliamp-level electronics. Examples of this sort of system are abundant: retrofitting old airplanes with new sensors without removing the fragile aluminum skin, monitoring processes at large scale industrial facilities, remote sensing capabilities, etc..

While vibrational energy harvesting may seem to be an easy answer to this need to retrofit old systems with new sensors, conversion from vibrational energy to electrical energy is not without challenges. An abundance of devices have been proposed, commonly using electrical magnets and coils to produce electrical current [1], or using deformation of piezoelectric materials to generate charge separation which can be gathered with intelligently placed electrodes and stored as electrical energy. To date, piezoelectric devices have demonstrated the highest level of coupling [2, 3, 4], and show promise as the vibrational energy harvesting mechanism of the future. Further challenges include development of a device that is capable of harvesting energy from a broad range of mechanical excitations, and storage of converted energy for future use. The most basic piezoelectric energy harvester consists of a cantilevered beam which is allowed to resonate at a frequency contained within the ambient spectrum. This method produces good results if the ambient vibration has a large component at the resonant frequency of the beam, but power generation falls off quickly as the difference between the resonant frequency of the cantilever and the forcing frequency increases. Ambient vibrations commonly have a time-varying aspect, or a relatively broad range of frequencies of excitation, and it can be difficult to find a situation where an energy harvester is capable of performing under all likely situations.

This is a common problem among energy harvesters designed to take advantage of a resonance, and extensive research has been done to determine how to expand the range of frequencies over which an energy harvesting device is functional. One method for

increasing the bandwidth is to incorporate a "hardening" response in the material [5, 6, 7, 8, 9, 10, 11, 12], which can create a situation where there is a stable high amplitude branch which spans a significantly wider frequency range than a linear resonance. However, there is also a co-existing stable low amplitude branch [13, 14], and the initial conditions of the system determine which branch will be reached as a stable long-term solution. Another method is to use impact nonlinearities to produce a frequency up-conversion property for a linear resonator [15, 16, 17]. The concept here is that an impact phenomenon has frequency content that overlaps with the resonant frequency, and therefore a frequency mismatch between the forcing and resonant frequencies results in a transient resonance from which some energy can be harvested. A third method for expanding the bandwidth of energy harvesting devices is to design with a double well potential such that high energy transitions between wells can occur [11, 18, 19, 20, 21, 22, 23, 24, 25, 26, 27, 28, 29, 30, 31]. A preferred method for realizing this double well potential is buckling a beam, although this method has a drawback in the fact that if the forcing doesn't contain enough power to cause transitions between wells, the amount of power that can be extracted is extremely small [32]. Several different methods for reducing the power barrier to snap-through behavior have been proposed, such as attaching a mass to the center of the buckled beam [30, 33]. Also considered are systems consisting of multiple resonant devices which have various resonant frequencies in the expected range of forcing frequency content [33, 34, 35, 36]. A final method for increasing bandwidth is to design the system with an *essential nonlinearity* such that the linear stiffness vanishes and the behavior is dictated by a cubic stiffness term [37].

Previous work done in the field of piezoelectric energy harvesting has deeply explored the applications of linear cantilever resonance [38] under conditions of both stochastic and single frequency excitations, including explorations of non-linearities associated with material phenomena and lumped parameter models. Comparatively, there has been few

attempts to produce mathematical models that recreate the complex dynamics associated with piezoelectric snap-through behavior [33, 39]. Modeling of buckled beams with the goal of reproducing snap-through behavior has been extensively examined in [40, 41], and resulted in an analytic model which was capable of recreating experimentally observed snap-through behavior. This method involves finding the buckled equilibrium position and calculating linear modes about this nonlinear operating point. These models require several modes to successfully recreate the snap-though effect. Utilization of this methodology has been sparse for piezoelectric buckled beams, but has been explored at buckling levels below the critical load, such that a double well potential does not exist [42], and where the piezoelectric effect on the beam is ignored [33]. Other researchers have utilized a single-mode Galerkin projection, which fails for several reasons [39, 43]. A single mode is incapable of properly recreating the equilibrium positions, and moreover at small but finite buckling levels this method violates the small strain approximation used in derivation of the model, as will be presented in Section 4.3.

In this document, we will examine the use of asymmetric buckled beams where one side of the device is much stiffer than the other side. This reduces the power barrier to snap-through behavior, and is a version of a method known to produce chaotic vibrations [13]. This concept has not been explored in the literature, but builds upon previous work and expands the field. The device will be motivated in Chapter 2.1, and experimentally demonstrated in Chapter 3. We will then proceed to examine the application of buckled beam modeling techniques as developed by Nayfeh et al. in Section 4.1. However, the complexity of this design produces a system of equations which is analytically intractable, and direct application fails. To overcome this obstacle, we are required to generate linear mode shapes and the respective equilibrium position via finite element modeling, which is done in the remainder of Chapter 4. The mode shapes are then combined with the principles of solid mechanics to construct an energy function where the independent

variables are the amplitudes of the mode shapes. An additional mode representing the amplitude of the equilibrium position is incorporated to allow the system to exist in either of the stable configurations, and to transition dynamically between them. A Lagrangian functional is used to create equations of motion for the beam subjected to single frequency excitation signals. This model will be validated experimentally in Section 4.5, and used to examine the regions where the beam produces significant power output in Chapter 5.

Several contributions to the understanding of how to model and analyze piezoelectric buckled beam energy harvesters have resulted from this work. A method has been developed to utilize finite element analysis about a nonlinear operating point to produce an analytic model appropriate for dynamic evaluation. Previously finite element methods have been utilized to identify resonant regions of nonlinear systems, but to our knowledge no one has successfully incorporated this information into an analytic model. This method results in a model which shows good subjective agreement with the experimental system in a regime where traditional modeling techniques are intractable. A mathematical argument demonstrating why a single mode projection violates the small strain approximation is presented, as this method has historically been used to derive buckled beam models of energy harvesting devices. Further, we have produced a dynamic analysis utilizing techniques such as bifurcation diagrams and numerical bifurcation analysis, which describes the transitions between single-well and double-well oscillations.

One of the major challenges faced by the nonlinear energy harvesting community is choosing the appropriate parameter space to produce meaningful comparisons between devices. Linear analysis techniques make use of the property of superposition to report frequency dependent *gain* as the ratio of the output amplitude to the amplitude of the acceleration of the forcing signal. This produces a description which is independent of the forcing amplitude and exposes the character of the underlying operator. However, there is no simple extension to nonlinear operator analysis. Frequently, claims about the

bandwidth of a nonlinear energy harvesting device are made based on forcing frequency sweeps with a constant acceleration amplitude. This results in different forcing power levels at different frequencies, and makes interpretation of the bandwidth dubious. We propose that the proper parameter space for these examinations is the forcing power level and frequency. Doing frequency sweeps with the power level fixed requires that the acceleration amplitude is varied with the frequency, but allows for a much more meaningful comparison between different power level sweeps.

# Chapter 2

# Background

## 2.1 Basics of Piezoelectricity

Piezoelectricity is a material property wherein charge separation and mechanical deformation are coupled. This effect was discovered in 1880 by the Curie brothers, when they deformed a crystal and were able to measure a voltage across the material. This is known as the *direct* piezoelectric effect. Alternatively, when an applied voltage causes a deformation of the material, it is known as the *converse* piezoelectric effect. These effects typically occur simultaneously, and must be considered together to form a complete picture of the interplay between charge separation and deformation.

Natural crystals exist which exhibit the piezoelectric effect at varying levels, but in the mid-1900's piezoelectric ceramics were developed which exhibit a much higher coupling constant than natural materials. The most commonly used piezoelectric ceramic material is known as lead zirconium titanate, or PZT, which exists in several forms, most notably PZT-5H and PZT-5A. Continued use of piezoelectrics in both sensor and actuator roles led to development of the IEEE Standard on Piezoelectricity [44]. Piezoelectric materials are manufactured by depositing a bulk layer of randomly poled material, and applying

an electric field to the material which causes the poles to align with the electric field. As a result the coupling constants are assigned in relation to the direction of poling. The 1 and 2 directions are perpendicular to the poling direction, and the 3 direction is parallel to the poling. In general, poled piezoelectric materials are transversely isotropic in the 12-plane, and therefore exhibit symmetry about the 3-axis, or the poling direction.

Using electrodes attached to the surface of a piezoelectric material, it is possible to measure voltages produced by deformation, or to induce a deformation by applying a potential. Some of the energy stored in the beam configuration can be harvested by placing a load between the electrodes and allowing any accumulated electrical potential to dissipate. The orientation of the electrodes in relation to the poling direction has a direct effect on the efficiency of conversion. The highest coupling between strain and charge separation occurs in the 1-5 direction, meaning that we are causing a shear stress and placing our electrodes in the 1 direction, or perpendicular to the poling direction. While this is the largest coupling, it is not a practical way to use piezoelectric devices and is not utilized for energy harvesting. The next highest coupling is in the 1-3 direction, where the beam is being strained in the poling direction (3) and electrodes are placed perpendicular to this direction. In a beam this can be interpreted as strain in the axial direction and electrodes placed on the top and bottom of the beam. The lowest coupling occurs in the 3-3 mode, where the electrodes are placed in the same direction as the poling. This is the easiest arrangement to produce as the same electrodes can be used for poling the raw material and for the sensing of charge separation. In this document we will be examining piezoelectric beams in the 1-3 configuration to utilize the increased coupling compared to the more readily constructed 3-3 configuration.

For any bounded piezoelectric volume, the rate of increase of energy is the rate at which work is done by surface tractions minus the flux of electric energy across the surface [45]. Under assumptions of infinitesimal strain, linear elasticity, and the absence of

electric body force and coupling, we arrive at what is known as the first law of thermodynamics for the piezoelectric medium [38]:

$$\dot{U} = T_{ij}\dot{S}_{ij} + E_i\dot{D}_i,$$

where $U$ is the stored energy density, $T$ is the stress, $S$ is the strain, $E$ is the electric field, and $D$ is the electric displacement. We have utilized the dot notation to represent a time derivative and indices imply Einstein summation. This allows the electric enthalpy density ($H$) to be defined for a linear piezoelectric medium as

$$H = \frac{1}{2}c^E_{ijkl}S_{ij}S_{kl} - e_{kij}E_kS_{ij} - \frac{1}{2}\varepsilon^S_{ij}E_iE_j,$$

where $c^E_{ijkl}$ gives the elastic constants at constant electric field, $e_{kij}$ gives the piezoelectric constants, and $\varepsilon^S_{ij}$ is the permittivity evaluated at constant strain. Noting that the stress and electric displacement tensors can be derived from the electric enthalpy density as $T_{ij} = \frac{\partial H}{\partial S_{ij}}$ and $D_i = -\frac{\partial H}{\partial E_i}$, and the relation $\frac{\partial S_{ij}}{\partial S_{ji}} = \delta_{ij}$, where $\delta_{ij}$ is the Kronecker delta function, we arrive at

$$T_{ij} = c^E_{ijkl}S_{kl} - e_{kij}E_k, \tag{2.1}$$

$$D_i = e_{ikl}S_{kl} + \varepsilon^S_{ik}E_k. \tag{2.2}$$

This can also be represented in expanded matrix form as

$$\begin{bmatrix} T_1 \\ T_2 \\ T_3 \\ T_4 \\ T_5 \\ T_6 \\ D_1 \\ D_2 \\ D_3 \end{bmatrix} = \begin{bmatrix} c_{11}^E & c_{12}^E & c_{13}^E & 0 & 0 & 0 & 0 & 0 & e_{31} \\ c_{12}^E & c_{11}^E & c_{13}^E & 0 & 0 & 0 & 0 & 0 & e_{31} \\ c_{13}^E & c_{13}^E & c_{33}^E & 0 & 0 & 0 & 0 & 0 & e_{33} \\ 0 & 0 & 0 & c_{55}^E & 0 & 0 & 0 & e_{15} & 0 \\ 0 & 0 & 0 & 0 & c_{55}^E & 0 & e_{15} & 0 & 0 \\ 0 & 0 & 0 & 0 & 0 & c_{66}^E & 0 & 0 & 0 \\ 0 & 0 & 0 & 0 & e_{15} & 0 & \varepsilon_{11}^S & 0 & 0 \\ 0 & 0 & 0 & e_{15} & 0 & 0 & 0 & \varepsilon_{11}^S & 0 \\ e_{31} & e_{31} & e_{33} & 0 & 0 & 0 & 0 & 0 & \varepsilon_{33}^S \end{bmatrix} \begin{bmatrix} S_1 \\ S_2 \\ S_3 \\ S_4 \\ S_5 \\ S_6 \\ E_1 \\ E_2 \\ E_3 \end{bmatrix} \tag{2.3}$$

where the symmetries of the transversely isotropic material behavior have been directly applied.

In a structure modeled as a thin beam based on Euler-Bernoulli beam theory, the stress components other than the one dimensional bending stress are negligible, and placing the electrodes perpendicular to the poling direction, as with the beams used in this document, we find the reduced piezoelectric constitutive equations to be [38]

$$\begin{bmatrix} T_1 \\ D_3 \end{bmatrix} = \begin{bmatrix} c_{11}^E & -\bar{e}_{31} \\ \bar{e}_{31} & \bar{\varepsilon}_{33}^S \end{bmatrix} \begin{bmatrix} S_1 \\ E_3 \end{bmatrix}, \tag{2.4}$$

where $\bar{e}_{31} = \frac{d_{31}}{s_{11}^E}$ and $\bar{\varepsilon}_{33}^S = \varepsilon_{33}^T - \frac{d_{31}^2}{s_{11}^E}$.

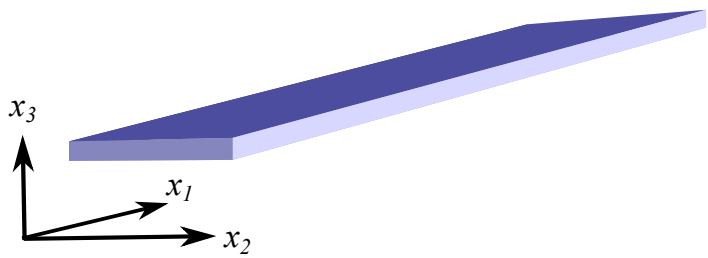


Figure 2.1: Representative beam with primary directions indicated. Here $x_1$ is associated with the length of the beam, $x_2$ is the width, and $x_3$ is the thickness.

## 2.2 Solid Mechanics

### 2.2.1 Beam Applications

Here the term *beam* is used to denote a slender rectangular parallelepiped in which the dimensions, denoted $X_1$, $X_2$, and $X_3$, satisfy

$$X_1 \gg X_2 \gg X_3, \tag{2.5}$$

as seen in Figure 2.1. The beam material will be assumed to be homogeneous and linearly elastic, in accordance with Hooke's law. The bending stiffness of a beam is proportional to the area moment of inertia, denoted

$$I = \iint_A p^2 \, \mathrm{d}A. \tag{2.6}$$

Beams considered in this examination will all be of rectangular shape and cross section, with the centroid located at the geometrical center of the cross section. Thus the two

bending stiffnesses of the beam are proportional to

$$I_{X_1} = \frac{X_2^3 \cdot X_3}{12}, \tag{2.7}$$

$$I_{X_2} = \frac{X_2 \cdot X_3^3}{12}, \tag{2.8}$$

$$X_2 \gg X_3 \implies I_{X_2} \gg I_{X_1}. \tag{2.9}$$

From this it is clear that the beam dimensions make bending much more likely about the $x_2$ axis. Therefore the beam can be reduced to a cross section in the $x_1$-$x_3$ plane, and we will assume that all motions remain in plane and motions out of plane are negligible. Also, we will denote displacements in the $x_1$ direction as $u$, and displacements in the $x_3$ direction as $w$. All derivations will follow the methods of [46].

### 2.2.2 Strain Tensor Derivation

Consider a line segment designated $d\underline{X}$ that runs from point $P$ to point $Q$, as shown in Figure 2.2. This line undergoes an arbitrary stretch and translation, resulting in the new deformed line segment running from $P'$ to $Q'$ denoted $d\underline{x}$. The length of segment $d\underline{X}$ is $dS = \sqrt{d\underline{X} \cdot d\underline{X}}$, while the length of segment $d\underline{x}$ is $ds = \sqrt{d\underline{x} \cdot d\underline{x}}$. We will denote the deformation gradient as $\underline{F}$, which maps $d\underline{X}$ into $d\underline{x}$:

$$d\underline{x} = \underline{F} \cdot d\underline{X}. \tag{2.10}$$

Therefore the length of line segment $d\underline{x}$ can be written

$$ds^2 = d\underline{X} \cdot \underline{F}^T \cdot \underline{F} \cdot d\underline{X}. \tag{2.11}$$

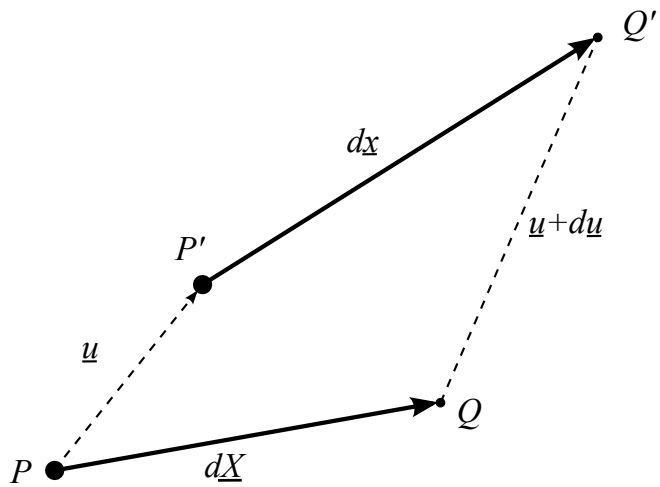


Figure 2.2: Deformation of a line segment.

We define the stretch ratio $\lambda$ as the ratio between the final length and the initial length,

$$\lambda = \frac{ds}{dS}, \tag{2.12}$$

or using (2.11),

$$\lambda^2 = \frac{d\underline{X} \cdot \underline{F}^T \cdot \underline{F} \cdot d\underline{X}}{dS^2} = \underline{N} \cdot \underline{F}^T \cdot \underline{F} \cdot \underline{N}, \tag{2.13}$$

where $\underline{N} = \frac{d\underline{X}}{dS}$ is the unit vector in the pre-deformed configuration. To maintain consistency with methods used to determine the engineering strain, we will define the strain $E$ as

$$E = \frac{1}{2}\left(\lambda^2 - 1\right), \tag{2.14}$$

which leads to

$$E = \frac{1}{2}\left(\underline{F}^T \cdot \underline{F} - \underline{I}\right), \tag{2.15}$$

where $\underline{I}$ is the identity matrix. This strain formulation is known as the Green-Lagrange strain tensor. In Cartesian coordinates it can be written

$$E_{ij} = \frac{1}{2}\left(F_{ki}F_{kj} - \delta_{ij}\right) = \frac{1}{2}\left(\frac{\partial u_i}{\partial X_j} + \frac{\partial u_j}{\partial X_i} + \frac{\partial u_k}{\partial X_i}\frac{\partial u_k}{\partial X_j}\right), \tag{2.16}$$

which under the basic beam assumptions laid out in the previous section can be reduced to

$$E_{11} = \frac{\partial u}{\partial X_1} + \frac{1}{2}\left(\frac{\partial u}{\partial X_1}\right)^2 + \frac{1}{2}\left(\frac{\partial w}{\partial X_1}\right)^2. \tag{2.17}$$

Figure 2.3 shows a cartoon depicting the behavior of a beam of non-negligible thickness under a bending deformation. Note that $z$ is the distance between the central axis of the beam and the point of interest. We will denote the bending tensor as $\underline{M}$, which is of unit length:

$$\underline{M} \cdot \underline{M} = 1, \tag{2.18}$$

$$\underline{M} = \cos\theta \underline{j} - \sin\theta \underline{i}, \tag{2.19}$$

where $\underline{i}$ and $\underline{j}$ are the unit vector in directions $x_1$ and $x_3$, respectively. We can proceed to define the trigonometric properties of the angle $\theta$:

$$\tan\theta = \frac{dy}{dx}, \tag{2.20}$$

$$\sin\theta = \frac{\frac{dy}{dx}}{\sqrt{1 + \left(\frac{dy}{dx}\right)^2}}, \tag{2.21}$$

$$\cos\theta = \frac{1}{\sqrt{1 + \left(\frac{dy}{dx}\right)^2}}. \tag{2.22}$$

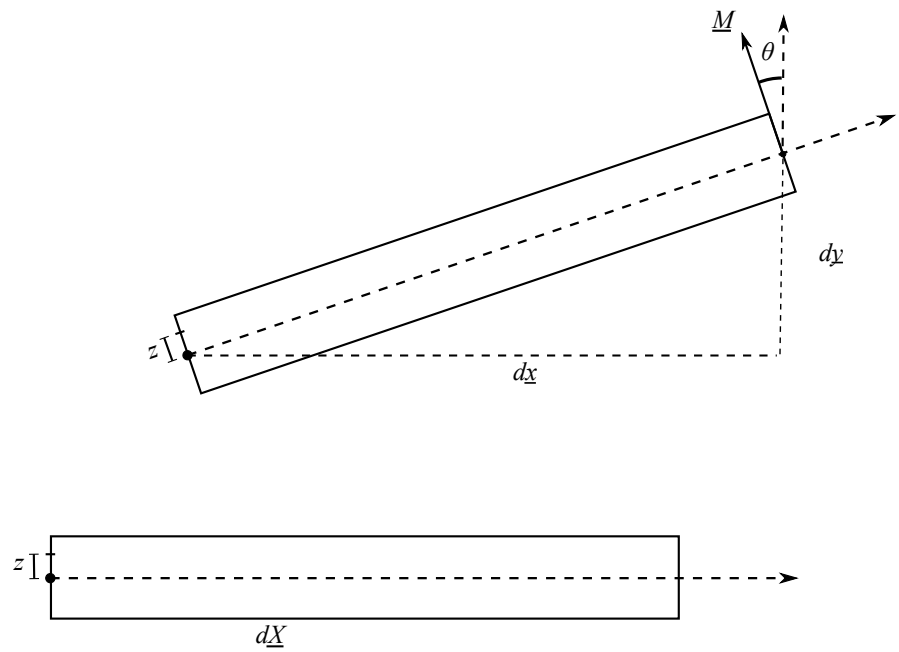


Figure 2.3: Beam subjected to bending moment.

This leaves us with

$$\underline{M} = \frac{\underline{j} - \frac{dy}{dx}\underline{i}}{\sqrt{1 + \left(\frac{dy}{dx}\right)^2}}. \tag{2.23}$$

Now we examine what effect this has on the axial displacement when removed from the neutral axis of the beam by a distance $z$,

$$u = u_0 - \frac{\frac{dw_0}{dX} \cdot z}{\sqrt{1 + \left(\frac{dw_0}{dX}\right)^2}}, \tag{2.24}$$

where we have assumed that $dx \approx dX$. Differentiating with respect to the spatial coordinate $X$,

$$\frac{\partial u}{\partial X} = \frac{\partial u_0}{\partial X} - \frac{\frac{d^2 w_0}{dX^2} \cdot z}{\sqrt{1 + \left(\frac{dw_0}{dX}\right)^2}} + \frac{\left(\frac{dw_0}{dX}\right)^2 \frac{d^2 w_0}{dX^2} \cdot z}{\left[1 + \left(\frac{dw_0}{dX}\right)^2\right]^{\frac{3}{2}}}. \tag{2.25}$$

Here the second term on the right hand side of the equation is representative of the radius of curvature of the beam, denoted as $\kappa$. Under a small strain approximation, we can conclude that the last term is much smaller than the second term and can therefore be assumed negligible, and the denominator of the second term will be very close to unity, leaving us with

$$\frac{\partial u}{\partial X} \approx \frac{\partial u_0}{\partial X} - \frac{d^2 w_0}{dX^2} \cdot z, \tag{2.26}$$

which can be substituted into (2.17) to provide a complete description of the axial strain in the beam.

### 2.2.3 Beam PDE

We will now proceed to derive the partial differential equation that governs the beam's motion under assumptions of small strain and small axial load. The kinetic energy ($T$) of a differential element of the beam is

$$dT = \frac{1}{2} m \left( \frac{\partial w}{\partial t} \right)^2 \mathrm{d}x, \tag{2.27}$$

where $m$ is the mass per unit length of the beam. Integrating over the domain of the beam, we arrive at

$$T = \frac{1}{2} m \int_0^L \left( \frac{\partial w}{\partial t} \right)^2 \mathrm{d}x. \tag{2.28}$$

Calculating the potential energy requires accounting for the axial deformation, bending moment, and axial load. By integrating (2.26) over the domain of the beam, we gain a measure of the midplane stretch ($\Delta$):

$$\Delta = u(L) - u(0) + \frac{1}{2} \int_0^L \left( \frac{\partial w}{\partial x} \right)^2 \mathrm{d}x. \tag{2.29}$$

Here we will assume that since the ends of the beam are fixed, $u(L) - u(0) \approx 0$ allowing us to reduce to

$$\Delta \approx \frac{1}{2} \int_0^L \left( \frac{\partial w}{\partial x} \right)^2 \mathrm{d}x. \tag{2.30}$$

The axial stiffness of the beam is calculated as $^{EA}/_{L}$, which can be combined with the midplane stretch and the axial stiffness to produce the induced axial force:

$$S = \frac{EA}{2L} \int_0^L \left( \frac{\partial w}{\partial x} \right)^2 \mathrm{d}x. \tag{2.31}$$

The bending moment $M$ is given by the flexural rigidity of the beam $E \cdot I$, multiplied with the radius of curvature $\kappa$, which we calculated in the previous section as having a contribution from the second derivative of the transverse displacement:

$$\kappa \approx \frac{\partial^2 w}{\partial x^2}. \tag{2.32}$$

Therefore the potential energy $V$ due to bending is calculated as

$$V_b = \frac{1}{2} \int_0^L M \, \kappa \, \mathrm{d}x \tag{2.33}$$

$$= \frac{EI}{2} \int_0^L \left( \frac{\partial^2 w}{\partial x^2} \right)^2 \mathrm{d}x. \tag{2.34}$$

The energy contribution due to the axial force $P$ is given by

$$V_p = P\Delta \tag{2.35}$$

$$= \frac{P}{2} \int_0^L \left( \frac{\partial w}{\partial x} \right)^2 \mathrm{d}x. \tag{2.36}$$

The contribution from midplane stretch is

$$V_s = \frac{1}{2} S \Delta \tag{2.37}$$

$$= \frac{EA}{8L} \left[ \int_0^L \left( \frac{\partial w}{\partial x} \right)^2 \mathrm{d}x \right]^2 . \tag{2.38}$$

This allows the full potential energy to be written as

$$V = \frac{EI}{2} \int_0^L \left( \frac{\partial^2 w}{\partial x^2} \right)^2 \mathrm{d}x - \frac{P}{2} \int_0^L \left( \frac{\partial w}{\partial x} \right)^2 \mathrm{d}x + \frac{EA}{8L} \left[ \int_0^L \left( \frac{\partial w}{\partial x} \right)^2 \mathrm{d}x \right]^2 . \tag{2.39}$$

We can now use the Euler-Lagrange equations to derive the governing PDE for this beam system. Recall that the Lagrangian is defined as the kinetic energy minus the potential energy,

$$\mathcal{L} = T - V \tag{2.40}$$

$$= \frac{1}{2} m \int_0^L \left( \frac{\partial w}{\partial t} \right)^2 \mathrm{d}x - \frac{EI}{2} \int_0^L \left( \frac{\partial^2 w}{\partial x^2} \right)^2 \mathrm{d}x + \frac{P}{2} \int_0^L \left( \frac{\partial w}{\partial x} \right)^2 \mathrm{d}x - \frac{EA}{8L} \left[ \int_0^L \left( \frac{\partial w}{\partial x} \right)^2 \mathrm{d}x \right]^2 . \tag{2.41}$$

The stationary values of this functional define the governing equations for the system by Hamilton's principle of stationary action. These stationary functions can be obtained from the Euler-Lagrange equation defined by [47]

$$\frac{\partial \mathcal{L}}{\partial f} + \sum_{i=1}^{n} (-1)^i \frac{\partial^i}{\partial x_{\mu_1} \ldots \partial x_{\mu_i}} \left( \frac{\partial \mathcal{L}}{\partial f_{,\mu_1 \ldots \mu_i}} \right) = 0, \tag{2.42}$$

$$f_{,i} \equiv \frac{\partial f}{\partial x_i}, \tag{2.43}$$

$$f_{,ij} \equiv \frac{\partial^2 f}{\partial x_i \partial x_j}, \tag{2.44}$$

where $\mu$ indices employ Einstein notation. For our problem this can be reduced to

$$-\frac{\partial}{\partial t}\left(\frac{\partial \mathcal{L}}{\partial \dot{w}}\right) - \frac{\partial}{\partial x}\left(\frac{\partial \mathcal{L}}{\partial w'}\right) + \frac{\partial^2}{\partial x^2}\left(\frac{\partial \mathcal{L}}{\partial w''}\right) = 0. \tag{2.45}$$

Applying (2.45) to (2.41) results in

$$\frac{\partial}{\partial t}\left(m\frac{\partial w}{\partial t}\right) + \frac{\partial}{\partial x}\left(P\frac{\partial w}{\partial x} - \frac{EA}{2L}\frac{\partial w}{\partial x}\int_0^L \left(\frac{\partial w}{\partial x}\right)^2 \mathrm{d}x\right) - \frac{\partial^2}{\partial x^2}\left(-EI\frac{\partial^2 w}{\partial x^2}\right) = 0, \tag{2.46}$$

or if we assume constant parameters throughout the beam,

$$m\frac{\partial^2 w}{\partial t^2} + P\frac{\partial^2 w}{\partial x^2} - \frac{EA}{2L}\frac{\partial^2 w}{\partial x^2}\int_0^L \left(\frac{\partial w}{\partial x}\right)^2 \mathrm{d}x + EI\frac{\partial^4 w}{\partial x^4} = 0, \tag{2.47}$$

which can be generalized to

$$m\frac{\partial^2 w}{\partial t^2} + P\frac{\partial^2 w}{\partial x^2} - \frac{EA}{2L}\frac{\partial^2 w}{\partial x^2}\int_0^L \left(\frac{\partial w}{\partial x}\right)^2 \mathrm{d}x + EI\frac{\partial^4 w}{\partial x^4} = q(x,t) - c\frac{\partial w}{\partial t}, \tag{2.48}$$

where $q(x,t)$ is a an arbitrary forcing function and the second term on the right hand side is a damping loss term.

## 2.3 Beam Development

Preliminary investigations of buckled piezoelectric beams for energy harvesting were based on easily available and inexpensive beams from Advanced Cerametrics [48]. It was presumed that by fixing a flexible beam in a buckled configuration and shaking, it would cause snap-through behavior where the beam oscillates between equilibrium wells, causing a relatively large amplitude oscillation which would presumably result in a relatively high power output from the beam. However, due to the symmetry of a buckled beam, one

| | Advanced Cerametrics | Measured |
|---|---|---|
| width | 14 mm | 10 mm |
| height | 0.3 mm | 0.4 mm |
| $^{\text{mass}}/_{\text{length}}$ | 0.014 $^{\text{kg}}/_{\text{m}}$ | 0.015 $^{\text{kg}}/_{\text{m}}$ |
| modulus | 24.4 GPa | 15.2 GPa |

Table 2.1: Provided and measured beam parameters.

half of the beam created a positive voltage, while the other half of the beam created an equal negative voltage, resulting in very little power output. Seeking to remedy this, the book *Chaotic Vibrations* by Frank Moon [13] was consulted, where it is indicated that a central mass with a spring on either side of different stiffness is a system that results in chaotic response to periodic inputs. It was suggested that a composite beam with different stiffnesses throughout the length would most likely result in chaotic behavior, while eliminating the symmetry that reduces power in one continuously electroded beam. The simplest configuration involved gluing a bimorph section beam to a single layer beam. Exploring this concept led to very promising experimental results, which are presented in the next section.

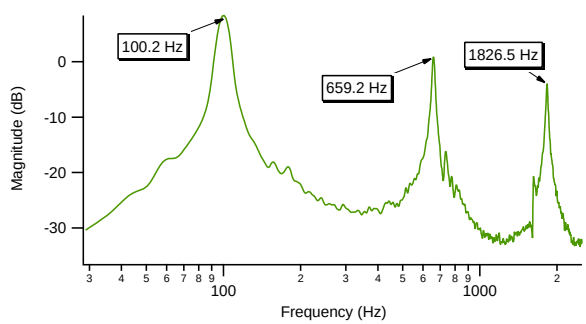


Figure 2.4: Frequency response of the voltage output of the bimorph beam, indicating resonance peaks from which material parameters can be extracted.

Experimental investigation of the beams began by ensuring that we could reproduce a model of the observed experimental behavior of a simple cantilever. However, the

| | Experimental (Hz) | FEA (Hz) | % error |
|---|---|---|---|
| mode 1 | 100.2 | 107.4 | 6.7 |
| mode 2 | 659.2 | 670.8 | 1.7 |
| mode 3 | 1826.5 | 1875.7 | 2.6 |

Table 2.2: Frequency comparison of experimental measurements and results from a finite element model of the beam using experimentally extracted parameters.

parameters provided by the manufacturer did not produce a model that was remotely reminiscent of the observed behavior. In order to assure agreement with our modeling attempts, we needed to make sure our material parameters were correct. This was done by statistical analysis of the bending of a single layer piezoelectric beam to extract the modulus of the material after having carefully measured the physical dimensions. Building on this foundation, we can check the bending stiffness of the bimorph beam, plug in the modulus of the piezoelectric portions, and extract the modulus of the steel shim. The extracted parameters are compared to the parameters provided by Advanced Cerametrics in Table 2.1. Now we can construct both analytic and finite element models from the established parameters and compare the predicted resonant peaks to the experimental data, as seen in Figure 2.4. The analytic results are very close by design of this experimental method, so we only show a comparison of the experimental and FEA results in Table 2.2.

# Chapter 3

# Experimental Demonstration

## 3.1 Experimental Setup

The experimental setup consists of a purpose built fixture mounted vertically on a shaker, which is driven by LabVIEW software. A cartoon of the fixture demonstrating the design intention is shown in Figure 3.1. This harvester uses two flexible ceramic piezoelectric elements from Advanced Cerametrics, Inc.: a single layer element (catalog #PFC-W14) and a bimorph element (catalog #PFCB-W14), each of which is 132 millimeters (mm) long and 14 mm wide, and 0.3 mm and 1.3 mm thick, respectively. The bimorph has two piezo layers separated by a core. The bimorph element has approximately 40 times the stiffness of the single layer element. The elements are bonded together as shown in the lower portion of Figure 3.1 with a 6 mm overlap, and the other ends fixed to an aluminum mount so that at equilibrium the single layer element is slightly buckled. Our harvesting results have proved to be robust to small changes in overlap length, overall length, and bimorph length, but is very sensitive to the amount of buckling. A picture of the actual fixture as used for these experiments is shown in Figure 3.2. Note that a stabilizing bar has been included in the actual device to move any

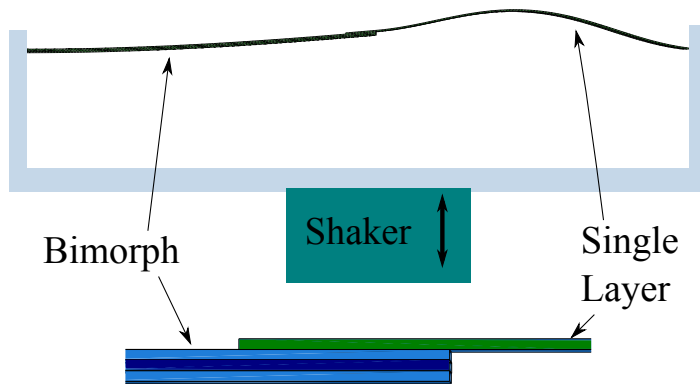


Figure 3.1: A cartoon demonstration of the system used to test buckled piezoelectric beams. Note that in this view, the shaker moves up and down vertically, and the beam is depicted in its top equilibrium position and will proceed to move between this position and the symmetric and downward buckled position.

fixture resonances outside of the range of interest. Also note the lightening holes in the steel base to reduce the mass of the system while minimizing the impact on the flexural rigidity. The first fixture built for proof of concept had a thin aluminum base plate with no reinforcing rod, and suffered from resonances at frequencies in the region of interest. A photo of the fixture mounted on the shaker can be seen in Figure 3.3. Also visible in this photo is the amplifier that drives the shaker, and the charge amplifier used to measure the acceleration at the fixture. The shaker is a LabWorks ET-139 with a dedicated amplifier that runs in constant current mode to reduce heating effects of the armature. Moreover, the system is run with forced air cooling to reduce armature temperature during extended operation. Early tests of this system were run with the shaker mounted to an optical bench, but the range of frequencies that were being explored resulted in some undesired noise levels ambient to the device, and a vibration isolation platform had to

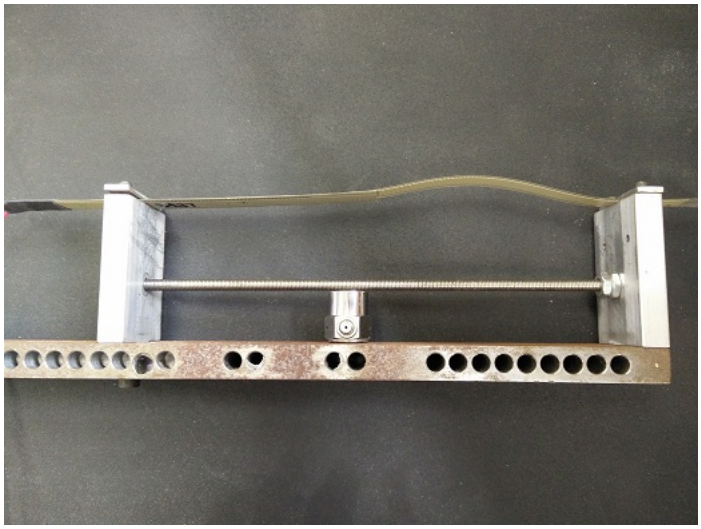

Figure 3.2: Photograph of the fixture used for gathering energy harvesting data from the buckled beam. The main support is the steel beam on the bottom with the holes drilled in it to reduce weight without sacrificing bending stiffness. The piezoelectric accelerometer is mounted to this, and sits just underneath the supporting bar that ensures rigidity of the system and pushes the natural resonances of the fixture out of the region of interest. The end support on the left can be moved to accommodate different lengths of beams, or to control the amount of bucking in the beam.

be developed to decouple the system from the ambient environment. This was accomplished by mounting the shaker on top of an approximately 100 pound steel plate, which rests on sorbothane bumpers designed to give at least 90% isolation in the frequency range of interest. Furthermore, an enclosure was built to contain the entire system and provide a sound barrier. The system is driven by LabVIEW virtual instruments. The program provides a voltage reference for the desired current level to the amplifier, and measures the signal from the accelerometer to determine the actual amount of available power. Typically, experiments are run by proposing a set of steps at different driving frequencies and available power levels. The driving signal for each power level/frequency pair is determined without the piezoelectric beams in place to eliminate any interplay between the power generation and power harvesting systems. To determine the proper forcing amplitude for a desired power level, the system is set to run at a fixed amplitude

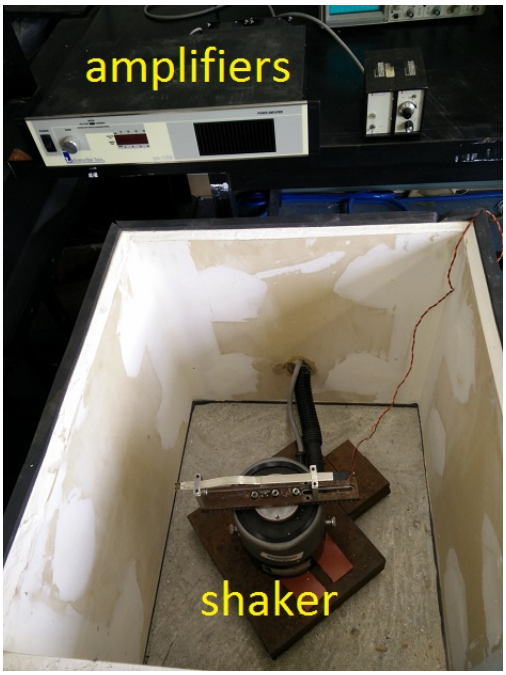


Figure 3.3: The shaker mounted on its vibration isolation platform and surrounded by a sound reducing enclosure. The amplifiers can be seen in the upper portion of the picture, with the shaker amplifier on the left and the piezoelectric charge amplifier on the right.

single frequency sinusoidal wave. This is allowed to run for 15 seconds for any transients to dissipate, then the signal from the accelerometer is recorded for several seconds, then analyzed to determine what the available power level (denoted $P$) was. This is done by running the signal through a lock-in amplifier to determine the true amplitude of the resulting signal (*acceleration*),

$$\int_P A \sin(\omega_i \cdot t) \cdot \sin(\omega_j \cdot t) = 0 \qquad i \neq j, \tag{3.1}$$

$$\int_P A \sin(\omega_i \cdot t) \cdot \sin(\omega_j \cdot t) = 2A \qquad i = j. \tag{3.2}$$

Then applying a correction factor to account for mass, frequency and the piezoelectric calibration,

$$\begin{aligned} x &= A \sin(\omega \cdot t), \\ P &= velocity \cdot force, \\ force &= m \cdot acceleration, \\ velocity &\propto A\,\omega, \\ acceleration &\propto A\,\omega^2, \\ P &\propto m\,A^2\,\omega^3, \\ acceleration^2 &\propto A^2\,\omega^4, \\ P &\propto \frac{acceleration^2}{\omega}. \end{aligned} \tag{3.3}$$

The available power level is then calculated as the square of the acceleration amplitude divided by the forcing frequency in $^{\text{radians}}/_{\text{second}}$. A series of these tests are run to determine the available power level as a function of the input signal amplitude at a specific frequency. With the appropriate look-up tables established, we can proceed to test the

power harvesting capabilities of a piezoelectric beam.

As a measurement of the power harvested by the piezoelectric beams, we have decided to place a 3.3 kilo-Ohm ($k\Omega$) load between the electrodes and measure the resulting voltage. The variety of behaviors exhibited by the beam system can frequently have large amplitude transients, or in some states a large amplitude continuous stable output. Voltage inputs to the DAQ card are limited to $\pm 5$ volts, restricting the maximum amplitude which can be measured accurately. The load resistance of 3.3 $k\Omega$ was experimentally determined to provide sufficient dynamic range to capture important large amplitude effects without losing the small amplitude behavior into the background noise. Additionally the data is oversampled at a rate of 100,000 samples per second (SPS), and reduced to 10,000 SPS by utilizing a moving average, downsampling filter. The software used for both look-up table generation and piezoelectric data gathering are detailed in Appendix B.

## 3.2 Experimental Results

It was found that, depending on the vibrational power and frequency, the voltage across this resistor can be periodic, quasi-periodic, or chaotic in time. Appreciable power is only generated when the beam responds by moving between the two equilibrium positions.

Figure 3.4 shows the rich variety of responses that can occur for periodic forcing of this device. These plots demonstrate the transition from periodic to quasi-periodic to chaotic response. The range of forcing frequencies in this transition is quite small, spanning approximately 6 Hz in going from from a period-5 periodic orbit to a fully chaotic response. Transitions such as the one shown here occur throughout the examined range of frequencies, and can be interpreted in terms of Arnold tongues in the amplitude-

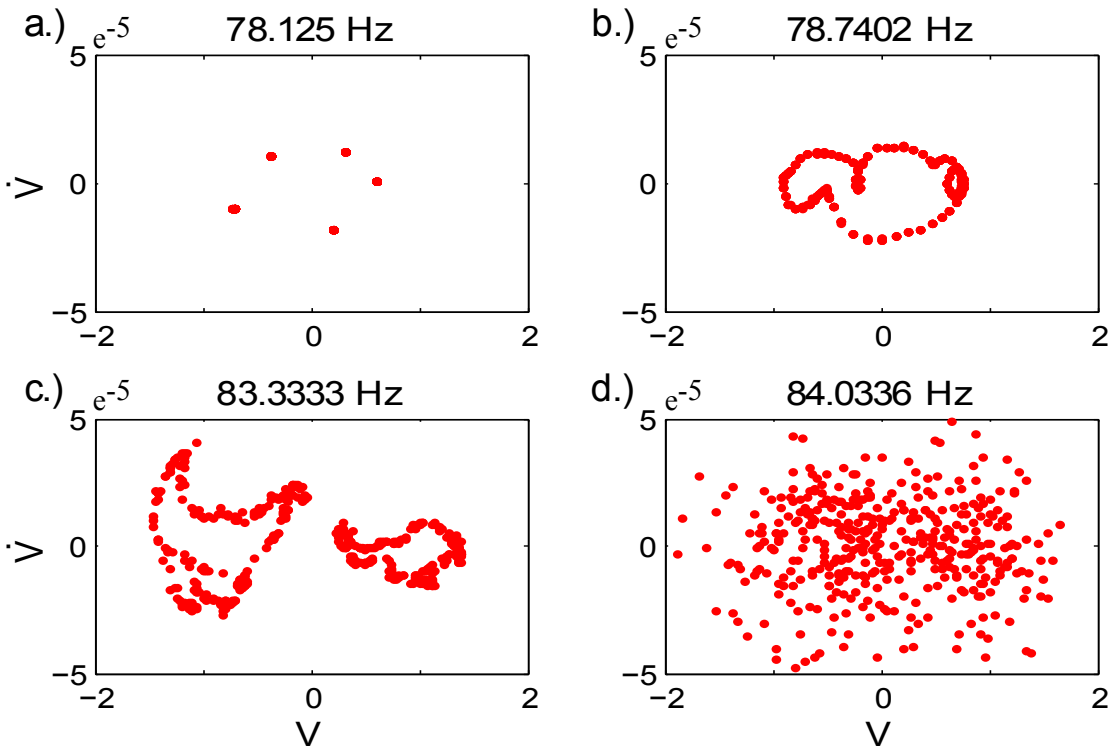


Figure 3.4: Poincaré maps demonstrating a typical transition from a periodic orbit to chaotic oscillations as the forcing frequency is varied. The dots indicate instantaneous values of $V$ and $\dot{V}$ once per forcing cycle. (a) shows a period-5 periodic orbit. (b) shows a quasi-periodic orbit, which wrinkles and folds, as seen in (c), until all recognizable order is lost and a chaotic response is achieved, as seen in (d).

frequency parameter space, with the transition to chaos showing the hallmarks of a torus which wrinkles until it loses its form, giving chaos, as has been observed in [49, 50]. The time series and broad power spectrum of a different chaotic response for forcing at 167 Hz, producing 0.4 mW, is shown in Figure 3.5.

Investigations of this energy harvester were focused on the frequency range of 20-500 Hz, as dictated by the characteristics of the beams and the range of frequencies over which we could acceptably control the shaker. This range was examined as a set of 175 discrete frequencies recorded in Hertz (Hz) with approximately even logarithmic spacing. A simple cantilevered beam has been subjected to the same series of tests for

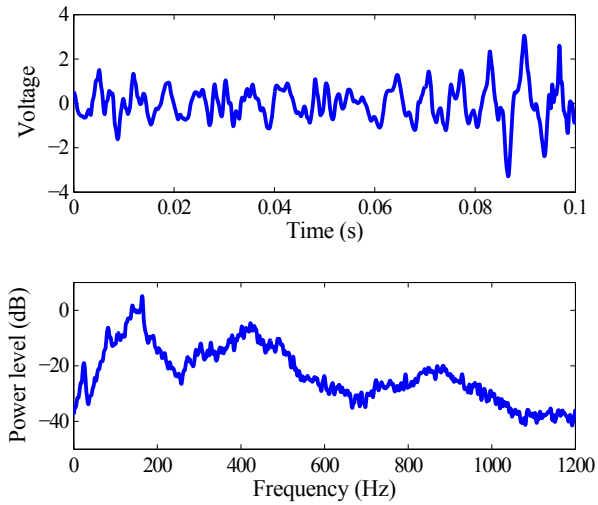


Figure 3.5: Example chaotic time series for shaking frequency 167 Hz, producing 0.4 mW of power. (*lower*) Power spectrum for time series shown above; the broad spectrum is characteristic of chaotic behavior.

comparison; this cantilever was configured as a bimorph element of equal dimension as used in the buckled device, but clamped approximately in the middle and allowed to vibrate on both ends, with resonant frequencies in the neighborhood of 80 Hz. Figure 3.6 demonstrates the increased bandwidth our design produces compared to the linear cantilever. Cantilever data is plotted as dashed lines, while the buckled device is plotted as solid lines. The RMS input power is 13 watts (W) at the highest level, drawn as red with dots, 7.5 W at the intermediate level, drawn as green with $\times$ markers, and 3.2 W at the lowest level, drawn as blue with no markers. Observe that the two halves of the cantilever have slightly different resonances, and the peaks are located at approximately 60 and 100 Hz, providing a maximum output power of 1.0 and 0.3 mW, respectively, for the highest power input. The first snap-through mode of the buckled beam design has been experimentally determined to be approximately 21 Hz. Due to the nonlinearity associated with snap-through dynamics, linear resonance is not observed in the examined range of frequencies and power levels.

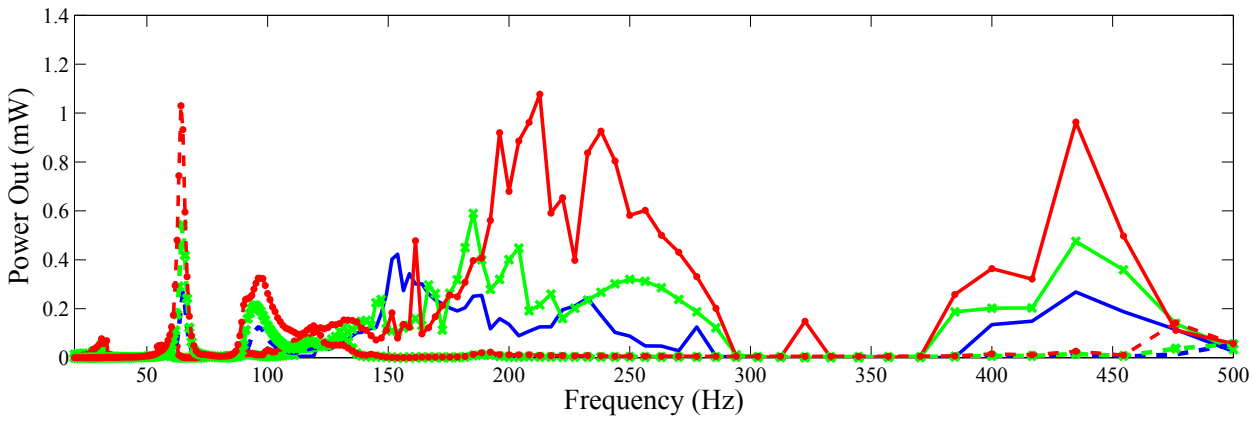


Figure 3.6: Response of the experimental system (*solid*) and reference cantilever (*dashed*) to three different power input levels. RMS input power is 3.2 W for the blue lines with no markers, 7.5 W for the green lines with x markers, and 13 W for the red lines with dots.

Note that the largest peak in the power output of the buckled device is close in magnitude to the resonant peak of the cantilever, and that the location of this peak increases in frequency as the input power is increased. For example, at the lowest input power level, the largest peak occurs at about 153 Hz producing 0.4 mW of power, and maintains power generation over 0.1 mW from 130 to 250 Hz and from 400 to 475 Hz. The cantilever produces peaks of 0.23 and 0.12 mW, and the output is only maintained over 0.1 mW near the resonant peak. At the highest input power level, the maximum peak of the buckled device shifts to 213 Hz with power output of 1.1 mW. Power generation is maintained over 0.2 mW from 165 Hz to 285 Hz and from 380 to 475 Hz. The cantilever produces peaks of 1.0 and 0.3 mW, with no appreciable power generation away from resonance. Note also that the peak of highest power generation for the buckled device is followed closely by a dip, and a second peak, where none of these frequencies are necessarily multiples of the resonant frequency. This shape remains consistent at all tested input power levels.

While observing the system, it can be seen that the oscillations of the beam shift

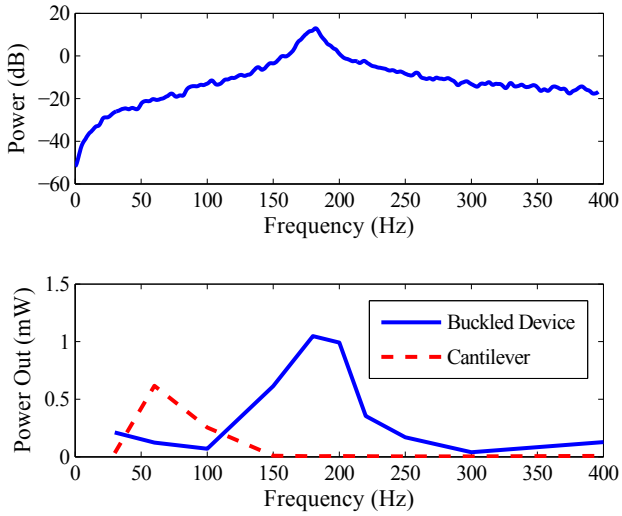


Figure 3.7: (*upper*) Example of broadband frequency input. (*lower*) Power output from broadband input at different frequencies.

between periodic, quasi-periodic, and chaotic response as the forcing frequency is varied. Observations indicate regions that produce a chaotic voltage output result in significant power generation. An interesting viewpoint for understanding the large response over a broad frequency range is the following: suppose we have an oscillator which can undergo chaotic oscillations, which could be transient or attracting. It is known that embedded within a chaotic set are an infinite number of unstable periodic orbits, each of which generically has a different frequency [14]. Indeed, chaos can be viewed as the system 'bouncing around' amongst these unstable periodic orbits; this is an interpretation for why the power spectrum for a chaotic signal is broadband [13]. The response of oscillators in the chaotic regime might be related to resonances between the drive frequency and the various unstable periodic orbits embedded in the chaotic set.

In addition to the single frequency tests, our design and the reference cantilever were subjected to a series of inputs with a wide energy spectrum. A representative input frequency response can be seen in the upper portion of Figure 3.7, with a comparison of

the output of the buckled design and the cantilever arrangement in the lower portion. This input shape was selected to mimic a vibration spectrum that might be available for harvesting, rather than a specific single frequency input as was used in the prior experiments. Tests were conducted through the same frequency range, but with reduced frequency resolution. The buckled device harvested more energy over the range from 150-200 Hz than the cantilever device was able to harvest when excited near its resonant frequency(s). This can be explained by the effects of spreading power over a range of frequencies and the chaotic tendencies of the new design. Many unstable periodic orbits are able to exist in the chaotic regime, allowing the experimental device to respond to many different frequency components, which makes the total effective power being used to excite the system larger than the input power at any specific frequency. The cantilever only responds to input power at its resonant frequency, and thus effectively ignores a large portion of the input power.

## 3.3 Further Experimental Exploration

In order to effectively describe the region of frequency/available power parameter space where chaotic responses are produced by sinusoidal forcing, further investigation was conducted to determine the periodicity of the resulting trajectory. For this examination, the phase space of interest is produced by plotting the voltage of the bimorph ($V_B[i]$) against the voltage of the single layer beam ($V_S[i]$). The concept used is based on breaking the phase space into discrete boxes (each labeled $\beta_{mn}$) as demonstrated in Figure 3.8, and at each time step denoting the box which the trajectory is currently in as "1", and all other boxes as "0".

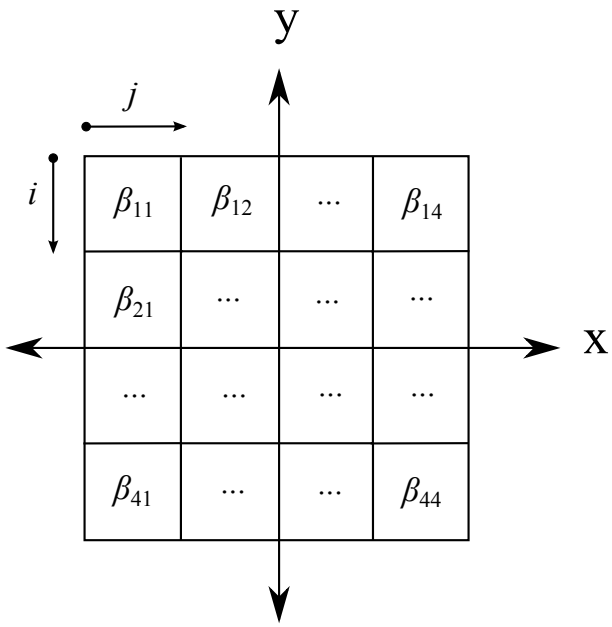


Figure 3.8: Dividing the phase space, here denoted $(x, y)$, into discrete boxes labeled $\beta_{mn}$. Here $m$ and $n$ have both been chosen as 4, with the indices starting in the upper left corner, giving sixteen discrete boxes.

$$T[i] = (V_B[i], V_S[i]) \tag{3.4}$$

$$\beta_{mn}[i] = 1 \qquad T[i] \in \beta_{mn} \tag{3.5}$$

$$\beta_{mn}[i] = 0 \qquad \text{otherwise} \tag{3.6}$$

With this process completed, a time series for each box has been created. Many of the boxes time series may be empty, having never been visited by the trajectory, while some may have only been visited due to noise on an irregular basis. However, examining only the boxes which are consistently visited provides some insight to the periodicity of the trajectory. An FFT, or Fast Fourier Transform is performed on each boxes time series that appears relevant to the problem, and the resulting set of coefficients is compared to the forcing frequency. A locking behavior is indicated if a significant portion of the boxes

show amplitude peaks at integer multiples of the forcing frequency. This information can be used to determine where the resulting trajectory is periodic with the forcing, and where the frequency of the forcing signal appears to have little direct effect on the resulting signal. A demonstration of the frequency locking characteristics of this system in our parameter space of interest can be seen in Figure 3.9, which also provides a comparison between the frequency locking behavior and the power output level. The frequency locking graph shows that for a significant portion of the parameter space, there is consistent locking of the voltage signals to the forcing frequency, as illustrated by green and white areas. Near 30 Hz, there is a region which indicates no apparent locking to the forcing frequency, as indicated by red in Figure 3.9. In this regime, the beam can be observed to move between equilibrium wells occasionally and gently, not exciting any significant power output from the piezoelectric beams, but disturbing the voltage output enough to appear aperiodic. A second region where the voltage signals don't lock to the forcing frequency occurs around 50 Hz. This is the region where the highest output power is achieved. Note that the transition between periodic and aperiodic behavior happens quite suddenly at this boundary. There is a correspondingly sharp boundary present in the power output at the same point. This represents when the beam can be observed to begin rapid and violent snap-through behavior. The region of aperiodic behavior encounters a region of period-2 orbits before it returns to the same periodicity as the forcing function. It is hypothesized that this region could indicate a period doubling bifurcation as the system loses periodicity, and this subject will be explored further in the analytic evaluation of the system. As the frequency is increased past about 70 Hz, another region of primarily periodic behavior is observed. Beam behavior in this region primarily consists of small single well motions, but there may be an occasional snap-through event. However, these events are not frequent enough to make a significant change in the power output, thus we see that the power remains quite low through this region. Around 120

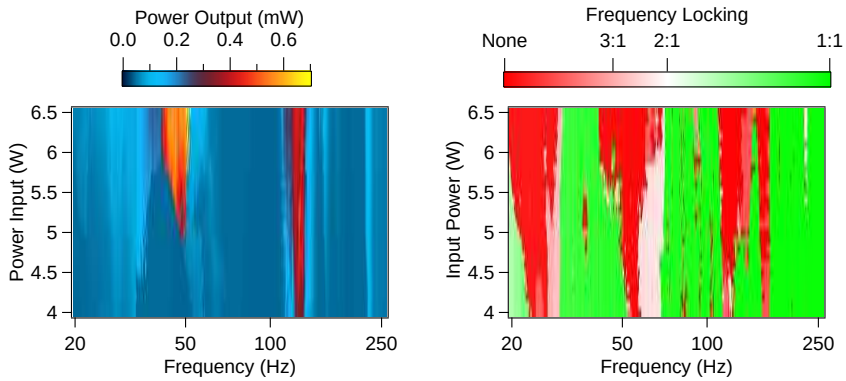


Figure 3.9: (*left*) Power output in parameter space of interest. (*right*) Locking behavior of trajectories whose power output is shown in the left panel. Note that the high power output regions are associated with a lack of frequency locking, though this is not a sufficient condition to predict high output power. Note also that regions of parameter space where frequency locking occurs at a higher integer relation to the forcing signal tend to be associated with the boundary of a region where no frequency locking is detected.

Hz we observe another band of aperiodic behavior, and an associated high power output region. In this range, the beam can be observed to exhibit rapid oscillations between wells, and the high power output can be easily surmised from the observed behavior. Once periodic behavior is observed again, it continues for the rest of the range of interest without any noteworthy behavior.

# Chapter 4

# Modeling

## 4.1 Analytic Attempts

Following the approach of Nayfeh et. al [41], we can attempt to create an analytic model of the beam system using separation of variables and Sturm-Liouville methods to solve the PDE. We will start by dividing the system into two beams with different physical parameters which each have a fixed boundary condition at one end and are forced to match the other beam at the joint end. To faithfully represent the glued joint we demand that both the displacement and the rotation at the joint remain continuous. This union of beams requires that we deal with an eighth order system of equations instead of a fourth order system, but it allows a representation of the discontinuous physical parameters through the length of the beam. This complication of the problem is critical for accurate representation of the original system. We will proceed by finding the static or equilibrium solution by solving for the homogeneous solution to the PDE, and then finding the particular solution to determine the response to a forcing function.

### 4.1.1 Governing PDE

We start with the partial differential equation governing the motion of a beam under compressive stress, with the possibility of buckling occuring as was derived in section 2.2 as equation (2.48):

$$M\frac{\partial^2 w}{\partial t^2} + EI\frac{\partial^4 w}{\partial x^4} + P\frac{\partial^2 w}{\partial x^2} + c\frac{\partial w}{\partial t} - \frac{EA_r}{2L}\frac{\partial^2 w}{\partial x^2}\int_0^L \left(\frac{\partial w}{\partial x}\right)^2 \mathrm{d}x = F(x)\cos\Omega t, \tag{4.1}$$

where $P$ is the axial load on the beam, $w(x,t)$ is the shape of the beam, $E$ is the Young's modulus, $I$ is the second moment of area about the $x$ axis, $M$ is the mass of the beam, $c$ is the damping coefficient, $A_r$ is the cross-sectional area of the beam, and $L$ is the length of the beam.

### 4.1.2 Buckled Equilibrium

In determining the static buckled equilibrium state, we set the time derivatives to zero, drop the forcing term, and change variables such that $\psi(x)$ now represents the buckled equilibrium shape:

$$EI\frac{\partial^4 \psi}{\partial x^4} + P\frac{\partial^2 \psi}{\partial x^2} - \frac{EA_r}{2L}\frac{\partial^2 \psi}{\partial x^2}\int_L \left(\frac{\partial \psi}{\partial x}\right)^2 \mathrm{d}x = 0. \tag{4.2}$$

One way to look at our beam is to consider it to be a system of two beams which are subject to coupled boundary conditions at the joint. Under this approach, the shape of the beam will be split into left and right portions as follows:

$$\psi(x) = \begin{cases} \psi_L(x) & -L_L \leq x \leq 0 \\ \psi_R(x) & 0 \leq x \leq L_R, \end{cases} \tag{4.3}$$

where $L_L$ is the length of the bimorph beam, and $L_R$ is the length of the single layer beam. With the beam descibed this way, we need to add a forcing term to our governing equation (4.2) for each side of the beam to account for forces present at the junction in the middle. Thus each side of the beam can be described by the equation

$$E_i I_i \frac{\partial^4 \psi_i}{\partial x^4} + P \frac{\partial^2 \psi_i}{\partial x^2} - \frac{E_i A_{ri}}{2L_i} \frac{\partial^2 \psi_i}{\partial x^2} \int_{L_i} \left( \frac{\partial \psi_i}{\partial x} \right)^2 \mathrm{d}x = W(x), \qquad i = L, R. \tag{4.4}$$

This can be re-arranged to give:

$$\frac{\partial^4 \psi_i}{\partial x^4} + \lambda^2 \frac{\partial^2 \psi_i}{\partial x^2} = W(x), \tag{4.5}$$

where $\lambda_i = \sqrt{\frac{P}{E_i I_i} - \frac{A_{ri}}{2L_i I_i} \int_{L_i} \left( \frac{\partial \psi_i}{\partial x} \right)^2 \mathrm{d}x}$ and is constant for a given buckled shape. From beam theory, we know that $W(x)$ describes a distributed load on the beam. For each side of our beam, the only loading comes from the joint as an applied shear and moment. Therefore the distributed load would be represented as a delta function. However, we can calculate the resulting moment distribution throughout the beam. The second integral of the distributed load is the moment distribution, so we can integrate (4.5) twice and plug in our known moment distribution:

$$M_i(x) = M_j(0) + \nu_j(0)(L_i - x), \qquad i \neq j \tag{4.6}$$

$$\frac{\partial^2 \psi_i}{\partial x^2} + \lambda_i^2 \psi_i = M_i(x) + \kappa_1 x + \kappa_2, \tag{4.7}$$

where $M_j(0)$ and $\nu_j(0)$ are the moment and shear at $x = 0$, respectively. This admits a general solution of the form:

$$\psi_i(x) = c_{i1} + c_{i2}x - c_{i3}\cos(\lambda_i x) - c_{i4}\sin(\lambda_i x). \tag{4.8}$$

The boundary conditions are defined as clamped at both ends and continuity of position, slope, shear and moment at the point where the beams meet, which is at $x = 0$. This allows us to construct an 8x8 matrix to determine the coefficients of the buckled shape:

$$\begin{bmatrix} 1 & 0 & -1 & 0 & -1 & 0 & 1 & 0 \\ 0 & 1 & 0 & -\lambda_L & 0 & -1 & 0 & \lambda_R \\ 0 & 0 & -E_L I_L \lambda_L^2 & 0 & 0 & 0 & E_R I_R \lambda_R^2 & 0 \\ 0 & 0 & 0 & -E_L I_L \lambda_L^3 & 0 & 0 & 0 & -E_R I_R \lambda_R^3 \\ 1 & -L_L & -\cos(-\lambda_L \cdot L_L) & -\sin(-\lambda_L \cdot L_L) & 0 & 0 & 0 & 0 \\ 0 & 1 & \lambda_L \sin(-\lambda_L \cdot L_L) & -\lambda_L \cos(-\lambda_L \cdot L_L) & 0 & 0 & 0 & 0 \\ 0 & 0 & 0 & 0 & 1 & L_R & -\cos(\lambda_R \cdot L_R) & -\sin(\lambda_R \cdot L_R) \\ 0 & 0 & 0 & 0 & 0 & 1 & \lambda_R \sin(\lambda_R \cdot L_R) & \lambda_R \cos(\lambda_R \cdot L_R) \end{bmatrix} \begin{bmatrix} c_{L1} \\ c_{L2} \\ c_{L3} \\ c_{L4} \\ c_{R1} \\ c_{R2} \\ c_{R3} \\ c_{R4} \end{bmatrix} = \begin{bmatrix} 0 \\ 0 \\ 0 \\ 0 \\ 0 \\ 0 \\ 0 \\ 0 \end{bmatrix}.$$

The determinant of the matrix is set to zero, and solved for $\lambda_L$ and $\lambda_R$. These values are plugged into the matrix equation to determine the values of the coefficients. With parameters to mimic our experimental setup, this results in $\lambda_L$=21.2 and $\lambda_R$=53.1.

### 4.1.3 Vibrations about Buckled Equilibrium

If we define the shape found above as $f(x)$, we are able to write the expected linear vibration shapes about the buckled equilibrium as

$$w(x,t) = Af(x) + v(x,t), \tag{4.9}$$

where $v(x,t)$ is the vibration about the buckled shape, and $A$ represents the amount of buckling. This assumed shape can then be plugged back into (4.1) and analyzed. To determine the linear vibration modes, we will drop the damping and forcing terms, giving

the following equation:

$$M\frac{\partial^2 w}{\partial t^2}+EI\frac{\partial^4 w}{\partial x^4}+P\frac{\partial^2 w}{\partial x^2}-\frac{EA_r}{2L}\frac{\partial^2 w}{\partial x^2}\int_x\left(\frac{\partial w}{\partial x}\right)^2\mathrm{d}x=0. \tag{4.10}$$

We will now substitute our expected $w(x,t)$ into (4.10) but we will switch notation such that an overdot represents a time derivative and a prime indicates a spatial derivative:

$$M\ddot{v}+EI\left(Af''''+v''''\right)+P\left(Af''+v''\right)-\frac{EA_r}{2L}\left(Af''+v''\right)\int_x(Af'+v')^2\mathrm{d}x=0. \tag{4.11}$$

Expanding the square inside the integral and gathering all the $v$ terms on one side, we arrive at the following,

$$\frac{M}{EI}\ddot{v}+v''''+\left(\frac{P}{EI}-\frac{A_rA^2}{2LI}\int_x f'^2\,\mathrm{d}x\right)v''-\frac{A_rA^2}{LI}f''\int_x f'v'\mathrm{d}x-\frac{A_rA}{LI}f''\int_x v'^2\mathrm{d}x \tag{4.12}$$

$$-\frac{A_r}{2LI}v''\int_x\left(2Af'v'+v'^2\right)\mathrm{d}x=-\left(Af''''+\frac{P}{EI}Af''-\frac{A_rA}{2LI}f''\int_x\left(Af'\right)^2\mathrm{d}x\right). \tag{4.13}$$

The RHS of (4.13) can be seen to satisfy (4.2) and is therefore equal to zero. Since we are looking for small vibrations about the equilibrium position, we can neglect terms higher than first order in $v$, leaving us with

$$\frac{M}{EI}\ddot{v}+v''''+\left(\frac{P}{EI}-\frac{A_rA^2}{2LI}\int_x f'^2\,\mathrm{d}x\right)v''-\frac{A_rA^2}{LI}f''\int_x f'v'\mathrm{d}x=0. \tag{4.14}$$

We can now perform a separation of time and space by assuming that the solutions take the form

$$v(x,t)=\chi(x)\Gamma(t). \tag{4.15}$$

Dropping the arguments and plugging into (4.14):

$$\frac{M}{EI}\chi\ddot{\Gamma}+\chi''''\Gamma+\left(\frac{P}{EI}-\frac{A_rA^2}{2LI}\int_x f'^2\,\mathrm{d}x\right)\chi''\Gamma-\frac{A_rA^2}{LI}f''\int_x f'\chi'\Gamma\mathrm{d}x=0. \tag{4.16}$$

Putting the spatial terms on the RHS and the temporal terms on the LHS:

$$-\frac{1}{\Gamma}\left(\frac{M}{EI}\ddot{\Gamma}\right)=\frac{1}{\chi}\left(\chi''''+\left(\frac{P}{EI}-\frac{A_rA^2}{2LI}\int_x f'^2\,\mathrm{d}x\right)\chi''-\frac{A_rA^2}{LI}f''\int_x f'\chi'\mathrm{d}x\right). \tag{4.17}$$

From this it becomes clear that the only way these can be equivalent for all time and space is for them to be equal to a constant (henceforth referred to as '$\kappa$'), allowing us to rewrite as

$$\frac{M}{EI}\ddot{\Gamma}=-\kappa\Gamma, \tag{4.18}$$

$$\chi''''+\left(\frac{P}{EI}-\frac{A_rA^2}{2LI}\int_x f'^2\,\mathrm{d}x\right)\chi''-\kappa\chi=\frac{A_rA^2}{LI}f''\int_x f'\chi'\mathrm{d}x. \tag{4.19}$$

Solving for $\Gamma$ we find that $\kappa=\frac{M\omega^2}{EI}$ and $\Gamma(t)=\mathrm{e}^{i\omega t}$ where $\omega$ is representative of a frequency in $^{\mathrm{rad}}/_{\mathrm{sec}}$. The integral on the RHS of (4.19) will be constant for a given $\chi$, and the above can be rewritten as

$$\chi''''(x)+b\chi''(x)-\kappa\chi(x)=h(x), \tag{4.20}$$

where $b=\frac{P}{EI}-\frac{A_rA^2}{2LI}\int_x f'^2\,\mathrm{d}x$, $\kappa=\frac{M\omega^2}{EI}$ and $h(x)=\frac{A_rA^2}{LI}\left[\int_x f'\chi'\mathrm{d}x\right]f''(x)$. This can be viewed as a fourth order ODE with a forcing term. We would like to find a solution to (4.20) where $\chi(x)$ can be described as a series of eigenfunctions of a Sturm-Liouville problem. The general form of a fourth order Sturm-Liouville problem is

$$\frac{d^2}{dx^2}\left[q(x)\frac{d^2u}{dx^2}\right]+\frac{d}{dx}\left[p(x)\frac{du}{dx}\right]+z(x)u=\lambda g(x)u. \tag{4.21}$$

Thus we want to find solutions of the form (where $\varphi$ is now an eigenfunction),

$$u(x)=\sum_{n=1}^{\infty} \upsilon_n \varphi_n(x) \tag{4.22}$$

satisfying:

$$[q(x)u''(x)]''+[p(x)u'(x)]'+[z(x)-\lambda(g(x))]\,u(x)=0 \tag{4.23}$$

for the homogeneous portion of the solution, and changing the 0 on the RHS to $h(x)$ for the particular solution. We can make examination of this problem significantly easier by assigning values to the coefficient functions of (4.21). In this problem we find that $q(x)=1$, $p(x)=b$, $\lambda g(x)=\kappa$, and $z(x)=0$. Let's look at the homogeneous portion first:

$$\sum_{n=0}^{\infty} [\upsilon_n \varphi_n''''+b\upsilon_n \varphi_n''-\kappa_n \upsilon_n \varphi_n]=0. \tag{4.24}$$

This differential equation allows solutions of the form

$$\varphi_n(x)=\alpha_{n1}\cos(\eta_n x)+\alpha_{n2}\sin(\eta_n x)+\alpha_{n3}\cosh(m_n x)+\alpha_{n4}\sinh(m_n x), \tag{4.25}$$

$$\eta_n, m_n=\sqrt{\pm\frac{b}{2}+\frac{1}{2}\sqrt{b^2+4\kappa_n}}. \tag{4.26}$$

Now lets turn to the particular solution:

$$\sum_{n=1}^{\infty} [\upsilon_n \varphi_n''''+b\upsilon_n \varphi_n''-\kappa \varphi_n]=h(x). \tag{4.27}$$

Adding and subtracting from RHS:

$$\sum_{n=1}^{\infty} [\upsilon_n \varphi_n''''+b\upsilon_n \varphi_n''-\kappa \varphi_n]=h(x)+\sum_{n=1}^{\infty} \kappa_n \upsilon_n \varphi_n-\sum_{n=1}^{\infty} \kappa_n \upsilon_n \varphi_n, \tag{4.28}$$

rearranging,

$$\sum_{n=1}^{\infty}[\upsilon_n\varphi_n''''+b\upsilon_n\varphi_n''-\kappa_n\varphi_n]=h(x)+\sum_{n=1}^{\infty}(\kappa-\kappa_n)\,\upsilon_n\varphi_n. \tag{4.29}$$

Recognize the LHS is zero by the definition of the homogeneous solution, and we arrive at

$$\sum_{n=1}^{\infty}(\kappa_n-\kappa)\,\upsilon_n\varphi_n=h(x). \tag{4.30}$$

Multiply by $\varphi_k$ and integrating over the region of interest,

$$\sum_{n=1}^{\infty}(\kappa_n-\kappa)\,\upsilon_n\int_L\varphi_n\varphi_k\,\mathrm{d}x=\int_L h(x)\varphi_k\,\mathrm{d}x. \tag{4.31}$$

By the orthogonal propeties of $\varphi$ we know that $\int_L\varphi_k\varphi_n\,\mathrm{d}x=\delta_{nk}$, and the above can be rewritten

$$(\kappa_k-\kappa)\,\upsilon_k=\int_L h(x)\varphi_k\,\mathrm{d}x \tag{4.32}$$

or

$$\upsilon_k=\frac{\int_L h(x)\varphi_k\,\mathrm{d}x}{\kappa_k-\kappa}. \tag{4.33}$$

Therefore the particular solution to (4.20) can be written

$$\chi_p(x)=\sum_{k=1}^{\infty}\frac{\int_L h(x)\varphi_k(x)\,\mathrm{d}x}{\kappa_k-\kappa}\varphi_k(x), \tag{4.34}$$

implying the full solution can be written as

$$\chi(x)=\sum_{k=1}^{\infty}\upsilon_k\varphi_k(x)+\sum_{k=1}^{\infty}\frac{\int_L h(x)\varphi_k(x)\,\mathrm{d}x}{\kappa_k-\kappa}\varphi_k(x), \tag{4.35}$$

or alternatively,

$$\chi(x)=\sum_{k=1}^{\infty}\left(\upsilon_k+\frac{1}{\kappa_k-\kappa}\int_L h(x)\varphi_k(x)\,\mathrm{d}x\right)\varphi_k(x), \tag{4.36}$$

allowing us to write the complete solution in terms of the homogeneous part. This method has proven to be extremely difficult to solve for all necessary eigenvalues, owing in part to the difficulty of finding roots to an eighth order transcendental equation. Moreover, it has been found that this method is not capable of sustaining snap-through behavior at above infinitesimal buckling levels, and therefore is insufficient for recreating the observed behavior of our beam system. This behavior is consistent with the assumption made in the derivation of the beam's PDE in (2.30). Unfortunately, dropping in this assumption results in an extremely complex potential energy function which produces an analytically intractable PDE and does not assist in our attempt to produce a model of the experimentally observed behavior.

## 4.2 Finite Element Representation

As an alternative approach,the FEA software ABAQUS [51] has been used to construct a model of the beam. The model is constructed from two basic units: a steel shim and a piezoelectric beam. The dimensions and important material parameters (experimentally determined) of each section can be seen in Table 4.1, while a detailed explanation of the process of constructing the ABAQUS model is contained in Appendix A. These units are assembled into a structure equivalent to the experimental setup. Both free ends of the assembly are constrained as fixed boundary conditions, allowing no translation or rotation to occur at the clamping points. To model the buckled equilibrium, the axial degree of freedom is allowed to translate and an axial force is applied. A quasi-

| | Steel shim | Piezoelectric |
|---|---|---|
| width (mm) | 14 | 10 |
| height (mm) | 0.4 | 0.4 |
| length (mm) | 116 | 116 |
| mass/length (g/mm) | 0.045 | 0.015 |
| modulus (GPa) | 180 | 15.2 |
| Poisson ratio | 0.3 | 0.3 |

Table 4.1: Material parameters for the two different sections used to build the finite element model.

static analysis then determines the resulting buckled configuration, as seen in Figure 4.1. Thereafter the axial degree of freedom is fixed, and a linear frequency analysis is performed to extract mode shapes (denoted $[U]_{(i)}$) and the associated natural frequencies about the buckled equilibrium configuration. The mode shapes and their associated frequencies are not constant as the degree of buckling changes, similar to the analytic solutions in [41] for a simple buckled beam. The dependence of the associated frequencies on the compressive load can be seen in Figure 4.2. The linear mode shapes are computed so that they are orthogonal with respect to the finite element mass matrix $[M]$:

$$[0] = [U]^T_{(i+1)} [M] [U]_{(i)} . \tag{4.37}$$

However, these modes are not orthogonal to the buckled equilibrium shape. Examining the components of the displacement, we find that the out of plane motions are several orders of magnitude lower than those in the transverse and axial directions and will be assumed to be negligible in the frequency range of interest. The axial motion ($u$) is critical to determining the buckled configuration, but subsequently any axial motion due to oscillations about the buckled equilibrium are very small compared to the transverse motions. Therefore we will consider the axial motion fixed after the initial buckling, and assume that only transverse motions ($w$) of the beam are significant to time varying

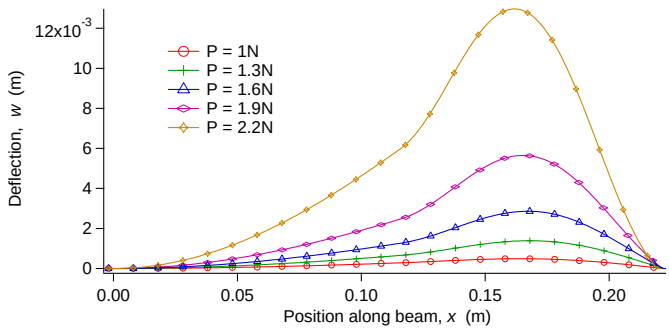


Figure 4.1: Evolution of buckled equilibrium position with axial loads between 1 and 2.2 N. Note that the right hand side of the beam, which consists of the single layer portion, exhibits much larger deviations from the centerline than the bimorph section. In this paper, the curve at P=1.3 N will be used for analysis.

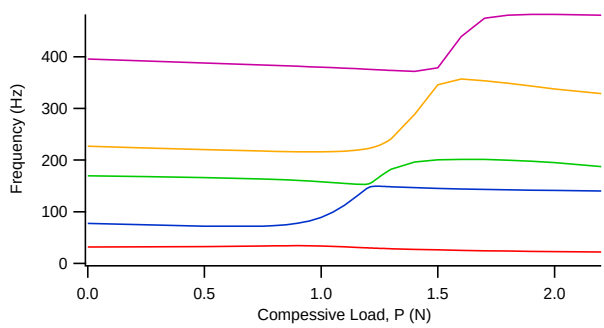


Figure 4.2: Dependence of natural frequencies on the axial compressive load. Note that eigenvalues two and three come very close together when the axial load is approximately 1.25 N. Analytic predictions for buckled beams indicate that there should be an eigenvalue crossing between the second and third eigenvalues. Examined closely it is clear that these eigenvalues do not cross in this example, but independently evolve through this region. The difference between observed model behavior and expected analytic behavior is due to the symmetry breaking of the glued joint. The region where these eigenvalues approach each other has been found to be a promising energy harvesting region.

energy storage. Assuming that the time and spatial dependence of $w$ can be separated and any arbitrary beam shape can be reconstructed by linear combinations of the mode shapes, we write the displacement functions as

$$u(x) = u_c(x), \tag{4.38}$$

$$w(x,t) = \sum_{i=0}^{\infty} a_i(t) w_i(x), \tag{4.39}$$

or equivalently in vector notation,

$$w(x,t) = \underline{a}(t) \cdot \underline{w}(x). \tag{4.40}$$

Here $u_c$ is the function representing the axial displacement associated with beam buckling, $\underline{a}(t)$ is a vector which contains the mode amplitudes, and $\underline{w}(x)$ is a vector of shape functions, which are the transverse displacements of the mode shapes. The buckled equilibrium transverse displacements are assumed to represent a fundamental mode of the dynamic response of the system, with its contribution to the total displacements varying according to $a_0(t)$, and the subscript 0 has been assigned to it. Increasing indices in the summation (4.39) indicate increasing natural frequency for the associated mode shape. The shape of the first three mode shapes with the respective buckled equilibrium shape and axial load are shown in Figure 4.3.

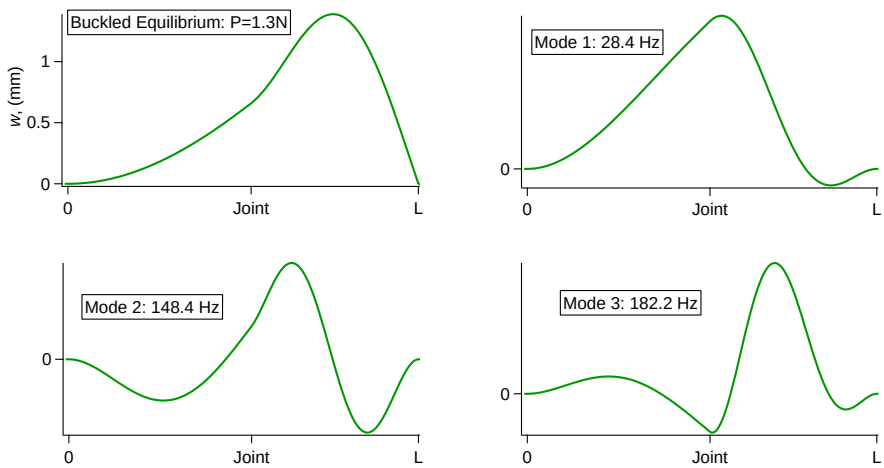


Figure 4.3: Buckled equilibrium state in terms of transverse displacement and the first three normal modes with their associated frequencies about the buckled equilibrium with axial load of 1.3 N. The horizontal axis represents the distance along the beam from 0 to $L$, while the the vertical axis portrays the transverse deflection, actual for the buckled equilibrium mode and normalized for the linear modes.

## 4.3 Energy Projection

### 4.3.1 Kinetic Energy

The kinetic energy can be expressed by superimposing the transverse beam motions onto the base excitation, $y(t)$:

$$T := \int_0^L \frac{1}{2} m(x) \left( \frac{\partial w}{\partial t} + \frac{\partial y}{\partial t} \right)^2 \mathrm{d}x \approx \frac{m_b}{2} \int_0^{L_b} (\dot{w} + \dot{y})^2 \, \mathrm{d}x + \frac{m_s}{2} \int_{L_s}^{L} (\dot{w} + \dot{y})^2 \, \mathrm{d}x, \quad (4.41)$$

where $m_b$ and $m_s$ are the mass per unit length of the bimorph and single layer, respectively. The time derivative of the displacement can be written as

$$\dot{w} = \dot{a}_0 \, w_0 + \sum_{i=1}^{\infty} \dot{a}_i \, w_i. \quad (4.42)$$

The buckled equilibrium displacement has been separated from the linear modes to preserve the orthogonality properties. We obtain

$$\dot{w}^2 = \dot{a_0}^2 w_0^2 + 2\sum_{i=1}^{\infty}\left(\dot{a}_i\dot{a}_0 w_i w_0\right) + \sum_{i=1}^{\infty}\sum_{j=1}^{\infty}\left(\dot{a}_i\dot{a}_j w_i w_j\right). \tag{4.43}$$

From the orthogonality condition (4.37), the last term integrates to zero when $i \neq j$. This allows the kinetic energy to be calculated as

$$\begin{aligned} T \approx & \frac{m_b}{2}\int_0^{L_b}\left[\dot{a_0}^2 w_0^2 + \sum_{i=1}^{n}\left(2\dot{a}_i\dot{a}_0 w_i w_0 + \dot{a_i}^2 w_i^2\right) + \sum_{i=0}^{n}\left(2\dot{a}_i w_i \dot{y} + \dot{y}^2\right)\right]\mathrm{d}x \\ & + \frac{m_s}{2}\int_{L_s}^{L}\left[\dot{a_0}^2 w_0^2 + \sum_{i=1}^{n}\left(2\dot{a}_i\dot{a}_0 w_i w_0 + \dot{a_i}^2 w_i^2\right) + \sum_{i=0}^{n}\left(2\dot{a}_i w_i \dot{y} + \dot{y}^2\right)\right]\mathrm{d}x, \end{aligned} \tag{4.44}$$

where $n$ is the number of mode shapes that we have included in a truncated calculation.

### 4.3.2 Potential Energy

The potential energy has contributions from both mechanical and electrical domains. In the mechanical domain, the strain energy is calculated as one half the volume integral of the product of stress and strain. In the electrical domain, the energy is calculated as the negative of one half the volume integral of the product of electric displacement and electric field:

$$U = \frac{1}{2}\int_V \sigma\,\varepsilon\,\mathrm{d}V - \frac{1}{2}\int_V DE\,\mathrm{d}V, \tag{4.45}$$

where $\sigma$ is the stress, $\varepsilon$ is the strain, $D$ is the electric displacement, and $E$ is the electric field. Piezoelectric constitutive equations as derived in section 2.2 [38] describe elastic and dielectric behavior and provide the connection between the mechanical and electrical

portions:

$$\sigma_{ij} = c^E_{ijkl}\,\varepsilon_{kl} - e_{kij}\,E_k, \tag{4.46}$$

$$D_i = e_{ikl}\,\varepsilon_{kl} + \epsilon^{\varepsilon}_{ik}\,E_k, \tag{4.47}$$

where $c^E_{ijkl}$ is the tensor of elastic constants evaluated at fixed electric field, $e_{kij}$ is the tensor of piezoelectric coupling constants when electric field and strain are taken as the independent variables, and $\epsilon^{\varepsilon}_{ik}$ is the tensor of electric permittivity constants evaluated at fixed strain. Euler-Bernoulli beam theory assumes that all stress components are negligible except those in the axial direction. Piezoelectric theory defines the poling direction as the 3-direction [44], which coincides in our case with the axial direction in a $d_{31}$ beam configuration. The constitutive equations can therefore be reduced to

$$\begin{bmatrix} \sigma_3 \\ D_1 \end{bmatrix} = \begin{bmatrix} c^E_{33} & -e_{31} \\ e_{31} & \epsilon^{\varepsilon}_{11} \end{bmatrix} \begin{bmatrix} \varepsilon_3 \\ E_1 \end{bmatrix}. \tag{4.48}$$

Piezoelectric constants are provided in a slightly different form, as seen in Table 4.2. The necessary coefficients are calculated as [38]

$$c^E_{33} = Y, \tag{4.49}$$

$$e_{31} = d_{31} \cdot Y, \tag{4.50}$$

$$\epsilon^{\varepsilon}_{11} = \epsilon^{\sigma}_{11} - d^2_{33} \cdot Y, \tag{4.51}$$

where $Y$ is the experimentally determined elastic modulus of the section being analyzed as presented in Table 4.1 and $\epsilon^{\sigma}_{11}$ is the dielectric permittivity in the poled direction at

| Constant | Value | Units |
|---|---|---|
| $d_{31}$ | 375 | $pm/V$ |
| $\epsilon^{\sigma}_{11}/\epsilon_0$ | 1725 | $n/a$ |

Table 4.2: Piezoelectric constants provided by Advanced Cerametrics Inc. [48].

fixed stress. Combining (4.45) and (4.48), and dropping the subscripts we find that

$$U = \frac{1}{2}\int_V Y\,\varepsilon^2\,\mathrm{d}V - \int_V e\,\varepsilon\,E\,\mathrm{d}V - \frac{1}{2}\int_V \epsilon\,E^2\,\mathrm{d}V. \tag{4.52}$$

First we will deal with the strain energy, then later we will come back to the electrical contributions to the potential energy.

### Equilibrium Strain Energy

At equilibrium, the electric field and electric displacement are zero, and only the buckled mode shape contributes to the potential energy. Thus this potential energy can be expressed as

$$U_{eq} = \frac{1}{2}\int_V Y\,\varepsilon^2\,\mathrm{d}V. \tag{4.53}$$

Here the goal is to develop an expression for the strain energy that has the buckled equilibrium mode amplitude as the independent variable. In order for a double well potential to exist, the energy function must be quartic at minimum. Forcing the symmetric, stable equilibrium positions to occur at $a_0 = \pm 1$, the potential energy can be approximated as

$$U_{eq} = \frac{1}{2}\int_V Y\varepsilon^2\,\mathrm{d}V \approx \eta_0 - 2\beta\,a_0^2 + \beta\,a_0^4 + \mathcal{O}(a_0^6), \tag{4.54}$$

where $\frac{\partial U_{eq}}{\partial a_0}$ must be equal to zero when evaluated at $a_0 = \pm 1$. From the finite element analysis, there is a reference for the strain energy at two configurations: the buckled equilibrium position ($a_0 = \pm 1$), and the constrained flat equilibrium ($a_0 = 0$). Using

these reference values allows one to solve for $\beta$.

### Dynamic Contributions to Strain Energy

We note that for strains to be infinitesimal we must have

$$\left| 2\frac{\partial u}{\partial x} + \left(\frac{\partial u}{\partial x}\right)^2 + \left(\frac{\partial w}{\partial x}\right)^2 \right| \ll 1. \tag{4.55}$$

This can occur when

$$\left(\frac{\partial w}{\partial x}\right)^2 = \mathcal{O}\left(\frac{\partial u}{\partial x}\right) \ll 1. \tag{4.56}$$

These conditions preclude even moderately large transverse deflections when compared to the length of the beam. The other possibility for fulfilling the infinitesimal strain condition is that

$$\frac{\partial u}{\partial x} < 0 \tag{4.57}$$

and the combination

$$2\frac{\partial u}{\partial x} + \left(\frac{\partial u}{\partial x}\right)^2 + \left(\frac{\partial w}{\partial x}\right)^2 \tag{4.58}$$

is small because of cancellation of positive and negative terms. This can happen in buckled beams, but if this condition prevails and the beam oscillates from a positive deflection to a negative deflection by passing through its straight configuration, the axial strain could be large due to the absence of the positive transverse deflection term. However, if we assume that the oscillation from positive deflection to negative deflection occurs by a combination of modes of deformation, the beam may never be straight in such motion, and large deflections may then be permitted. This relieves us of the requirement (4.56), and instead we may rely on (4.55). Thus under assumptions of small strain and moderate rotation, we approximate the axial strain at any point from the

Green-Lagrange strain tensor [52] as

$$\varepsilon \approx \frac{\partial u_c}{\partial x} - z\frac{\partial^2 w}{\partial x^2} + \frac{1}{2}\left(\frac{\partial u_c}{\partial x} - z\frac{\partial^2 w}{\partial x^2}\right)^2 + \frac{1}{2}\left(\frac{\partial w}{\partial x}\right)^2, \tag{4.59}$$

where $z$ is the distance of the specified point from the neutral axis of the beam. Finite element analysis does not provide enough reference points to generate a full description of the strain energy using the amplitudes of the mode shapes. To overcome this obstacle, it is necessary to use analytic predictions to determine the shape of the energy surfaces. To generate these approximate surfaces, the buckled equilibrium amplitude will be fixed at unity, and two mode amplitudes varied while all other amplitudes are equal to zero. The resulting shape is then integrated over the approximate beam dimensions as

$$\Omega \approx \frac{1}{2}\int_V Y\varepsilon^2 \,\mathrm{d}V, \tag{4.60}$$

where $\varepsilon$ is as in (4.59). This produces an analytic prediction of the strain energy ($\Omega$) at one particular combination of mode shapes. We repeat this procedure on a grid to span the maximum mode amplitudes observed in simulation, which is an iterative process. Now a surface has been produced describing the energy variation with two mode shapes about the buckled equilibrium. This surface is fit with a fourth order polynomial in two variables, remembering that symmetric solutions dictate which terms are needed. As an example, the polynomial descibing the variation of strain energy with variation of modes $i$ and $j$ is of the form:

$$\begin{aligned}\Omega(a_i, a_j, a_0) \approx\ & \eta_1 + m_1\, a_i^2 + m_2\, a_j^2 + m_3\, a_i\, a_j + m_4\, a_0\, a_i^2\, a_j + m_5\, a_0\, a_i\, a_j^2 \\ & + m_6\, a_0\, a_i^3 + m_7\, a_0\, a_j^3 + m_8\, a_i^2\, a_j^2 + m_9\, a_i^3\, a_j + m_{10}\, a_i\, a_j^3 + m_{11}\, a_i^4 + m_{12}\, a_j^4,\end{aligned} \tag{4.61}$$

where the $m$'s are the coefficients to be solved for in the fit. Repeating this procedure for all combinations of mode shapes, all of the planes can be combined to produce a polynomial fit of the strain energy surface as a function of the mode amplitudes. The approximate nature of this calculation leaves a discrepancy between the strain energy at equilibrium as calculated above and the FEA result. To ensure consistency, the strain energy surface is multiplied by an order one constant to make the strain energy at equilibrium equal to the FEA results.

### Piezoelectric Terms

Terms containing piezoelectric coupling and capacitive energy storage are:

$$U_{piezo} = -\frac{1}{2}\int_V \epsilon\, E^2\, \mathrm{d}V - \int_V e\, \varepsilon\, E\, \mathrm{d}V. \tag{4.62}$$

The first term captures the electrical energy stored in the capacitance of the piezoelectric material, which can be expanded as

$$\frac{1}{2}\int_V \epsilon\, E^2\, \mathrm{d}V \approx \frac{\epsilon\, E_B^2}{2}\left[\int_{P_1} \mathrm{d}V + \int_{P_2} \mathrm{d}V\right] + \frac{\epsilon\, E_S^2}{2}\int_{P_3} \mathrm{d}V, \tag{4.63}$$

where $P_1$ and $P_2$ are the two piezoelectric layers of the bimorph, and $P_3$ is the single layer section of the beam. Separate electrical circuits are defined on the bimorph section and the single layer section, therefore the electric field variable has been divided into two contributions, one from each beam section. Calculation of capacitive energy storage is easily accomplished utilizing the volume of each piezoelectric beam. The coupling between the mechanical and electrical domains is contained in the second term and can

be expanded as

$$\int_V e\,\varepsilon\,E\,\mathrm{d}V \approx E_B\left(e_1\int_{P_1}\varepsilon\,\mathrm{d}V + e_2\int_{P_2}\varepsilon\,\mathrm{d}V\right) + e_3\,E_S\int_{P_3}\varepsilon\,\mathrm{d}V. \tag{4.64}$$

Note that the piezoelectric coupling coefficient $e$ has been separated into different values for each section of the beam. The absolute value of this parameter is the same for all three layers, but due to coupling directions and orientation, the sign of the coefficient can change. In the single layer section, we will define $e_3$ as the same as the coupling constant $e$. In the bimorph section, the coupling in the two layers is reversed, so we will define $e_1 = e$ and $e_2 = -e$. This produces

$$\int_V e\,\varepsilon\,E\,\mathrm{d}V \approx e\left[E_B\left(\int_{P_1}\varepsilon\,\mathrm{d}V - \int_{P_2}\varepsilon\,\mathrm{d}V\right) + E_S\int_{P_3}\varepsilon\,\mathrm{d}V\right]. \tag{4.65}$$

The contribution from the single layer is the electric field times the membrane stretch. This integral will be converted to a quadratic polynomial of the mode amplitudes by generating linear combinations of the mode shapes, which is accomplished by calculating the arclength ($s$) of the resulting shape, dividing by the natural length to calculate the stretch ratio, then taking the natural logarithm of the stretch ratio to determine the volume average axial strain:

$$s(a_0, a_1, ..., a_n) = \int_{L_S}^{L}\sqrt{1 + \left(\frac{\partial u}{\partial x}\right)^2}\,\mathrm{d}x, \tag{4.66}$$

$$\frac{1}{V}\int_{P_3}\varepsilon\,\mathrm{d}V = \ln\left(\frac{s(a_0, a_1, ..., a_n)}{L_0}\right), \tag{4.67}$$

where $L_0$ is the natural, unstretched length of the beam. Repeating the above process to span the expected mode amplitudes generates a surface which is fit with a quadratic

polynomial with the mode amplitudes as the independent variables:

$$\int_{P_3} \varepsilon \, \mathrm{d}V \approx c_1 + [c_3] : [\underline{a}^T \underline{a}], \tag{4.68}$$

where ':' indicates a matrix dot product, or Frobenius inner product. The $d_{33}$ beam is configured such that a voltage difference is detected at the electrodes in response to an axial deformation; in the bimorph beam this causes a voltage to develop at the electrodes in response to a bending deformation, and we realize cancellation of any contribution from an axial load. Therefore to leading order the mode amplitudes will affect this integral in a linear fashion:

$$\int_{P_1} \varepsilon \, \mathrm{d}V - \int_{P_2} \varepsilon \, \mathrm{d}V \approx \underline{a} \cdot \underline{c_2}, \tag{4.69}$$

where $\underline{c}$ is a vector of coefficients. The integrals on the left hand side of this equation can be evaluated at various combinations of amplitudes, and this provides solutions for these coefficients. The total potential energy can now be expressed as

$$\begin{aligned} U \approx & -2\beta \, a_0^2 + \beta \, a_0^4 + \Omega - \frac{\epsilon \, E_B^2}{2} \left[ V_{P_1} + V_{P_2} \right] + \frac{\epsilon \, E_S^2}{2} V_{P_3} \\ & - e \left[ E_B (\underline{a} \cdot \underline{c_2}) + E_S \left( c_1 + [c_3] : [\underline{a}^T \underline{a}] \right) \right]. \end{aligned} \tag{4.70}$$

## 4.4 EOM and Testing

With the kinetic energy as defined in (4.44), and the potential energy defined as (4.70), a Lagrangian function will be used to derive equations of motion based on the mode amplitudes. The Lagrangian $\mathcal{L}$ is computed as the kinetic energy minus the potential energy, and the equations of motion are generated via the Euler-Lagrange equation as

[47]:

$$\frac{\mathrm{d}}{\mathrm{d}t}\left(\frac{\partial \mathcal{L}}{\partial \dot{a}_i}\right) - \frac{\partial \mathcal{L}}{\partial a_i} = \zeta_i \dot{a}_i(t) \qquad i = 0, ..., n \tag{4.71}$$

$$\frac{\mathrm{d}}{\mathrm{d}t}\left(\frac{\partial \mathcal{L}}{\partial \dot{F}_j}\right) - \frac{\partial \mathcal{L}}{\partial F_j} = \frac{\dot{F}_j}{R_j} \qquad j = B, S, \tag{4.72}$$

where $F$ is the time integral of the voltage, $v$, called the flux linkage ($v_j = \dot{F}_j$). The terms on the right side of the equations represent losses in the system. Modes of the system are assumed to have damping losses proportional to their velocity, $\zeta_i$ corresponding to the $i^{th}$ mode. Current flowing out of the system removes energy from the electrical portion. Deriving a model using a buckled equilibrium shape plus the first three mode shapes

(referred to as a three mode model), we produce equations of the form:

$$
\begin{aligned}
\ddot{a_{i-1}} =& b_{(i,1)}\, a_0 + b_{(i,2)}\, a_0^3 + b_{(i,3)}\, a_1 + b_{(i,4)}\, a_0\, a_1^2 + b_{(i,5)}\, a_1^3 \\
&+ b_{(i,6)}\, a_2 + b_{(i,7)}\, a_0\, a_1\, a_2 + b_{(i,8)}\, a_1^2\, a_2 + b_{(i,9)}\, a_0\, a_2^2 \\
&+ b_{(i,10)}\, a_1\, a_2^2 + b_{(i,11)}\, a_2^3 + b_{(i,12)}\, a_3 + b_{(i,13)}\, a_0\, a_1\, a_3 \\
&+ b_{(i,14)}\, a_1^2\, a_3 + b_{(i,15)}\, a_0\, a_2\, a_3 + b_{(i,16)}\, a_2^2\, a_3 \\
&+ b_{(i,17))}\, a_0\, a_3^2 + b_{(i,18)}\, a_1\, a_3^2 + b_{(i,19)}\, a_2\, a_3^2 + b_{(i,20)}\, a_3^3 \\
&+ b_{(i,21)}\, A\, \omega^2 \sin \omega t + b_{(i,22)}\, v_B + b_{(i,23)}\, a_0\, v_S \\
&+ b_{(i,24)}\, a_1\, v_S + b_{(i,25)}\, a_2\, v_S + b_{(i,26)}\, a_3\, v_S \\
&+ b_{(i,27)}\, \dot{a_0} + b_{(i,28)}\, \dot{a_1} + b_{(i,29)}\, \dot{a_2} + b_{(i,30)}\, \dot{a_3}, \qquad (4.73) \\
\dot{v_B} =& d_0\, \dot{a_0} + d_1\, \dot{a_1} + d_2\, \dot{a_2} + d_3\, \dot{a_3} + d_4\, v_B, \qquad (4.74) \\
\dot{v_S} =& \dot{a_0}(h_0\, a_0 + h_1\, a_1 + h_2\, a_2 + h_3\, a_3) \qquad (4.75) \\
&+ \dot{a_1}(h_4\, a_0 + h_5\, a_1 + h_6\, a_2 + h_7\, a_3) \\
&+ \dot{a_2}(h_8\, a_0 + h_9\, a_1 + h_{10}\, a_2 + h_{11}\, a_3) \\
&+ \dot{a_3}(h_{12}\, a_0 + h_{13}\, a_1 + h_{14}\, a_2 + h_{15}\, a_3) + h_{16}\, v_S,
\end{aligned}
$$

where $b$ is a matrix of coefficients with as many rows as shape functions, and $d$ and $h$ are vectors of coefficients. The matrices used for this examination can be found in Appendix C. This three mode model consists of 10 degrees of freedom: eight for the shape functions and two for the piezoelectric voltages. The primary motivation for generation of this model is to replicate the behavior that generates the transition to high power output to allow further dynamic analysis and optimization of the system. Therefore, the modes are selected by determining the minimum number required to replicate experimental behavior while keeping the degrees of freedom within the range which can be dynamically analyzed.

| Mode ($i$) | Damping Ratio ($\zeta_i$) |
|---|---|
| 0 | $1 \times 10^{-11}$ |
| 1 | $12 \times 10^{-8}$ |
| 2 | $2 \times 10^{-7}$ |
| 3 | $2 \times 10^{-5}$ |

Table 4.3: Damping ratios prescribed to provide interwell behavior at similar excitation level to experimental observations.

| Eigenvalues at equilibrium |
|---|
| -76015 |
| -55787 |
| -27893 |
| -4.73 |
| -49.05±2185$i$ |
| -75.67±719.3$i$ |
| -16.84±130.5$i$ |

Table 4.4: Eigenvalues of Jacobian matrix at stable equilibrium.

### 4.4.1 Model Analysis

Evaluation of the model requires determination of damping coefficients. Experimental results are not indicative of modal damping ratios, so coefficients have been adjusted to match the input power level at which inter-well oscillations begin, while ensuring that higher mode numbers are increasingly damped and the unforced system when perturbed returns to equilibrium quickly. The resulting coefficients can be seen in Table 4.3. Evaluation of the Jacobian matrix at one of the stable equilibrium positions shows that this system is stiff, with the eigenvalues presented in Table 4.4. To deal with this, a backwards differentiation formula is used for numerical integration, with an analytic Jacobian to aid in convergence.

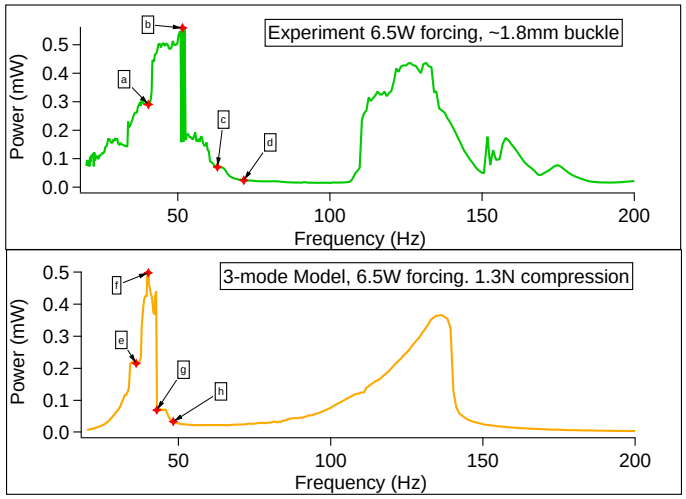


Figure 4.4: A comparison of the power output of the experiment and the predicted output of the model. Points marked as a through h will be used to compare dynamic behavior of the experimental system and the model, as shown in Figure 4.5.

## 4.5 Comparison with Experimental Results

The comparison of power output of the model and experiment, both in response to 6.5 watts of input power, can be seen in Figure 4.4. The experimental setup is buckled to a transverse maximum displacement of approximately 1.8 mm with an error bound of approximately 0.5 mm, while the model is specified to have a compressive force of 1.3 N, which results in 1.34 mm maximum transverse deflection, which is within the error bound of the experiment. Perfect agreement of results is not expected due to the complex nature of the system and the severe truncation associated with our low order model. Nevertheless every attempt has been made in the model to keep results for all parameters within the expected error bounds of the experiment. Phase portraits for dynamic comparison are constructed by plotting the voltage measured across the single layer beam against the voltage measured across the bimorph. The system is first allowed to evolve for several seconds to allow any transient to die out, then when a consistent behavior is seen, data are gathered by measuring the voltage across a 2.2 kΩ resistor.

The system is then strobed at the forcing frequency to create a Poincaré map, which is overlaid on the phase portrait. These plots are shown in Figure 4.5, and it can be seen that similar behavior in the chaotic region occurs in the model and the experiment. The system starts as a twisted period-1 orbit which repeats indefinitely as seen in panels $a$ and $e$ of Figure 4.5. As the forcing frequency is increased there is a torus which loses any recognizable structure and ceases to repeat itself, resulting in chaotic behavior as seen in panels $b$ and $f$. Further increase of the forcing frequency returns to a twisted periodic orbit (panels $c$ and $g$), which simplifies and untwists until a much simpler period-1 orbit is achieved which persists throughout the low power region, as seen in panels $d$ and $h$. Note that the experimental system contains much more high frequency content than the model; however the model successfully captures the essential behavior of the system.

The power output of the model is indicated as being slightly lower than is measured in the experiment, which is most likely due to the use of the nominal piezoelectric coupling coefficient, which is expected to have some variation. Note that the high power output frequencies for the model and experiment are slightly different, but indicate the same sort of behavior around the high power output areas. The lower frequency peak exhibits shoulders around the highest output area in both model and experiment, but the model does not have quite as much bandwidth as the experimental peak. This is presumably due to the severe truncation in the model used to reduce the system from infinite dimensional to ten degrees of freedom. The second peak around 120-140Hz also demonstrates wider bandwidth for the experiment than the model, and any higher frequency peaks are very attenuated in the model. As the driving frequency of the system increases, the number of modes required to capture the behavior seen in the experiment goes up. However, our model has been truncated to allow accurate analysis of the lowest lobe of power output. In spite of these discrepancies, the model appears to capture the critical behavior of the system and gives a good indication of the power output over a significant frequency

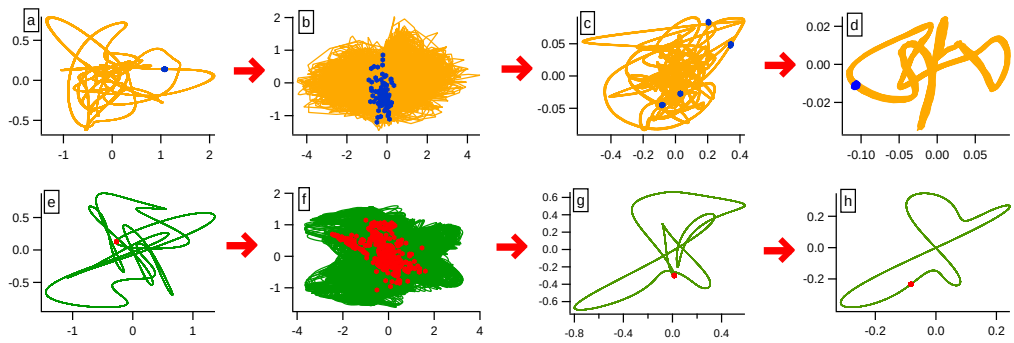


Figure 4.5: Phase plots around a chaotic regime in the experiment and the model. Phase plots are generated with voltage output from the single layer beam on the horizontal axis and voltage from the bimorph on the vertical axis. Poincaré maps are overlaid on phase space plots, and the letter in each panel corresponds to the marked locations in Figure 4.4. Upper plots represent the experiment, lower plots represent the model. At frequencies lower than the chaotic regime, both have a complex period-1 orbit. Increasing the forcing frequency causes chaotic behavior, producing phase plots and Poincaré maps that appear to have no structure. Continued increase of the forcing frequency returns the behavior to a periodic response, which simplifies as the forcing frequency moves further above chaos until a relatively simple period-1 orbit is achieved.

range.

### 4.5.1 Model Conclusions

A model has been generated for a complex, nonlinear energy harvesting system. Finite element analysis was used to determine a basis for projecting the system dynamics onto, as well as a reference for stresses and strains in the equilibrium positions. This approach allows a system to be modeled when analytic solutions are unavailable. It was found that to properly capture the small strain snap-through effects of the system, it is necessary to keep several modes in addition to the buckled equilibrium shape so that the system never passes through the flat, unstable equilibrium where the strains would be relatively high. The model demonstrates good quantitative agreement with the power output of the experiment in both power level and frequency of occurrence. Experimental transitions

between dynamic behavior patterns are replicated closely, indicating that the model is appropriate for dynamic analysis of the underlying phenomena. We note that nominal material parameters are used in this chapter; it was not necessary to tune these for better agreement. Overall, the model provides a source for understanding and optimizing energy harvesting ability with a system that exhibits a much broader response than a linear resonator.

# Chapter 5

# Analysis of the Model

We propose that the critical parameters for examining a nonlinear energy harvesting system are the forcing power level and the frequency and/or bandwidth of excitation. Commonly, comparisons are made using the amplitude of the acceleration of the forcing signal, without regard to the fact that the forcing power level is not constant or linear as the frequency is changed when the acceleration amplitude is kept constant. This results in higher frequency tests being done at significantly higher forcing power levels which can skew the results to appear that the device works just as well or better at higher frequencies, particularly damaging the perception of output bandwidth. The lack of superposition in nonlinear devices compounds this phenomenon. Sweeps at constant acceleration often result in overlapping power levels with another sweep which is presented as a separate result, and interpolation or normalization are not possible. Only comparing signals produced by the same input power level allows for a fair comparison of output root mean squared (RMS) values without any skew based on frequency of excitation.

To begin examination of the model, we produce a plot of power output over the parameter space of frequency and available forcing power. This can be seen in Figure 5.1. Here the forcing power is calculated as the forcing amplitude squared multiplied with

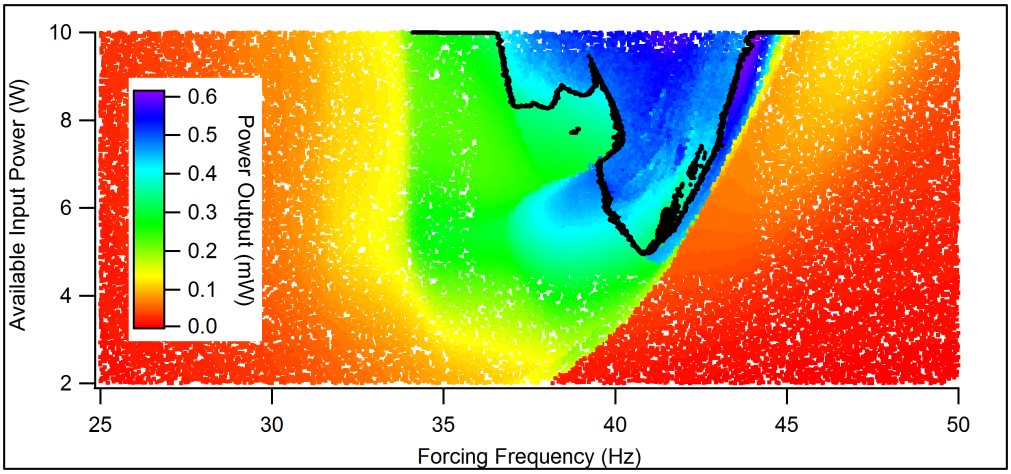


Figure 5.1: Summed RMS power output in mW of both single layer beam and bimorph beam. Note the sharp transition between low and high power on the high frequency side of the tongue. Also note the "bite" that seems to be taken out of the high power region on the low frequency side.

the forcing frequency in $^{\text{radians}}/_{\text{second}}$ cubed. This represents the maximum amplitude of the acceleration multiplied with the maximum value of the velocity, providing a measure of mechanical power. Though these quantities are never at their maxima at the same instant, it provides a consistent and easily calculable reference for which to compare forcing power levels, which we will denote as the available input power. The output power is the sum of the RMS voltage output divided by the resistive load in kilo-ohms for both the single layer and bimorph sections of the beam. Note that there is a region of the parameter space where the power output is significantly higher. This region begins at approximately 5 watts of available input power and a forcing frequency of 41 Hz, where the bandwidth is quite small. As the available input power is increased there is a significant increase of the bandwidth of the high power region. Interestingly, around 7 watts of available input power there is a region where the bandwidth shrinks. This phenomenon is due to the existence of a non-attracting set of high power orbits that settles to a small amplitude orbit after a period of high power transients, as will be shown in more detail later in this paper. The high power region is associated with the

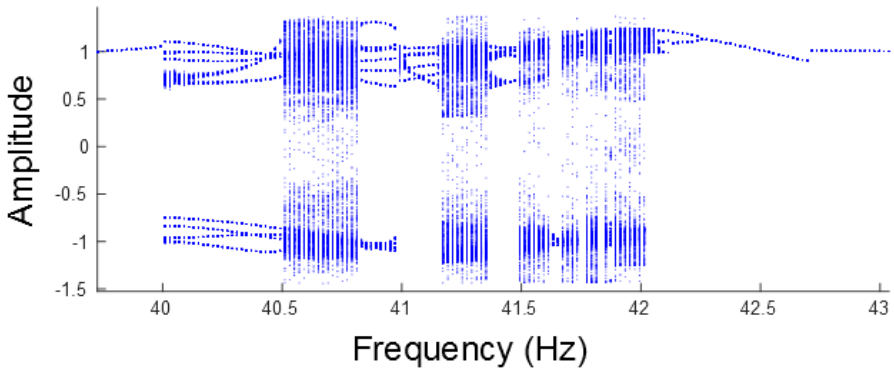


Figure 5.2: Bifurcation diagram created by strobing the system at the forcing frequency. The selected function is the equilibrium amplitude $a_0$, and the available input power is 6 watts. Frequencies with well defined discrete points have periodic solutions, while frequencies where the Poincaré intersections fill in vertical bands of parameter space are chaotic.

beam entering into a behavior which transitions between the two stable equilibria of the buckled beam, which we will call a snap-through behavior. The region of parameter space where the beam exhibits this snap-through behavior can be determined by examining the long-time average of the amplitude of the equilibrium mode [53]. When the beam is settled into single well behavior, the time average is very close to positive or negative one, while during snap-through behavior the time average approaches zero. The black trace in Figure 5.1 represents the boundary of the region where the snap-through behavior represents the attracting set, and all orbits inside the region make well-to-well transitions. Note that while this encompasses a large portion of the high power region, there is a significant slice on the high frequency side where high power output is realized without snap-through behavior, as well as a small lobe on the low frequency side. These regions will be examined later in the paper.

## 5.1 Bifurcation Diagrams

For a specified available input power level, a bifurcation diagram can be created. To do so, a range of frequencies is selected with adequate density to catch interesting phenomena, and a time series is run at each chosen excitation frequency. After discarding any transient portion, a Poincaré section is created by strobing the time series once per forcing period. Selecting one representative function and plotting the amplitude of that function across the frequency range, a bifurcation diagram is generated; see Figure 5.2. For this example, an available input power level of 6 watts has been selected, and the function we are examining is the amplitude of the equilibrium mode, $a_0$. Periodic behavior is expected to have all of the Poincaré iterates lie on top of each other, and are therefore expected to correspond to a point or a well defined set of points at the respective frequency. Beginning at the far right of the diagram, a period one oscillation is noted for which a demonstrative time series can be seen in Figure 5.3(a). Decreasing the forcing frequency results in this behavior splitting into a period two oscillation, as seen in Figure 5.3(b), suggesting the existence of a period doubling cascade, which will be examined shortly. Moving further down in frequency, chaotic response is found first in just one well, panel (c), then the attractor expands until it fills the well, then snap-through behavior begins with the attractor visiting both wells indiscriminately, see panel (d). This behavior suggests that the transition from single well behavior to snap-through behavior is governed by an *attractor merging crisis* [54] of the symmetry related attractors in each well. Traveling for a while through the chaotic zone, suddenly a periodic window is encountered. A time series with Poincaré map can be seen in panel (e) of Figure 5.3. Further reduction in frequency carries us through several more chaotic zones and periodic windows before we return to a period one oscillation. Note that at approximately 42.7 Hz in Figure 5.2 there is a discontinuity in the bifurcation branch of the period one orbit.

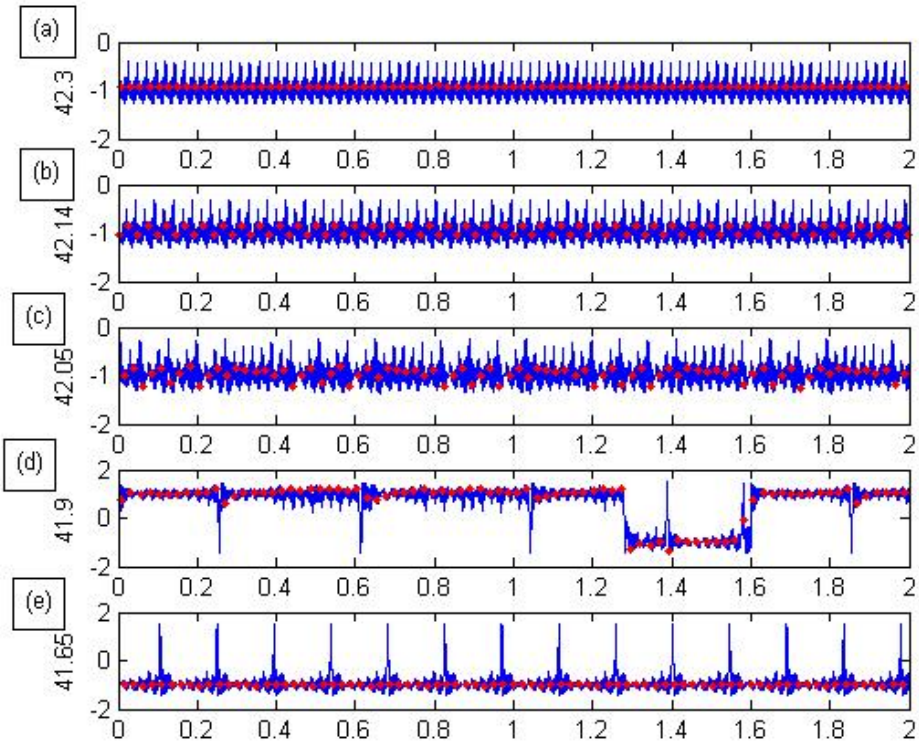


Figure 5.3: A set of time series demonstrating qualitatively different behaviors. All plots are of the equilibrium mode amplitude, with red dots overlaid at the Poincaré sections used to create the bifurcation diagrams. Panel (a) demonstrates a simple period 1 orbit which exists at 42.3 Hz. As the frequency is decreased to 42.14 Hz, the orbit becomes period 2, as seen in panel (b). Chaos is first noted in a single well, as shown in panel (c) at 42.05 Hz. Quickly this chaotic attractor merges with the attractor existing in the other well, and snap-through behavior is noted, as seen in panel (d) at 41.9 Hz. Moving down in forcing frequency through the chaotic zone, a periodic window is encountered, as seen in panel (e) at 41.65 Hz.

To determine the cause of this irregularity, we can use the numerical bifurcation software AUTO [55] to follow the development of the period one orbit as we move through this range of forcing frequencies. We will start on the stable period one orbit above the discontinuity, and follow the orbit as the forcing frequency is decreased. We find that there is a region where multiple saddle-node bifurcations create multiple stable orbits. Figure 5.4 shows the evolution of the orbit through this frequency range. The red portions of the trace are the unstable branch of the period one orbit, while the blue portions are stable. The vertical axis represents the $L^2$ norm of the voltage produced by this orbit, so higher values are associated with higher power output. We note that between 42.39 and 42.71 Hz, there are multiple stable instances of this period one orbit, connected through 4 saddle-node bifurcations (marked with black triangles on the figure). While the intermediate stable orbit is not easily discovered with a time series exploration, the low power and high power branches are both easily observed, and the switch between them is what causes the discontinuity observed in Figure 5.2. Moreover, this jump between stable orbits is the cause of the sudden jump in output power noted at the high frequency side of the high power region in Figure 5.1. The stable high power branch of the orbit doesn't exist for long before it loses stability at a period doubling bifurcation (such bifurcations are marked with black squares). The period doubled stable solution can be traced to a second period doubling bifurcation, where a new branch leads to a third bifurcation, and quickly the orbit becomes too complex and the bifurcations too close together to identify any further, accumulating at approximately 42.075 Hz. Recall that the Feigenbaum number ($\delta$) can be calculated as

$$\lim_{n\to\infty} \frac{\lambda_n - \lambda_{n-1}}{\lambda_{n+1} - \lambda_n} = \delta \to 4.6692016, \tag{5.1}$$

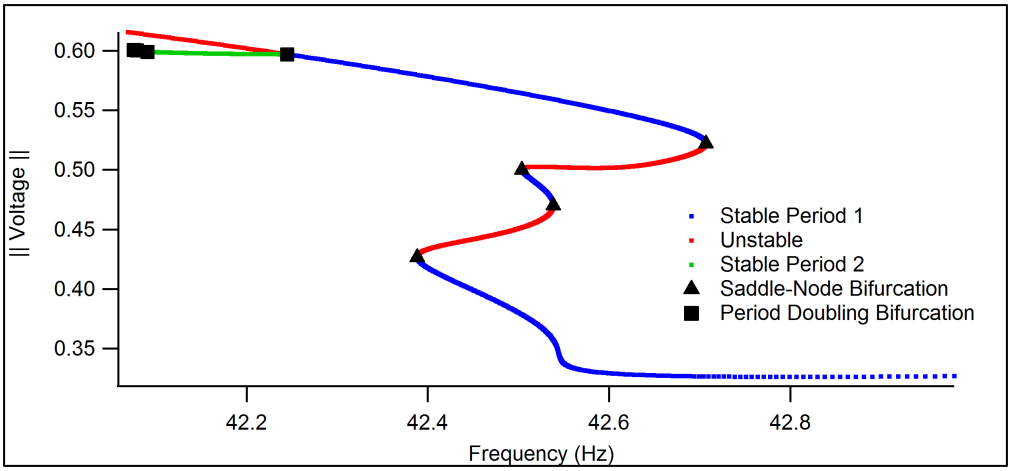


Figure 5.4: Evolution of the period one orbit at the high frequency side of the high power region. Blue traces indicate regions of stability of the period one orbit, the green trace is a stable period two orbit, while the red lines indicate unstable branches. Saddle node bifurcations are marked with black triangles, while period doubling bifurcations are marked with black squares. The existence of multiple stable orbits at different power output levels provides insight to the sudden change of output power observed here. The period doubling cascade at the far left of the figure indicates the transition to chaotic behavior.

where $\lambda_n$ represents the frequency at which the $n^{th}$ bifurcation occurs [13] [56]. For the present model this is calculated as 4.5 for the fourth period doubling bifurcation ($n = 4$), which is reasonable close to the Feigenbaum number, suggesting that this period doubling cascade obeys the universal scaling expected of a period doubling transition to chaotic behavior. The period one orbit can be traced through the high power region, where it remains unstable, until stability is regained as we drop back into single well oscillations near a saddle-node bifurcation on the low frequency side of the high power region, corresponding to 39.6 Hz with 6 watts of available input power. The saddle-node bifurcation appears to trace the boundary, as can be seen in Figure 5.6, along the low frequency side of the snap-through region. However, this bifurcation branch is not responsible for the transition. There is a very small region where both the stable period one orbit, which undergoes the saddle-node bifurcation, and the chaotic attractor coexist. Furthermore, a time series including the transient portion can be seen in Figure 5.5. The

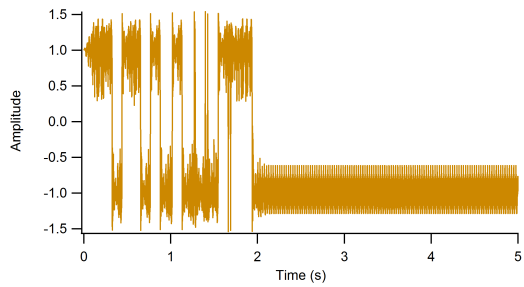


Figure 5.5: On the low frequency side of the high power region, transient snap-through behavior can be observed before the system settles into a single well oscillation. This time series plots the equilibrium mode amplitude, with a forcing frequency of 39.7 Hz, and an available input power of 6 watts.

transient portion produces snap-through behavior in a manner similar to trajectories where snap-through is the attracting behavior. The overlap of stable period one and chaotic regions combined with the presence of transient chaos indicates that an unstable orbit has collided with the chaotic attractor, creating a boundary crisis [57]. The chaotic set becomes non-attracting, but orbits near the boundary are able to jump onto this set for a short period of time before moving off to a stable period one orbit. Therefore, we see a high power output transient that settles to a low power output long term behavior. Presumably small perturbations to the system could result in returning to the high power non-attracting set through this region. Though all of this bifurcation analysis has been developed at an available input power level of 6 watts, these phenomena persist across the span of the high power region. Using AUTO to trace the bifurcation branches through the frequency/available power parameter space and plot them on top of the power output allows us to trace the boundaries of the high power region very accurately. Figure 5.6 shows this, where saddle node branches are traced in black, period doubling branches in red, and the region of transient chaos highlighted in brown. Note that the region of transient chaos fills in the "bite" of low power output noted around 7-8 watts of available input power. There is a high power lobe that occurs outside of the snap-through region on the low frequency side, between about 5 and 7 watts of available input power. This is

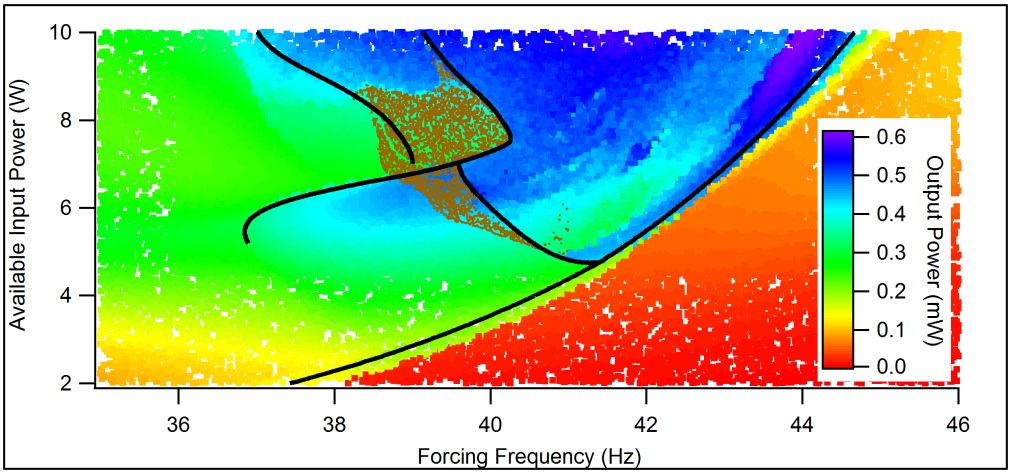


Figure 5.6: Power output over the parameter space, with bifurcation sets shown. Black lines are associated with saddle-node bifurcations, and the red line is a period doubling bifurcation at the start of the period doubling cascade. The brown highlighting indicates regions of transient chaos. The majority of the high power output region is enclosed by the saddle-node bifurcations.

also traced by a saddle-node bifurcation, indicating that there is a sudden change from a low power output behavior to a high power output behavior.

## 5.2 Periodic Windows

It is informative to examine the periodic windows that exist within the chaotic region. Reviewing Figure 5.2, we note that there are several windows where the period is quite high. By measuring the time elapsed between crossings of the equilibrium mode through zero in the positive direction, and averaging over a comparatively long time period we can define an average crossing frequency. Plotting this for a sweep at 6 watts of available input power, and overlaying integer multiples of the forcing frequency produces Figure 5.7. Note that there are several regions where the frequency of the well-to-well oscillations is locked to the forcing frequency. This is particularly obvious in this figure between 40 and 40.5 Hz, where the oscillations are locked at 9 periods of the forcing

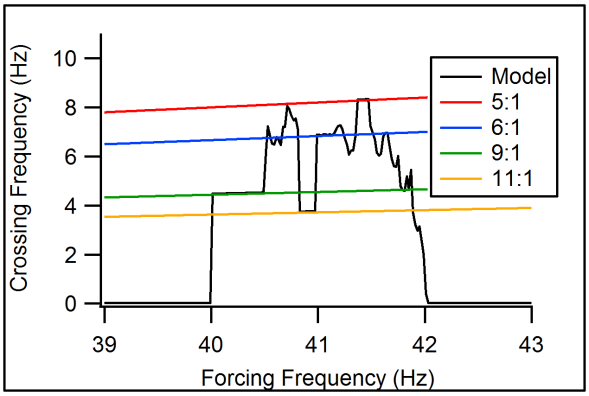


Figure 5.7: Frequency locking in the well-to-well oscillation zone. Any time we are experiencing well-to-well oscillations, this frequency is non-zero. Note the regions where the crossing frequency locks to the forcing frequency. Locked oscillations of several different periods are present, ranging from 5 forcing cycles up to 11.

cycle. Note also that Figure 5.2 indicates that the periodic windows exist at the same frequencies which indicate a lock between the forcing frequency and the response of the system. Moreover, the integer relation to the forcing frequency is coincident with the periodicity of the associated window. This phenomenon can be visualized through Figure 5.8, where the periodic windows have been highlighted in a color pattern consistent with their periodicity as determined from the locking behavior. In this plot, we have stacked multiple bifurcation diagrams together to give a sense of the development of the periodic windows and snap-through regions throughout the parameter space. Interestingly, we note that the relatively low period orbits only occur at higher power levels, with higher periodicities being present at lower available power levels. The expansion of the chaotic region with its interspersed periodic windows is clearly apparent from this perspective. The development of the chaotic region is closely associated with snap-through behavior, as evidenced by the fact that nearly all chaotic frequencies have strobe points in both wells. Therefore it is reasonable to assume that for this beam, the chaotic attractor becoming stable results in high power output, though it is possible to achieve high power output without a chaotic attractor. The transition between periodic and chaotic be-

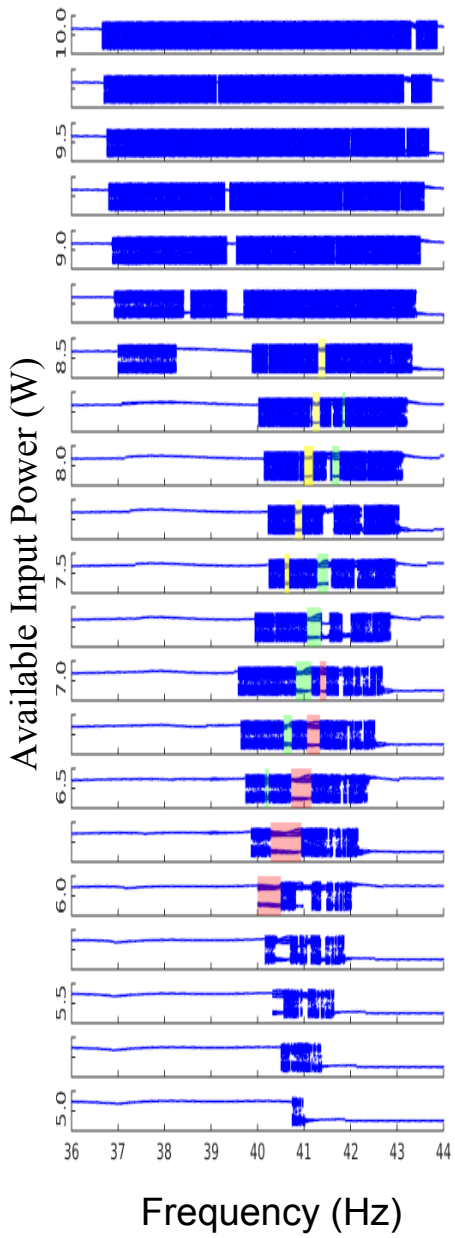


Figure 5.8: Stacked bifurcation diagrams of the equilibrium mode show the evolution of the snap-through region. Here some of the major periodic windows are highlighted: yellow corresponds to a period 5 oscillation, green to a period 7, and red to a period 9. As the available input power level is decreased, the trend is towards higher period periodic windows.

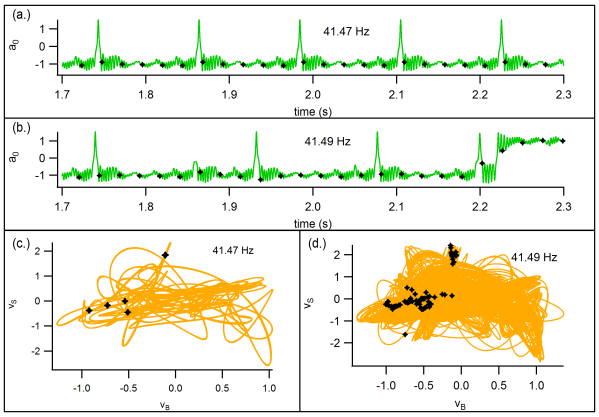


Figure 5.9: Upper panels show time series of periodic response at 41.47 Hz, and chaotic response at 41.49 Hz. Lower panels phase space of period 5 oscillation at 41.47 Hz, and the response at 41.49 Hz where the Poincaré sections no longer form a periodic orbit. Note that the behavior of the chaotic series is very similar to the periodic response with bursts of different behavior interspersed that prevents the Poincaré map from repeating.

havior within the chaotic attractor deserves some attention. A time series of a period 5 window with overlaid Poincaré map and a time series of a chaotic response very close in frequency is displayed in Figure 5.9. The phase portraits associated with each trajectory are also presented. The chaotic time series has sections that appear to behave in a very similar way to the periodic time series. However, there are intermittent bursts of aperiodic behavior that prevent the Poincaré map from repeating as it does in the periodic case. From this it can be inferred that the transition between periodic behavior and chaotic behavior is governed by an intermittency transition around these periodic windows.

## 5.3 Wideband Forcing

In the experimental exploration of this beam shown in Chapter 3, a wide band excitation was used to explore the performance in response to a more realistic vibration source than a single frequency sinusoid. To generate this excitation, white noise is generated

and bandpass filtered to allow only specific frequencies. Specifically, a central frequency is selected, then the bandpass filter is set to allow a range of $\pm 1$ Hz around the central frequency, with a $12^{th}$ order crossover. A representative example of the time series produced by this method as well as the associated frequency spectrum and resulting output can be seen in Figure 5.10. Spreading the power across several frequencies requires a higher input power level to achieve a comparable output power level with the single sinusoid forcing, but it can be noted from Figure B.5 that the bandwidth is much wider in response to this more complex forcing than it is with a single frequency sinusoid, particularly on the high frequency side of the high power region. The regions of transient chaos observed in Figure 5.6 have blended into the high power region. It can be noted from Figure 5.10 that the beam does not exhibit continuous snap-through behavior in response to this excitation, rather it snaps through in response to the large amplitude sections of the forcing signal. Due to the time-varying nature of a non-sinusoidal forcing signal, any sort of behavior can be viewed as transient so the distinction between attracting and non-attracting chaotic sets has been blurred to the point of becoming indistinguishable.

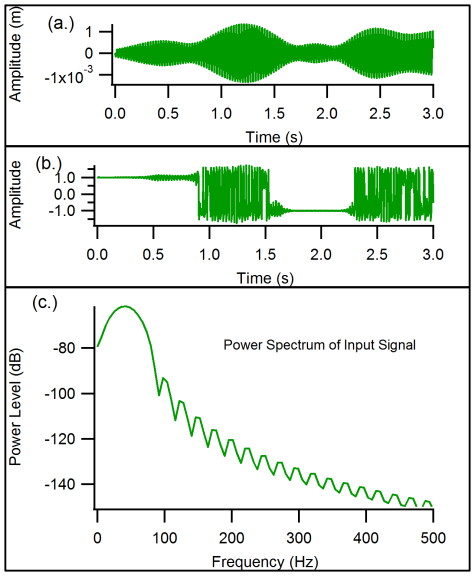


Figure 5.10: Panel (a) demonstrates a time series of the widened band forcing, with the power spectrum of this input shown in panel (c). The resulting amplitude of the equilibrium mode from this input is shown in panel (b). For this combination, the input RMS power is 5.4 watts, with an output RMS power of 0.35 mW. Note that the widened band forcing signal has a beating effect where the forcing amplitude goes through low amplitude sections and high amplitude sections. Unsurprisingly, the beam responds with single well oscillations during the small amplitude portions, and snap-through behavior during the large amplitude sections.

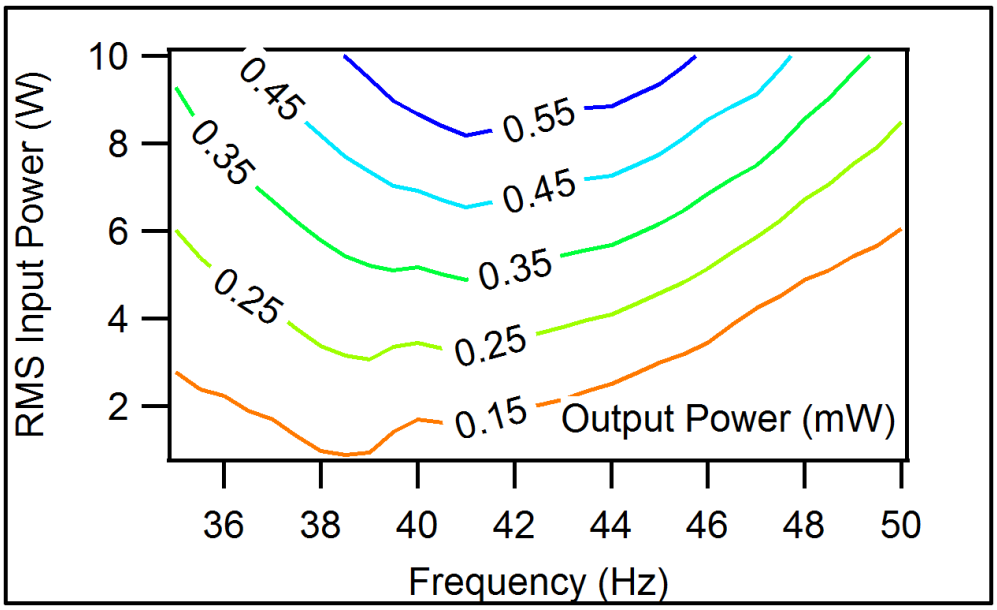


Figure 5.11: Contour plot of power output in response to widened band forcing signal. Contours are labeled with the associated power output in mW.

# Chapter 6

# Conclusions and Future Work

In this document we have developed a device which is capable of harvesting vibrational energy over a greater bandwidth than a linear resonant device. Experimental results presented in Chapter 3 demonstrated this, and indicated that this device was particularly attractive when used to harvest energy from broad spectrum forcing signals. The next step was to develop a model of the system, so we started by attempting to use established methods for buckled beams in Section 4.1, and found that the assumptions made in this process were not compatible with the buckling levels we wanted to achieve, and were therefore unacceptable for use as a dynamic model. As an alternative approach, the finite element analysis software ABAQUS was used to produce both the buckled equilibrium shape and linear modes about the nonlinear operating point, as was presented in Section 4.2. This information was used to develop energy equations based on the mode amplitudes in Section 4.3, and then finally compared to experimental results in Section 4.5, where good agreement for the different modes of operation is shown between the model and the experimental results.

Analysis of this beam model in Chapter 5 indicates that the presence of a chaotic attractor results in a relatively high power output. The chaotic attractor is associated

with a period doubling cascade, an itermittency transition, and a crisis where an unstable period-one orbit collides with the attractor. There are regions where the power output increases without a chaotic attractor, but these areas are bounded by saddle-node bifurcations which are the start of a transformation of behavior which will result in a chaotic attractor when the parameter of interest continues to evolve. The resulting high power bandwidth is much greater than can be realized with a linear oscillator, and performs particularly well in response to a widened band forcing signal, indicating that this beam system is particularly well suited to the time varying characteristics that are commonly present in ambient vibrations. This model performs quite well in comparison with other nonlinear energy harvesting devices, though the lack of a well-defined and properly normalized performance metric for other studies makes quantitative comparison very difficult. Analysis of the single-forcing frequency model provides understanding of which transitions result in high power output.

Further investigations of the system should be oriented towards utilizing the characteristics of the model to attempt to *optimize* the beam design in response to some particular figure of merit, such as bandwidth or the integral of the power output, or perhaps to ensure particularly good response to a certain range of forcing frequencies. Due to the disconnect between beam physical parameters and the resulting model, it will be necessary to build any variations of the model as a finite element representation, extract the critical stress and strain values, and regenerate the model. This has been started to the extent of building the models in ABAQUS and extracting the shapes, but generalizing all of the subsequent analysis steps to varying beam parameters will be postponed to future work.

# Appendix A

# Finite Element Setup Process

- Sketch a 3D deformable solid extrusion for the steel beam, approximate size: 0.1.
  - centered on x-axis, extending from 0-L
    - start @ $(0, \frac{-b}{2})$
    - opposite corner @ $(L, \frac{b}{2})$
  - extrude to proper thickness
- repeat above for piezoelectric beam
- create materials and sections for each beam
- assign section to each beam
- Assembly
  - instance piezo
    - translate from (0,0,0) to (0,0,-0.0014)
  - instance piezo
    - translate from (0,0,0) to (0,0,+0.0014)

  - instance steel
  - instance piezo
    * translate from (0,0,0) to ($L_{steel} - L_{overlap}$,0,+0.0024)

- Interaction
  - Define surface-to-surface contact (standard) for all contacting surfaces
  - Create tie constraint for all contact surfaces
- Create electrical BC on interior piezoelectric surfaces
- translate piezo's into contact with appropriate surfaces
- create disp/rotat BC @ bimorph fixed end, constrain all DOF
- create disp/rotat BC @ single layer fixed end, constrain all DOF
- create linear frequency response step in un-deformed condition (9 freqs)
- create static general step NLGeom ON
  - period: 0.1, 1e-15 min, 1e-3 max step, 1e-5 start, 10,000 iteration max
- in BC manager, change sliding end BC to be free in 1 direction
- create pressure load on end of single beam
  - set total force applied
- create frequency step
  - modify BC to fix $U_1$ @ single end
  - add additional general and linear steps as needed

- Mesh
  - seed all 4 long edges @0.001 /element
  - seed all 4 widths @ 2 elements
  - seed height @ 1 element
- create node set on midline of top of beam (named *shapes*)
- create field output request for the first step
  - set:shapes
  - Disp/Vel/Acc/UT/translations
- change element type to quadratic, full integration.

# Appendix B

# Labview

## B.1 Power Level Adjustment Controller

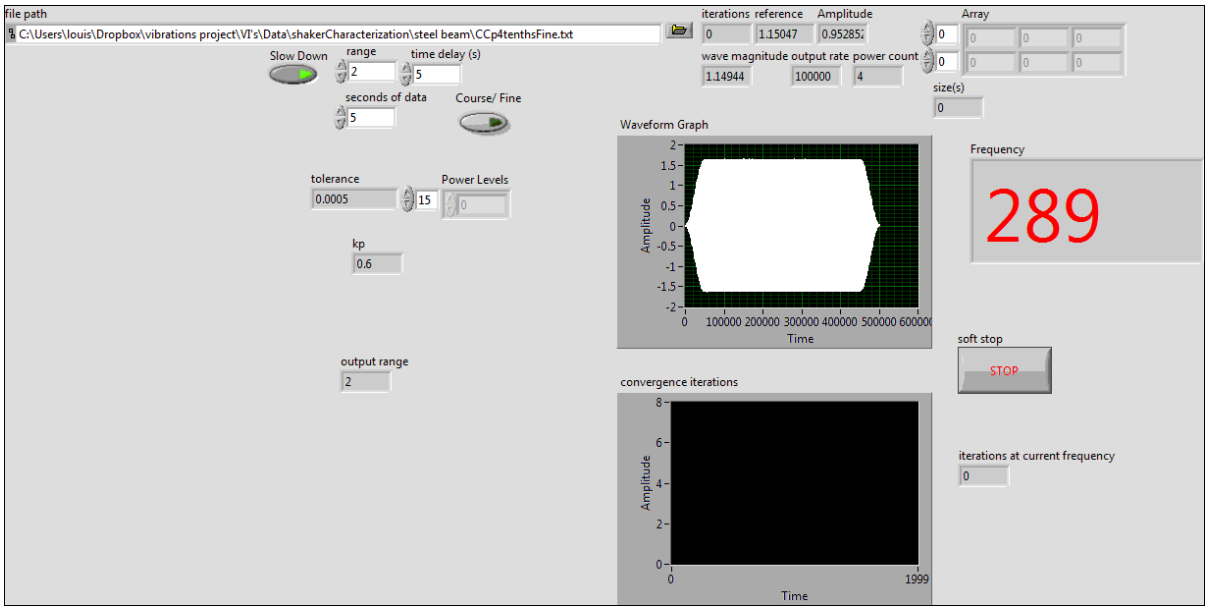


Figure B.1: Interface panel. Displays live data to the user, and allows for user input live updates while running. Here we can adjust the tolerance to which we want to control into, change the amount of time data is gathered for, and other time based adjustments to allow for proper human observation. Displayed statistics include current driving amplitude, reference magnitude, and resulting wave magnitude.

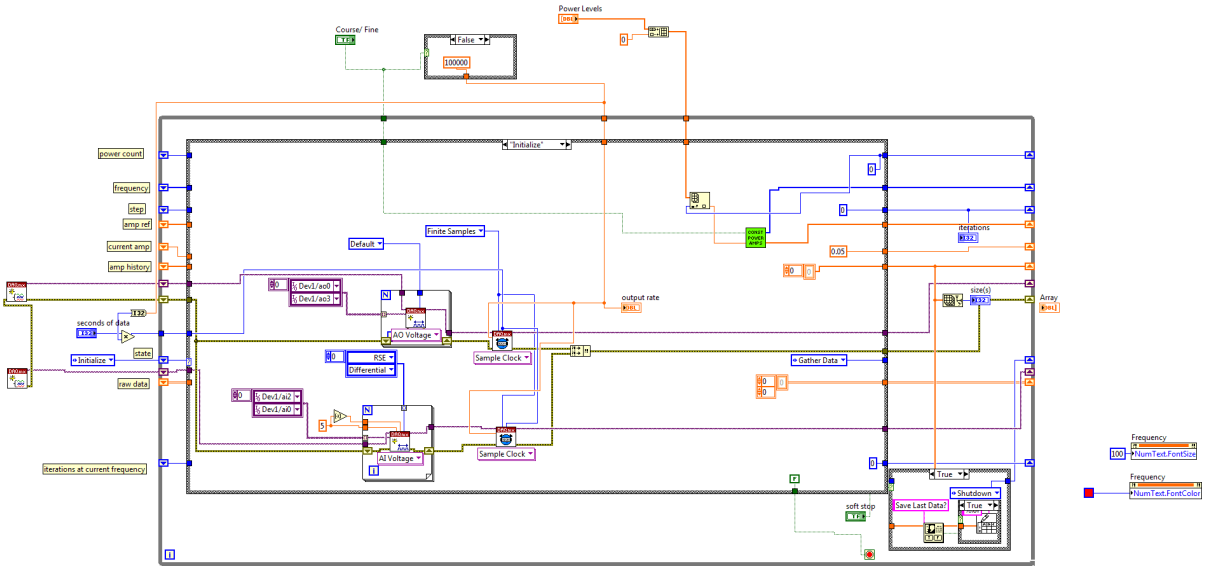


Figure B.2: This image shows the organization of the program and indicates important parameters that are to be stored throughout the execution. The program is structured as a state machine, which starts off with an initialization routine where the interface with the experimental device is started and configured.

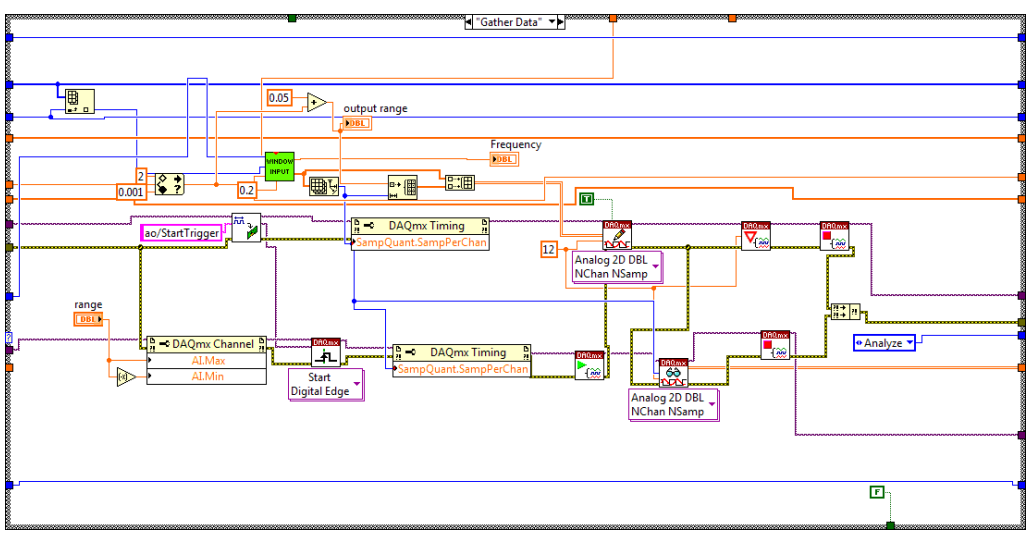


Figure B.3: Contour plot of power output in response to widened band forcing signal. Contours are labeled with the associated power output in mW.

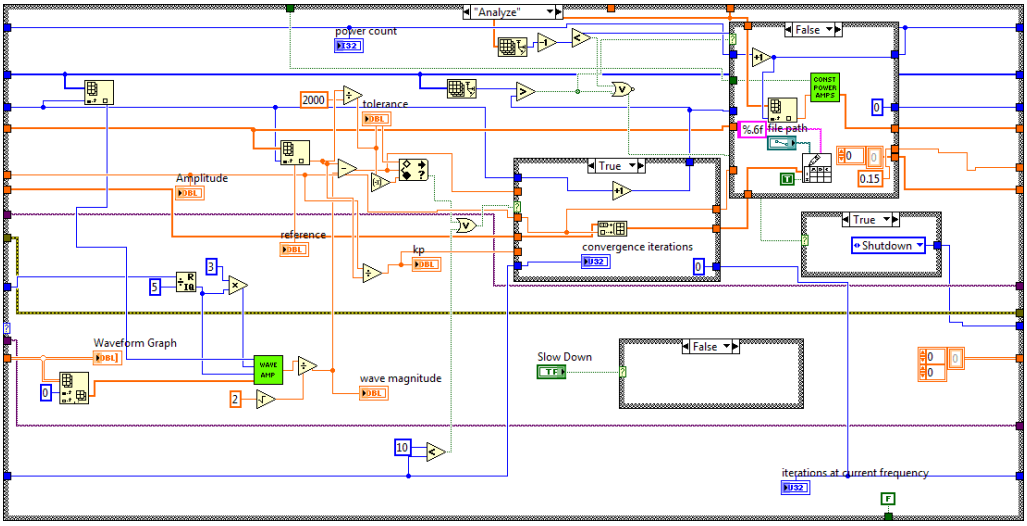


Figure B.4: This state gathers data from the experimental device while syncronizing a signal output. The first writing event triggers the reading to start, and both are run for a specified number of synchronized time steps.

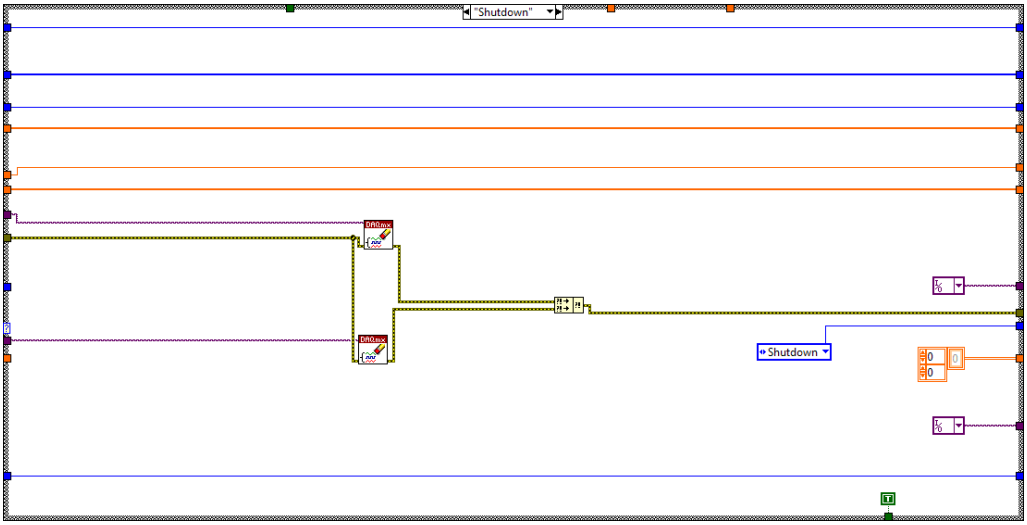


Figure B.5: This state takes the data gathered from the experiment, and decided whether the applied signal resulted in the desired output. If it is within tolerance, we record the acceptable data, change frequency and start over. If the results are out of tolerance, the driving amplitude is adjusted and run again.

## B.2 Raw Data Collection

Figure B.6: The control panel for the raw data collection program. Here we can control the sampling rates of both the input and the output, and we can control how many samples are used to generate the signals. Feedback from the program comes as the current frequency, and some tallies to keep track of where in the program it is at.

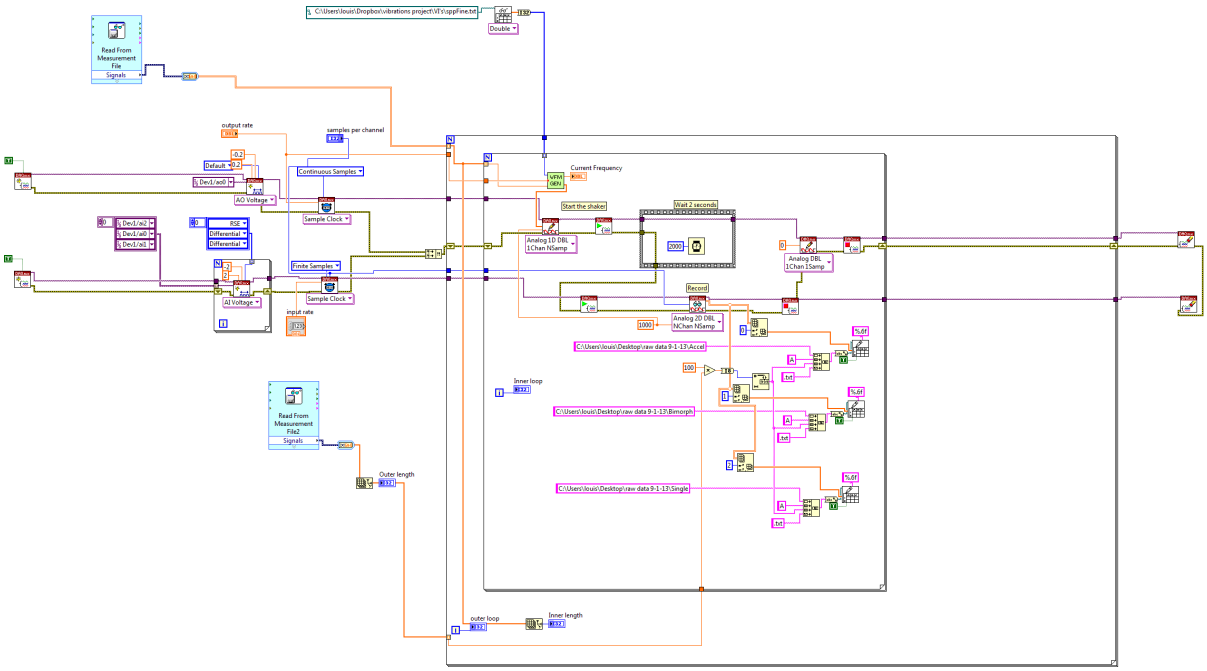

Figure B.7: The operations of this program are quite simple. The appropriate frequency/amplitude pairs produced by the control loop are loaded, the signal is generated, the experiment starts and we wait for two seconds (variable) for transients to die out. Then we gather samples from the accelerometer and both voltage signals, which are then written to data files titled with their source and test number.

## B.3 Amplitude Extraction Program

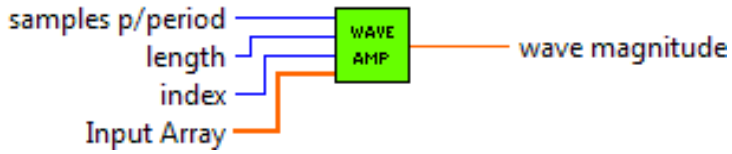


Figure B.8: The cartoon demonstration of this program. It takes in an array of experimental data along with the length of the signal, samples per period of the forcing signal, and the index of the array to be analyzed. The output is the amplitude of the input waveform at the frequency specified by the samples per period input.

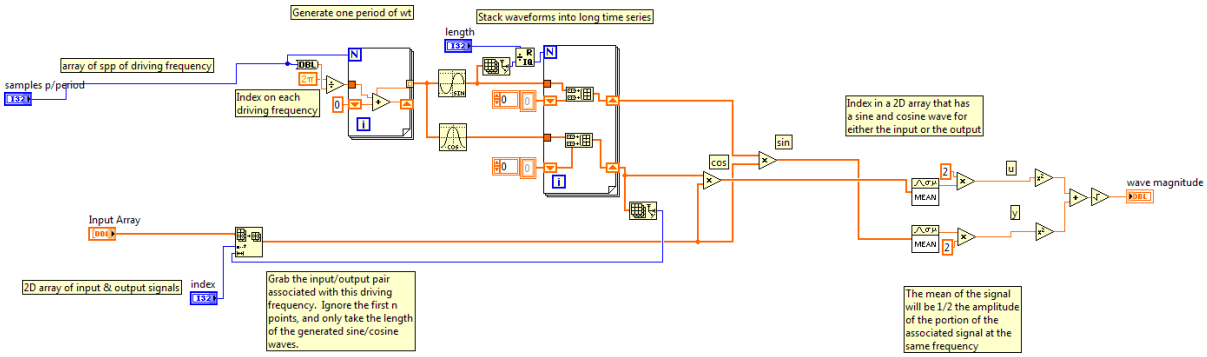


Figure B.9: This vi starts by creating a sine and a cosine wave at the frequency specified by the input samples per period. The desired array is selected via a user selected input, and the signal is multiplied separately by both the sine and cosine waves. From this we average the values over the array, and arrange at the true amplitude at the specified frequency of the selected array.

# Appendix C

# Model Matrices

These are the matrices used to evaluate the model according to equations of motion as dictated by 4.74.

## C.1 "b" matrix

B(:,1-10)=

$$\begin{bmatrix} 4.6792e6 & -4.6792e6 & 3.0868e4 & 1.6238e4 & 5.7772e4 & 4.6283e3 & -8.5506e4 & 1.2149e5 & 5.9335e4 & 2.7958e5 \\ -3.1111e6 & 3.1111e6 & -3.879e4 & -1.2368e4 & -5.6353e4 & -1.5915e4 & 7.1771e4 & -1.3911e5 & -3.9728e4 & -2.8698e5 \\ 2.2135e5 & -2.2135e5 & 3.1832e4 & -1.7494e4 & 1.6094e3 & -3.9363e4 & -5.2679e5 & -2.0004e5 & 2.2235e5 & -3.8841e5 \\ -4.7753e6 & 4.7753e6 & 1.7122e3 & -3.0519e4 & -5.8959e4 & 2.6692e4 & 6.4494e4 & -1.2398e5 & -9.607e4 & -2.8533e5 \end{bmatrix}$$

b(:,11-20)=

$$\begin{bmatrix} 5.1763e5 & 1.6291e5 & -4.2026e3 & 1.3573e5 & 3.5928e5 & 5.0641e5 & 1.8815e5 & -2.9523e4 & 1.0784e5 & 1.6504e5 \\ -4.0993e5 & -1.0196e5 & -2.5468e3 & -7.2203e4 & -2.3888e5 & -3.3671e5 & -1.2293e5 & -2.2147e4 & -7.1704e4 & -9.797e4 \\ -4.1559e5 & -1.1694e3 & -198.8071 & 6.4209e3 & -1.0692e4 & -1.9868e5 & -6.5571e4 & -1.3966e3 & -2.2691e5 & -3.4875e4 \\ -7.1865e5 & -3.6071e5 & 2.6893e4 & -3.567e5 & -7.4876e5 & -1.112e6 & -4.0661e5 & 2.1448e5 & -4.3855e5 & -4.5765e5 \end{bmatrix}$$

b(:,21-30)=

$$\begin{bmatrix} 217.5912 & -853.4918 & 447.0109 & -311.2155 & -1.4341e3 & -765.9379 & -1.7956e9 & 1.1939e9 & -8.4941e7 & 1.8325e9 \\ -1.3515e3 & 431.6371 & -336.9502 & 296.5459 & 1.1025e3 & 481.6803 & 1.1939e9 & -1.1638e9 & 5.6477e7 & -1.2184e9 \\ -1.0979e3 & -655.0989 & -119.9638 & 288.6023 & 922.4949 & 263.1793 & -8.4941e7 & 5.6477e7 & -7.5716e8 & 8.6687e7 \\ 847.1166 & 1.5043e3 & 122.1378 & 173.5364 & 2.2317e3 & 2.2854e3 & 1.8325e9 & -1.2184e9 & 8.6687e7 & -3.8023e9 \end{bmatrix}$$

## C.2 "d" vector

d= h(1:10)=

$$\begin{bmatrix} 21.2556 & 22.5333 & 50.0881 & -20.1127 & -6.1366e7 \end{bmatrix}$$

## C.3 "h" vector

h(1:10)=

$$\begin{bmatrix} 22.9956 & -36.7379 & -49.4305 & 9.1522 & -161.3873 & -48.7929 & 13.1824 & -29.732 & -49.4305 & 9.1522 \end{bmatrix}$$

h(11:17)=

$$\begin{bmatrix} -60.3702 & 13.1824 & 22.9956 & -36.7379 & -48.7929 & -95.5216 & -1.2273e8 \end{bmatrix}$$

# Appendix D

# Mathematica

## D.1 Mathematica EOM

This section contains a Mathematica notebook that is used to generate the equations of motion of the beam. We start by importing the mode shapes and the Matlab calculations of strain integrals. It then creates a grid of points by varying two mode shapes and calculating the membrane stretch produced by the combination. A two dimensional surface is fit to this grid of points to establish a smooth approximation of the membrane stretch of these two mode shapes. This procedure is repeated for all combinations of mode shapes, and the results are combined to make a complete description of the strain in the beam as a function of the mode shapes. This is then used to calculate the potential energy as a function of the mode shapes, and combined with the kinetic energy to derive the equations of motion. The resulting coefficients are written to a file called MatLink.txt which is used by Matlab to run simulations of the beam model.

```
(*Clear any possible information in the kernel*)
ClearAll["Global`*"]
Remove["Global`*"]
(*import and interpolate the mode shapes*)
h0 = Import["C:\\Users\\louis\\Desktop\\abaM0.txt", "Table"];
m0 = Interpolation[h0];
h1 = Import["C:\\Users\\louis\\Desktop\\abaM1.txt", "Table"];
m1 = Interpolation[h1];
h2 = Import["C:\\Users\\louis\\Desktop\\abaM2.txt", "Table"];
m2 = Interpolation[h2];
h3 = Import["C:\\Users\\louis\\Desktop\\abaM3.txt", "Table"];
m3 = Interpolation[h3];

(*Import the matlab computed integrals*)
matFit = Import["C:\\Users\\louis\\Desktop\\matFit.txt", "Table"]

(*Import the beam end locations*)
u = Import["C:\\Users\\louis\\Desktop\\abaL.txt", "List"];
Ls = u[[1]]
Lb = u[[2]]
Lend = u[[3]]

(*Initialize some matrices for storing fit coefficients*)
(*The first row will be used to accumulate fit coefficients,
and the second row will
 be used to tally how many fits have been performed*)
```

$$b = \begin{pmatrix} 0 & 0 & 0 & 0 & 0 & 0 & 0 & 0 & 0 & 0 & 0 \\ 0 & 0 & 0 & 0 & 0 & 0 & 0 & 0 & 0 & 0 & 0 \end{pmatrix};$$

$$s = \begin{pmatrix} 0 & 0 & 0 & 0 & 0 & 0 & 0 & 0 & 0 & 0 & 0 \\ 0 & 0 & 0 & 0 & 0 & 0 & 0 & 0 & 0 & 0 & 0 \end{pmatrix};$$

$$\{\{-1.65753\times10^{-12}, 0.0000144173, 31.71, -2.99839\times10^{-11}, -3.17863\times10^{-11}, 9.28\times10^{-7}, 0.0448, -1.14\}, \{-9.93492\times10^{-12}, 0.0000224195, -30.41, -7.0656\times10^{-11}, 2.83717\times10^{-11}, 4.63996\times10^{-7}, 0.0149998, 7.526\times10^{-9}\}\}$$

0.105993

0.115992

0.221957

```
(*Calculate coeffecients for a0 and a1*)
```

$$\text{blahB} = \text{Table}\left[\text{Log}\left[\frac{1}{.116}\,\text{NIntegrate}\left[\sqrt{\left(1+(D[j\,m1[x]+i\,m0[x],x])^2\right)},\{x,0,Lb\}\right]\right],\{i,-2,2,.2\},\{j,-5,5,.5\}\right];$$

$$\text{blahS} = \text{Table}\left[\text{Log}\left[\frac{1}{.116}\,\text{NIntegrate}\left[\sqrt{\left(1+(D[j\,m1[x]+i\,m0[x],x])^2\right)},\{x,Ls,Lend\}\right]\right],\{i,-2,2,.2\},\{j,-5,5,.5\}\right];$$

```
blahB2 = Table[{i, j, blahB[[i 5 + 11, j 2 + 11]]}, {i, -2, 2, .2}, {j, -5, 5, .5}];
```

```
blahB3 = Table[{i , j , blahB[[i, j]]}, {i, 1, 21, 1}, {j, 1, 21, 1}];
blahS2 = Table[{i, j, blahS[[i 5 + 11, j 2 + 11]]}, {i, -2, 2, .2}, {j, -5, 5, .5}];
blahS3 = Table[{i , j , blahS[[i, j]]}, {i, 1, 21, 1}, {j, 1, 21, 1}];
doodB = Table[0, {i, 441}];
doodB2 = Table[0, {i, 441}];
doodS = Table[0, {i, 441}];
doodS2 = Table[0, {i, 441}];
For[i = 0, i < 21, i++, For[j = 1, j < 22, j++, doodB[[i * 21 + j]] = blahB2[[i + 1, j]]]]
For[i = 0, i < 21, i++, For[j = 1, j < 22, j++, doodB2[[i * 21 + j]] = blahB3[[i + 1, j]]]]
For[i = 0, i < 21, i++, For[j = 1, j < 22, j++, doodS[[i * 21 + j]] = blahS2[[i + 1, j]]]]
For[i = 0, i < 21, i++, For[j = 1, j < 22, j++, doodS2[[i * 21 + j]] = blahS3[[i + 1, j]]]]
planeB = Fit[doodB, {1, a1^2, a0^2, a1 a0}, {a0, a1}]
planeS = Fit[doodS, {1, a1^2, a0^2, a1 a0}, {a1, a0}]
b[[1, 2]] = b[[1, 2]] + Coefficient[planeB, a0^2];
b[[2, 2]] = b[[2, 2]] + 1;
b[[1, 3]] = b[[1, 3]] + Coefficient[planeB, a0 a1];
b[[2, 3]] = b[[2, 3]] + 1;
b[[1, 6]] = b[[1, 6]] + Coefficient[planeB, a1^2];
b[[2, 6]] = b[[2, 6]] + 1;
b[[1, 1]] = b[[1, 1]] + Chop[planeB - Coefficient[planeB, a0^2] a0^2 -
    Coefficient[planeB, a0 a1] a0 a1 - Coefficient[planeB, a1^2] a1^2];
b[[2, 1]] = b[[2, 1]] + 1;

s[[1, 3]] = s[[1, 3]] + Coefficient[planeS, a0 a1];
s[[2, 3]] = s[[2, 3]] + 1;
s[[1, 6]] = s[[1, 6]] + Coefficient[planeS, a1^2];
s[[2, 6]] = s[[2, 6]] + 1;


(*Calculate coeffecients for a0 and a2*)
blahB = Table[Log[1/.116 NIntegrate[√(1 + (D[j m2[x] + i m0[x], x])^2), {x, 0, Lb}]],
   {i, -2, 2, .2}, {j, -5, 5, .5}];
blahS = Table[Log[1/.116 NIntegrate[√(1 + (D[j m2[x] + i m0[x], x])^2), {x, Ls, Lend}]],
   {i, -2, 2, .2}, {j, -5, 5, .5}];
blahB2 = Table[{i, j, blahB[[i 5 + 11, j 2 + 11]]}, {i, -2, 2, .2}, {j, -5, 5, .5}];
blahB3 = Table[{i , j , blahB[[i, j]]}, {i, 1, 21, 1}, {j, 1, 21, 1}];
blahS2 = Table[{i, j, blahS[[i 5 + 11, j 2 + 11]]}, {i, -2, 2, .2}, {j, -5, 5, .5}];
blahS3 = Table[{i , j , blahS[[i, j]]}, {i, 1, 21, 1}, {j, 1, 21, 1}];
doodB = Table[0, {i, 441}];
doodB2 = Table[0, {i, 441}];
doodS = Table[0, {i, 441}];
doodS2 = Table[0, {i, 441}];
For[i = 0, i < 21, i++, For[j = 1, j < 22, j++, doodB[[i * 21 + j]] = blahB2[[i + 1, j]]]]
For[i = 0, i < 21, i++, For[j = 1, j < 22, j++, doodB2[[i * 21 + j]] = blahB3[[i + 1, j]]]]
For[i = 0, i < 21, i++, For[j = 1, j < 22, j++, doodS[[i * 21 + j]] = blahS2[[i + 1, j]]]]
```

```
For[i = 0, i < 21, i++, For[j = 1, j < 22, j++, doodS2[[i * 21 + j]] = blahS3[[i + 1, j]]]]
planeB = Fit[doodB, {1, a2^2, a0^2, a2 a0}, {a0, a2}]
planeS = Fit[doodS, {1, a2^2, a0^2, a2 a0}, {a0, a2}]
b[[1, 2]] = b[[1, 2]] + Coefficient[planeB, a0^2];
b[[2, 2]] = b[[2, 2]] + 1;
b[[1, 4]] = b[[1, 4]] + Coefficient[planeB, a0 a2];
b[[2, 4]] = b[[2, 4]] + 1;
b[[1, 7]] = b[[1, 7]] + Coefficient[planeB, a2^2];
b[[2, 7]] = b[[2, 7]] + 1;
b[[1, 1]] = b[[1, 1]] + Chop[planeB - Coefficient[planeB, a0^2] a0^2 -
    Coefficient[planeB, a0 a2] a0 a2 - Coefficient[planeB, a2^2] a2^2];
b[[2, 1]] = b[[2, 1]] + 1;

s[[1, 4]] = s[[1, 4]] + Coefficient[planeS, a0 a2];
s[[2, 4]] = s[[2, 4]] + 1;
s[[1, 7]] = s[[1, 7]] + Coefficient[planeS, a2^2];
s[[2, 7]] = s[[2, 7]] + 1;


(*Calculate coeffecients for a0 and a3*)
blahB = Table[Log[1/.116 NIntegrate[√(1 + (D[j m3[x] + i m0[x], x])^2), {x, 0, Lb}]],
   {i, -2, 2, .2}, {j, -5, 5, .5}];
blahS = Table[Log[1/.116 NIntegrate[√(1 + (D[j m3[x] + i m0[x], x])^2), {x, Ls, Lend}]],
   {i, -2, 2, .2}, {j, -5, 5, .5}];
blahB2 = Table[{i, j, blahB[[i 5 + 11, j 2 + 11]]}, {i, -2, 2, .2}, {j, -5, 5, .5}];
blahB3 = Table[{i , j , blahB[[i, j]]}, {i, 1, 21, 1}, {j, 1, 21, 1}];
blahS2 = Table[{i, j, blahS[[i 5 + 11, j 2 + 11]]}, {i, -2, 2, .2}, {j, -5, 5, .5}];
blahS3 = Table[{i , j , blahS[[i, j]]}, {i, 1, 21, 1}, {j, 1, 21, 1}];
doodB = Table[0, {i, 441}];
doodB2 = Table[0, {i, 441}];
doodS = Table[0, {i, 441}];
doodS2 = Table[0, {i, 441}];
For[i = 0, i < 21, i++, For[j = 1, j < 22, j++, doodB[[i * 21 + j]] = blahB2[[i + 1, j]]]]
For[i = 0, i < 21, i++, For[j = 1, j < 22, j++, doodB2[[i * 21 + j]] = blahB3[[i + 1, j]]]]
For[i = 0, i < 21, i++, For[j = 1, j < 22, j++, doodS[[i * 21 + j]] = blahS2[[i + 1, j]]]]
For[i = 0, i < 21, i++, For[j = 1, j < 22, j++, doodS2[[i * 21 + j]] = blahS3[[i + 1, j]]]]
planeB = Fit[doodB, {1, a3^2, a0^2, a3 a0}, {a0, a3}]
planeS = Fit[doodS, {1, a3^2, a0^2, a3 a0}, {a0, a3}]
b[[1, 2]] = b[[1, 2]] + Coefficient[planeB, a0^2];
b[[2, 2]] = b[[2, 2]] + 1;
b[[1, 5]] = b[[1, 5]] + Coefficient[planeB, a0 a3];
b[[2, 5]] = b[[2, 5]] + 1;
b[[1, 8]] = b[[1, 8]] + Coefficient[planeB, a3^2];
b[[2, 8]] = b[[2, 8]] + 1;
```

```
b[[1, 1]] = b[[1, 1]] + Chop[planeB - Coefficient[planeB, a0^2] a0^2 -
      Coefficient[planeB, a0 a3] a0 a3 - Coefficient[planeB, a3^2] a3^2];
b[[2, 1]] = b[[2, 1]] + 1;
Coefficient[planeS, a0^2]
s[[1, 2]] = s[[1, 2]] + Coefficient[planeS, a0^2];
s[[2, 2]] = s[[2, 2]] + 1;
s[[1, 5]] = s[[1, 5]] + Coefficient[planeS, a0 a3];
s[[2, 5]] = s[[2, 5]] + 1;
s[[1, 8]] = s[[1, 8]] + Coefficient[planeS, a3^2];
s[[2, 8]] = s[[2, 8]] + 1;
s[[1, 1]] = s[[1, 1]] + Chop[planeS - Coefficient[planeS, a0^2] a0^2 -
      Coefficient[planeS, a0 a3] a0 a3 - Coefficient[planeS, a3^2] a3^2];
s[[2, 1]] = s[[2, 1]] + 1;

(*Calculate coeffecients for a1 and a2*)
cross0B =
  Table[Log[1/.116 NIntegrate[√(1 + (D[j m1[x] + i m2[x] + m0[x], x])^2), {x, 0, Lb}]],
   {i, -5, 5, .5}, {j, -5, 5, .5}];
cross0S = Table[Log[1/.116 NIntegrate[√(1 + (D[j m1[x] + i m2[x] + m0[x], x])^2),
      {x, Ls, Lend}]], {i, -5, 5, .5}, {j, -5, 5, .5}];
cross0B2 = Table[{i, j, cross0B[[i 2 + 11, j 2 + 11]]}, {i, -5, 5, .5}, {j, -5, 5, .5}];
cross0B3 = Table[{i , j , cross0B[[i, j]]}, {i, 1, 21, 1}, {j, 1, 21, 1}];
cross0S2 = Table[{i, j, cross0S[[i 2 + 11, j 2 + 11]]}, {i, -5, 5, .5}, {j, -5, 5, .5}];
cross0S3 = Table[{i , j , cross0S[[i, j]]}, {i, 1, 21, 1}, {j, 1, 21, 1}];
cdood0B = Table[0, {i, 441}];
cdood0B2 = Table[0, {i, 441}];
cdood0S = Table[0, {i, 441}];
cdood0S2 = Table[0, {i, 441}];
For[i = 0, i < 21, i++,
 For[j = 1, j < 22, j++, cdood0B[[i * 21 + j]] = cross0B2[[i + 1, j]]]]
For[i = 0, i < 21, i++, For[j = 1, j < 22, j++,
  cdood0B2[[i * 21 + j]] = cross0B3[[i + 1, j]]]]
For[i = 0, i < 21, i++, For[j = 1, j < 22, j++,
  cdood0S[[i * 21 + j]] = cross0S2[[i + 1, j]]]]
For[i = 0, i < 21, i++, For[j = 1, j < 22, j++,
  cdood0S2[[i * 21 + j]] = cross0S3[[i + 1, j]]]]
plane0B = Fit[cdood0B, {1, a1, a2, a1^2, a2^2, a1 a2}, {a2, a1}]
plane0S = Fit[cdood0S, {1, a1, a2, a1^2, a2^2, a1 a2}, {a2, a1}]
b[[1, 7]] = b[[1, 7]] + Coefficient[plane0B, a2^2];
b[[2, 7]] = b[[2, 7]] + 1;
b[[1, 9]] = b[[1, 9]] + Coefficient[plane0B, a2 a1];
b[[2, 9]] = b[[2, 9]] + 1;
b[[1, 6]] = b[[1, 6]] + Coefficient[plane0B, a1^2];
b[[2, 6]] = b[[2, 6]] + 1;
```

```
b[[1, 3]] = b[[1, 3]] + Coefficient[plane0B, a1] /. a2 → 0;
b[[2, 3]] = b[[2, 3]] + 1;
b[[1, 4]] = b[[1, 4]] + Coefficient[plane0B, a2] /. a1 → 0;
b[[2, 4]] = b[[2, 4]] + 1;
s[[1, 7]] = s[[1, 7]] + Coefficient[plane0S, a2^2];
s[[2, 7]] = s[[2, 7]] + 1;
s[[1, 9]] = s[[1, 9]] + Coefficient[plane0S, a2 a1];
s[[2, 9]] = s[[2, 9]] + 1;
s[[1, 6]] = s[[1, 6]] + Coefficient[plane0S, a1^2];
s[[2, 6]] = s[[2, 6]] + 1;
s[[1, 3]] = s[[1, 3]] + Coefficient[plane0S, a1] /. a2 → 0;
s[[2, 3]] = s[[2, 3]] + 1;
s[[1, 4]] = s[[1, 4]] + Coefficient[plane0S, a2] /. a1 → 0;
s[[2, 4]] = s[[2, 4]] + 1;

(*Calculate coeffecients for a1 and a3*)
cross0B =
  Table[Log[1/.116 NIntegrate[√(1 + (D[j m1[x] + i m3[x] + m0[x], x])^2), {x, 0, Lb}]],
   {i, -5, 5, .5}, {j, -5, 5, .5}];
cross0S = Table[Log[1/.116 NIntegrate[√(1 + (D[j m1[x] + i m3[x] + m0[x], x])^2),
      {x, Ls, Lend}]], {i, -5, 5, .5}, {j, -5, 5, .5}];
cross0B2 = Table[{i, j, cross0B[[i 2 + 11, j 2 + 11]]}, {i, -5, 5, .5}, {j, -5, 5, .5}];
cross0B3 = Table[{i , j , cross0B[[i, j]]}, {i, 1, 21, 1}, {j, 1, 21, 1}];
cross0S2 = Table[{i, j, cross0S[[i 2 + 11, j 2 + 11]]}, {i, -5, 5, .5}, {j, -5, 5, .5}];
cross0S3 = Table[{i , j , cross0S[[i, j]]}, {i, 1, 21, 1}, {j, 1, 21, 1}];
cdood0B = Table[0, {i, 441}];
cdood0B2 = Table[0, {i, 441}];
cdood0S = Table[0, {i, 441}];
cdood0S2 = Table[0, {i, 441}];
For[i = 0, i < 21, i++,
 For[j = 1, j < 22, j++, cdood0B[[i * 21 + j]] = cross0B2[[i + 1, j]]]]
For[i = 0, i < 21, i++, For[j = 1, j < 22, j++,
  cdood0B2[[i * 21 + j]] = cross0B3[[i + 1, j]]]]
For[i = 0, i < 21, i++, For[j = 1, j < 22, j++,
  cdood0S[[i * 21 + j]] = cross0S2[[i + 1, j]]]]
For[i = 0, i < 21, i++, For[j = 1, j < 22, j++,
  cdood0S2[[i * 21 + j]] = cross0S3[[i + 1, j]]]]
plane0B = Fit[cdood0B, {1, a1, a3, a1^2, a3^2, a1 a3}, {a3, a1}]
plane0S = Fit[cdood0S, {1, a1, a3, a1^2, a3^2, a1 a3}, {a3, a1}]
b[[1, 8]] = b[[1, 8]] + Coefficient[plane0B, a3^2];
b[[2, 8]] = b[[2, 8]] + 1;
b[[1, 10]] = b[[1, 10]] + Coefficient[plane0B, a3 a1];
b[[2, 10]] = b[[2, 10]] + 1;
b[[1, 6]] = b[[1, 6]] + Coefficient[plane0B, a1^2];
b[[2, 6]] = b[[2, 6]] + 1;
```

```
b[[1, 3]] = b[[1, 3]] + Coefficient[plane0B, a1] /. a3 → 0;
b[[2, 3]] = b[[2, 3]] + 1;
b[[1, 5]] = b[[1, 5]] + Coefficient[plane0B, a3] /. a1 → 0;
b[[2, 5]] = b[[2, 5]] + 1;
s[[1, 8]] = s[[1, 8]] + Coefficient[plane0S, a3^2];
s[[2, 8]] = s[[2, 8]] + 1;
s[[1, 10]] = s[[1, 10]] + Coefficient[plane0S, a3 a1];
s[[2, 10]] = s[[2, 10]] + 1;
s[[1, 6]] = s[[1, 6]] + Coefficient[plane0S, a1^2];
s[[2, 6]] = s[[2, 6]] + 1;
s[[1, 3]] = s[[1, 3]] + Coefficient[plane0S, a1] /. a3 → 0;
s[[2, 3]] = s[[2, 3]] + 1;
s[[1, 5]] = s[[1, 5]] + Coefficient[plane0S, a3] /. a1 → 0;
s[[2, 5]] = s[[2, 5]] + 1;

(*Calculate coeffecients for a2 and a3*)
cross0B =
  Table[Log[1/.116 NIntegrate[√(1 + (D[j m3[x] + i m2[x] + m0[x], x])^2), {x, 0, Lb}]],
   {i, -5, 5, .5}, {j, -5, 5, .5}];
cross0S = Table[Log[1/.116 NIntegrate[√(1 + (D[j m3[x] + i m2[x] + m0[x], x])^2),
      {x, Ls, Lend}]], {i, -5, 5, .5}, {j, -5, 5, .5}];
cross0B2 = Table[{i, j, cross0B[[i 2 + 11, j 2 + 11]]}, {i, -5, 5, .5}, {j, -5, 5, .5}];
cross0B3 = Table[{i , j , cross0B[[i, j]]}, {i, 1, 21, 1}, {j, 1, 21, 1}];
cross0S2 = Table[{i, j, cross0S[[i 2 + 11, j 2 + 11]]}, {i, -5, 5, .5}, {j, -5, 5, .5}];
cross0S3 = Table[{i , j , cross0S[[i, j]]}, {i, 1, 21, 1}, {j, 1, 21, 1}];
cdood0B = Table[0, {i, 441}];
cdood0B2 = Table[0, {i, 441}];
cdood0S = Table[0, {i, 441}];
cdood0S2 = Table[0, {i, 441}];
For[i = 0, i < 21, i++,
 For[j = 1, j < 22, j++, cdood0B[[i * 21 + j]] = cross0B2[[i + 1, j]]]]
For[i = 0, i < 21, i++, For[j = 1, j < 22, j++,
  cdood0B2[[i * 21 + j]] = cross0B3[[i + 1, j]]]]
For[i = 0, i < 21, i++, For[j = 1, j < 22, j++,
  cdood0S[[i * 21 + j]] = cross0S2[[i + 1, j]]]]
For[i = 0, i < 21, i++, For[j = 1, j < 22, j++,
  cdood0S2[[i * 21 + j]] = cross0S3[[i + 1, j]]]]
plane0B = Fit[cdood0B, {1, a3, a2, a3^2, a2^2, a3 a2}, {a2, a3}]
plane0S = Fit[cdood0S, {1, a3, a2, a3^2, a2^2, a3 a2}, {a2, a3}]
b[[1, 7]] = b[[1, 7]] + Coefficient[plane0B, a2^2];
b[[2, 7]] = b[[2, 7]] + 1;
b[[1, 11]] = b[[1, 11]] + Coefficient[plane0B, a2 a3];
b[[2, 11]] = b[[2, 11]] + 1;
b[[1, 8]] = b[[1, 8]] + Coefficient[plane0B, a3^2];
b[[2, 8]] = b[[2, 8]] + 1;
```

```
b[[1, 5]] = b[[1, 5]] + Coefficient[plane0B, a3] /. a2 → 0;
b[[2, 5]] = b[[2, 5]] + 1;
b[[1, 4]] = b[[1, 4]] + Coefficient[plane0B, a2] /. a3 → 0;
b[[2, 4]] = b[[2, 4]] + 1;
s[[1, 7]] = s[[1, 7]] + Coefficient[plane0S, a2^2];
s[[2, 7]] = s[[2, 7]] + 1;
s[[1, 11]] = s[[1, 11]] + Coefficient[plane0S, a2 a3];
s[[2, 11]] = s[[2, 11]] + 1;
s[[1, 8]] = s[[1, 8]] + Coefficient[plane0S, a3^2];
s[[2, 8]] = s[[2, 8]] + 1;
s[[1, 5]] = s[[1, 5]] + Coefficient[plane0S, a3] /. a2 → 0;
s[[2, 5]] = s[[2, 5]] + 1;
s[[1, 4]] = s[[1, 4]] + Coefficient[plane0S, a2] /. a3 → 0;
s[[2, 4]] = s[[2, 4]] + 1;


(*Perform averaging to make a "best guess" at the true coefficients*)
st =
 ( s[[1,1]]/s[[2,1]]  s[[1,2]]/s[[2,2]]  s[[1,3]]/s[[2,3]]  s[[1,4]]/s[[2,4]]  s[[1,5]]/s[[2,5]]  s[[1,6]]/s[[2,6]]  s[[1,7]]/s[[2,7]]  s[[1,8]]/s[[2,8]]  s[[1,9]]/s[[2,9]]  s[[1,10]]/s[[2,10]]  s[[1,
  )
bt = ( b[[1,1]]/b[[2,1]]  b[[1,2]]/b[[2,2]]  b[[1,3]]/b[[2,3]]  b[[1,4]]/b[[2,4]]  b[[1,5]]/b[[2,5]]  b[[1,6]]/b[[2,6]]  b[[1,7]]/b[[2,7]]  b[[1,8]]/b[[2,8]]  b[[1,9]]/b[[2,9]]  b[[1,10]]/b[[2,10]]  b
(*Assemble the coefficients into equations
 for the strain in either section of the beam*)
pSb[t_] = st[[1, 1]] + st[[1, 2]] a0[t]^2 + st[[1, 3]] a0[t] a1[t] + st[[1, 4]] a0[t] a2[t] +
   st[[1, 5]] a0[t] a3[t] + st[[1, 6]] a1[t]^2 + st[[1, 7]] a2[t]^2 + st[[1, 8]] a3[t]^2 +
   st[[1, 9]] a1[t] a2[t] + st[[1, 10]] a1[t] a3[t] + st[[1, 11]] a2[t] a3[t];
pBb[t_] = bt[[1, 1]] + bt[[1, 2]] a0[t]^2 + bt[[1, 3]] a0[t] a1[t] + bt[[1, 4]] a0[t] a2[t] +
   bt[[1, 5]] a0[t] a3[t] + bt[[1, 6]] a1[t]^2 + bt[[1, 7]] a2[t]^2 + bt[[1, 8]] a3[t]^2 +
   bt[[1, 9]] a1[t] a2[t] + bt[[1, 10]] a1[t] a3[t] + bt[[1, 11]] a2[t] a3[t];
(*Calculate the constant needed to provide the correct equilibrium strain*)
Vb = matFit[[1, 1]] / (pBb[t] /. {a0[t] → 1, a1[t] → 0, a2[t] → 0, a3[t] → 0});
Vs = matFit[[2, 1]] / (pSb[t] /. {a0[t] → 1, a1[t] → 0, a2[t] → 0, a3[t] → 0});
(*Calculate the constant needed to
 provide the correct strain energy at equilibrium*)
Yb = matFit[[1, 2]] / (Expand[pBb[t]^2] /. {a0[t] → 1, a1[t] → 0, a2[t] → 0, a3[t] → 0});
Ys = matFit[[2, 2]] / (Expand[pSb[t]^2] /. {a0[t] → 1, a1[t] → 0, a2[t] → 0, a3[t] → 0});

(*Use the calculated constants to build
 functions of true strain and strain energy*)
ϵB[t] = Expand[Vb pBb[t]]
ϵS[t] = Expand[Vs pSb[t]]
seB[t] = Expand[Yb pBb[t]^2]
seS[t] = Expand[Ys pSb[t]^2]
```

$-0.0000679281 + 0.0000185347\, a0^2 + 0.0000525187\, a0\, a1 + 0.0000389681\, a1^2$

$$-0.000309293 + 0.000104647\, a0^2 - 0.0000928824\, a0\, a1 + 0.000211663\, a1^2$$

$$-0.0000674142 + 0.0000184938\, a0^2 + 0.0000462292\, a0\, a2 + 0.0000763954\, a2^2$$

$$-0.000278343 + 0.00020877\, a0^2 - 0.000158893\, a0\, a2 + 0.000559431\, a2^2$$

$$-0.0000680715 + 0.0000185663\, a0^2 - 0.0000223791\, a0\, a3 + 0.0000108986\, a3^2$$

$$-0.000297077 + 0.000210046\, a0^2 + 0.000255112\, a0\, a3 + 0.000332653\, a3^2$$

$$0.000210046$$

$$-0.0000476099 + 0.0000523102\, a1 + 0.0000388347\, a1^2 + 0.0000461181\, a2 + 0.0000478771\, a1\, a2 + 0.0000762643\, a2^2$$

$$-0.0000395199 - 0.0000907213\, a1 + 0.000101279\, a1^2 - 0.000158242\, a2 + 0.000339437\, a1\, a2 + 0.00055627\, a2^2$$

$$-0.0000491967 + 0.0000524875\, a1 + 0.0000389481\, a1^2 - 0.000022325\, a3 - 0.0000265292\, a1\, a3 + 0.000010877\, a3^2$$

$$-0.0000741582 - 0.0000914474\, a1 + 0.000103277\, a1^2 + 0.000254258\, a3 - 0.0000629999\, a1\, a3 + 0.000331376\, a3^2$$

$$-0.0000483036 + 0.0000461762\, a2 + 0.0000763295\, a2^2 - 0.0000222373\, a3 - 0.0000558074\, a2\, a3 + 0.0000108289\, a3^2$$

$$-5.4275 \times 10^{-6} - 0.000160968\, a2 + 0.000553581\, a2^2 + 0.000252572\, a3 + 0.000331085\, a2\, a3 + 0.0003267\, a3^2$$

```
{{-0.000297077, 0.000210046, -0.0000916837, -0.000159368, 0.000253981, 0.00013874,
  0.000556427, 0.000330243, 0.000339437, -0.0000629999, 0.000331085}}
```

```
{{-0.0000678046, 0.0000185316, 0.0000524388,
  0.0000461745, -0.0000223138, 0.0000389169, 0.0000763297,
  0.0000108682, 0.0000478771, -0.0000265292, -0.0000558074}}
```

$$-2.28092 \times 10^{-12} + 6.23396 \times 10^{-13}\, a0[t]^2 + 1.76402 \times 10^{-12}\, a0[t]\, a1[t] + 1.30915 \times 10^{-12}\, a1[t]^2 + 1.55329 \times 10^{-12}\, a0[t]\, a2[t] + 1.61057 \times 10^{-12}\, a1[t]\, a2[t] + 2.56771 \times 10^{-12}\, a2[t]^2 - 7.50628 \times 10^{-13}\, a0[t]\, a3[t] - 8.92432 \times 10^{-13}\, a1[t]\, a3[t] - 1.87734 \times 10^{-12}\, a2[t]\, a3[t] + 3.65601 \times 10^{-13}\, a3[t]^2$$

$$-3.39125 \times 10^{-11} + 2.39776 \times 10^{-11}\, a0[t]^2 - 1.04661 \times 10^{-11}\, a0[t]\, a1[t] + 1.58377 \times 10^{-11}\, a1[t]^2 - 1.81925 \times 10^{-11}\, a0[t]\, a2[t] + 3.87481 \times 10^{-11}\, a1[t]\, a2[t] + 6.35184 \times 10^{-11}\, a2[t]^2 + 2.89929 \times 10^{-11}\, a0[t]\, a3[t] - 7.1917 \times 10^{-12}\, a1[t]\, a3[t] + 3.77947 \times 10^{-11}\, a2[t]\, a3[t] + 3.76986 \times 10^{-11}\, a3[t]^2$$

$$0.0000273013 - 0.0000149233\, a0[t]^2 + 2.03934\times10^{-6}\, a0[t]^4 - 0.0000422285\, a0[t]\, a1[t] + 0.0000115414\, a0[t]^3\, a1[t] - 0.0000313395\, a1[t]^2 + 0.0000248947\, a0[t]^2\, a1[t]^2 + 0.0000242374\, a0[t]\, a1[t]^3 + 8.99376\times10^{-6}\, a1[t]^4 - 0.0000371839\, a0[t]\, a2[t] + 0.0000101627\, a0[t]^3\, a2[t] - 0.000038555\, a1[t]\, a2[t] + 0.0000392948\, a0[t]^2\, a1[t]\, a2[t] + 0.0000511597\, a0[t]\, a1[t]^2\, a2[t] + 0.0000221289\, a1[t]^3\, a2[t] - 0.0000614677\, a2[t]^2 + 0.0000294607\, a0[t]^2\, a2[t]^2 + 0.0000737937\, a0[t]\, a1[t]\, a2[t]^2 + 0.0000488917\, a1[t]^2\, a2[t]^2 + 0.0000418591\, a0[t]\, a2[t]^3 + 0.0000434026\, a1[t]\, a2[t]^3 + 0.000034598\, a2[t]^4 + 0.0000179691\, a0[t]\, a3[t] - 4.91112\times10^{-6}\, a0[t]^3\, a3[t] + 0.0000213637\, a1[t]\, a3[t] - 0.0000197359\, a0[t]^2\, a1[t]\, a3[t] - 0.0000268358\, a0[t]\, a1[t]^2\, a3[t] - 0.0000122619\, a1[t]^3\, a3[t] + 0.0000449413\, a2[t]\, a3[t] - 0.0000245197\, a0[t]^2\, a2[t]\, a3[t] - 0.0000619933\, a0[t]\, a1[t]\, a2[t]\, a3[t] - 0.0000408794\, a1[t]^2\, a2[t]\, a3[t] - 0.0000508331\, a0[t]\, a2[t]^2\, a3[t] - 0.000055783\, a1[t]\, a2[t]^2\, a3[t] - 0.0000505918\, a2[t]^3\, a3[t] - 8.75204\times10^{-6}\, a3[t]^2 + 5.34873\times10^{-6}\, a0[t]^2\, a3[t]^2 + 0.0000137992\, a0[t]\, a1[t]\, a3[t]^2 + 9.20267\times10^{-6}\, a1[t]^2\, a3[t]^2 + 0.0000207498\, a0[t]\, a2[t]\, a3[t]^2 + 0.0000237635\, a1[t]\, a2[t]\, a3[t]^2 + 0.0000283472\, a2[t]^2\, a3[t]^2 - 2.8802\times10^{-6}\, a0[t]\, a3[t]^3 - 3.42431\times10^{-6}\, a1[t]\, a3[t]^3 - 7.20347\times10^{-6}\, a2[t]\, a3[t]^3 + 7.01416\times10^{-7}\, a3[t]^4$$

$$0.000261227 - 0.000369397\, a0[t]^2 + 0.00013059\, a0[t]^4 + 0.000161239\, a0[t]\, a1[t] - 0.000114003\, a0[t]^3\, a1[t] - 0.000243994\, a1[t]^2 + 0.000197395\, a0[t]^2\, a1[t]^2 - 0.0000753012\, a0[t]\, a1[t]^3 + 0.0000569745\, a1[t]^4 + 0.000280271\, a0[t]\, a2[t] - 0.000198164\, a0[t]^3\, a2[t] - 0.000596949\, a1[t]\, a2[t] + 0.000508566\, a0[t]^2\, a1[t]\, a2[t] - 0.000315121\, a0[t]\, a1[t]^2\, a2[t] + 0.000278785\, a1[t]^3\, a2[t] - 0.000978558\, a2[t]^2 + 0.000767059\, a0[t]^2\, a2[t]^2 - 0.000622237\, a0[t]\, a1[t]\, a2[t]^2 + 0.000798036\, a1[t]^2\, a2[t]^2 - 0.00052495\, a0[t]\, a2[t]^3 + 0.00111809\, a1[t]\, a2[t]^3 + 0.000916423\, a2[t]^4 - 0.000446662\, a0[t]\, a3[t] + 0.000315809\, a0[t]^3\, a3[t] + 0.000110795\, a1[t]\, a3[t] - 0.000216185\, a0[t]^2\, a1[t]\, a3[t] + 0.000242792\, a0[t]\, a1[t]^2\, a3[t] - 0.0000517428\, a1[t]^3\, a3[t] - 0.000582261\, a2[t]\, a3[t] + 0.000172071\, a0[t]^2\, a2[t]\, a3[t] + 0.000390091\, a0[t]\, a1[t]\, a2[t]\, a3[t] + 0.000145333\, a1[t]^2\, a2[t]\, a3[t] + 0.000524246\, a0[t]\, a2[t]^2\, a3[t] + 0.000457767\, a1[t]\, a2[t]^2\, a3[t] + 0.00109058\, a2[t]^3\, a3[t] - 0.000580781\, a3[t]^2 + 0.00060157\, a0[t]^2\, a3[t]^2 - 0.000273962\, a0[t]\, a1[t]\, a3[t]^2 + 0.000282982\, a1[t]^2\, a3[t]^2 + 0.000186233\, a0[t]\, a2[t]\, a3[t]^2 + 0.000540116\, a1[t]\, a2[t]\, a3[t]^2 + 0.00141226\, a2[t]^2\, a3[t]^2 + 0.000496528\, a0[t]\, a3[t]^3 - 0.000123164\, a1[t]\, a3[t]^3 + 0.000647266\, a2[t]\, a3[t]^3 + 0.00032281\, a3[t]^4$$

```
(*Define the electric field as the voltage divided by the thickness*)
Eb[t_] = vL'[t] / (2 hp);
Es[t_] = vR'[t] / (hp);
(*Define the thickness of the piezo element*)
hp = 0.0004;

mS = matFit[[1, 7]]; (*mass/length steel*)
mP = matFit[[2, 7]]; (*mass/length piezo*)
ϵ = matFit[[2, 8]];  (*dielectric constant*)
d31 = matFit[[1, 8]]; (*piezoelectric coupling constant*)

y[t_] = A Sin[ω t]; (*base excitation of amplitude 'A' and frequency 'ω'*)

(*construct the potential energy function*)
Pe[t_] = seB[t] + seS[t] - (matFit[[1, 3]] + matFit[[2, 3]] a0[t]^2) (ϵB[t] + ϵS[t]) -
   d31 (Eb[t] (matFit[[1, 4]] a0[t] + matFit[[1, 5]] a1[t] +
         matFit[[2, 4]] a2[t] + matFit[[2, 5]] a3[t]) + Es[t] ϵS[t]) -
   ϵ/2 (matFit[[1, 6]] Eb[t]^2 + matFit[[2, 6]] Es[t]^2) // Simplify
```

$$
\begin{aligned}
&0.000288529 + 0.00013263\, a0[t]^4 + 0.0000659683\, a1[t]^4 - 0.00104003\, a2[t]^2 + \\
&0.000951021\, a2[t]^4 + a1[t]^3\, (0.000300914\, a2[t] - 0.0000640047\, a3[t]) + \\
&a0[t]^3\, (-0.000102462\, a1[t] - 0.000188002\, a2[t] + 0.000310899\, a3[t]) - \\
&0.000537321\, a2[t]\, a3[t] + 0.00103999\, a2[t]^3\, a3[t] - 0.000589534\, a3[t]^2 + \\
&0.00144061\, a2[t]^2\, a3[t]^2 + 0.000640063\, a2[t]\, a3[t]^3 + 0.000323512\, a3[t]^4 - \\
&1.00685 \times 10^{-7}\, a2[t]\, vL'[t] + 4.04297 \times 10^{-8}\, a3[t]\, vL'[t] - 1.09127 \times 10^{-8}\, vL'[t]^2 + \\
&a1[t]\, \big(0.00116149\, a2[t]^3 + 0.000401984\, a2[t]^2\, a3[t] - 0.000126588\, a3[t]^3 - \\
&\quad 4.52955 \times 10^{-8}\, vL'[t] + a3[t]\, (0.000132159 - 2.04963 \times 10^{-8}\, vR'[t]) + \\
&\quad a2[t]\, (-0.000635506 + 0.00056388\, a3[t]^2 + 1.10432 \times 10^{-7}\, vR'[t])\big) + \\
&a1[t]^2\, \big(-0.000275334 + 0.000846928\, a2[t]^2 + 0.000104453\, a2[t]\, a3[t] + \\
&\quad 0.000292184\, a3[t]^2 + 4.51374 \times 10^{-8}\, vR'[t]\big) + \\
&a0[t]^2\, \big(-0.000384322 + 0.00022229\, a1[t]^2 + 0.000796521\, a2[t]^2 + \\
&\quad a1[t]\, (0.000547862\, a2[t] - 0.000235921\, a3[t]) + 0.000147552\, a2[t]\, a3[t] + \\
&\quad 0.00060692\, a3[t]^2 + 6.83362 \times 10^{-8}\, vR'[t]\big) - 9.66507 \times 10^{-8}\, vR'[t] + \\
&1.81027 \times 10^{-7}\, a2[t]^2\, vR'[t] + 1.07715 \times 10^{-7}\, a2[t]\, a3[t]\, vR'[t] + \\
&1.07441 \times 10^{-7}\, a3[t]^2\, vR'[t] - 2.18252 \times 10^{-8}\, vR'[t]^2 + \\
&a0[t]\, \big(-0.0000510639\, a1[t]^3 - 0.000483091\, a2[t]^3 + \\
&\quad a1[t]^2\, (-0.000263962\, a2[t] + 0.000215956\, a3[t]) - 0.000428694\, a3[t] + \\
&\quad 0.000473413\, a2[t]^2\, a3[t] + 0.000493648\, a3[t]^3 - 4.27271 \times 10^{-8}\, vL'[t] + \\
&\quad a2[t]\, (0.000243088 + 0.000206983\, a3[t]^2 - 5.18485 \times 10^{-8}\, vR'[t]) + \\
&\quad a1[t]\, \big(0.000119011 - 0.000548443\, a2[t]^2 + 0.000328097\, a2[t]\, a3[t] - \\
&\qquad 0.000260163\, a3[t]^2 - 2.98283 \times 10^{-8}\, vR'[t]\big) + 8.26299 \times 10^{-8}\, a3[t]\, vR'[t]\big)
\end{aligned}
$$

```
Te[t_] =
 mS / 2 (a0'[t]^2 NIntegrate[m0[x]^2, {x, 0, Lb}] + 2 y'[t] a0'[t] NIntegrate[m0[x],
        {x, 0, Lb}] + y'[t]^2 + 2 a0'[t] a1'[t] NIntegrate[m0[x] m1[x], {x, 0, Lb}] +
      2 a0'[t] a2'[t] NIntegrate[m0[x] m2[x], {x, 0, Lb}] + 2 a0'[t] a3'[t]
       NIntegrate[m0[x] m3[x], {x, 0, Lb}] + a1'[t]^2 NIntegrate[m1[x]^2, {x, 0, Lb}] +
      a2'[t]^2 NIntegrate[m2[x]^2, {x, 0, Lb}] + a3'[t]^2 NIntegrate[m3[x]^2, {x, 0, Lb}] +
      2 y'[t] a1'[t] NIntegrate[m1[x], {x, 0, Lb}] + 2 y'[t] a2'[t]
       NIntegrate[m2[x], {x, 0, Lb}] + 2 y'[t] a3'[t] NIntegrate[m3[x], {x, 0, Lb}]) +
   mP (a0'[t]^2 NIntegrate[m0[x]^2, {x, 0, Lb}] + 2 y'[t] a0'[t] NIntegrate[m0[x],
        {x, 0, Lb}] + y'[t]^2 + 2 a0'[t] a1'[t] NIntegrate[m0[x] m1[x], {x, 0, Lb}] +
      2 a0'[t] a2'[t] NIntegrate[m0[x] m2[x], {x, 0, Lb}] + 2 a0'[t] a3'[t]
       NIntegrate[m0[x] m3[x], {x, 0, Lb}] + a1'[t]^2 NIntegrate[m1[x]^2, {x, 0, Lb}] +
      a2'[t]^2 NIntegrate[m2[x]^2, {x, 0, Lb}] + a3'[t]^2 NIntegrate[m3[x]^2, {x, 0, Lb}] +
      2 y'[t] a1'[t] NIntegrate[m1[x], {x, 0, Lb}] + 2 y'[t] a2'[t]
       NIntegrate[m2[x], {x, 0, Lb}] + 2 y'[t] a3'[t] NIntegrate[m3[x], {x, 0, Lb}]) +
   mP / 2 (a0'[t]^2 NIntegrate[m0[x]^2, {x, Ls, Lend}] +
      2 y'[t] a0'[t] NIntegrate[m0[x], {x, Ls, Lend}] + y'[t]^2 +
      2 a0'[t] a1'[t] NIntegrate[m0[x] m1[x], {x, Ls, Lend}] +
      2 a0'[t] a2'[t] NIntegrate[m0[x] m2[x], {x, Ls, Lend}] +
      2 a0'[t] a3'[t] NIntegrate[m0[x] m3[x], {x, Ls, Lend}] +
      a1'[t]^2 NIntegrate[m1[x]^2, {x, Ls, Lend}] + a2'[t]^2
       NIntegrate[m2[x]^2, {x, Ls, Lend}] + a3'[t]^2 NIntegrate[m3[x]^2, {x, Ls, Lend}] +
      2 y'[t] a1'[t] NIntegrate[m1[x], {x, Ls, Lend}] +
      2 y'[t] a2'[t] NIntegrate[m2[x], {x, Ls, Lend}] +
      2 y'[t] a3'[t] NIntegrate[m3[x], {x, Ls, Lend}]) // Simplify
```

$$0.0448997\, A^2 \omega^2 \mathrm{Cos}[t\,\omega]^2 + 1.14697\times 10^{-9}\, a0'[t]^2 + 4.04419\times 10^{-6}\, A\,\omega\, \mathrm{Cos}[t\,\omega]\, a1'[t] + 1.35153\times 10^{-9}\, a1'[t]^2 - 1.47141\times 10^{-6}\, A\,\omega\, \mathrm{Cos}[t\,\omega]\, a2'[t] + 6.63889\times 10^{-10}\, a2'[t]^2 + a0'[t]\left(3.4445\times 10^{-6}\, A\,\omega\, \mathrm{Cos}[t\,\omega] + 1.79724\times 10^{-9}\, a1'[t] - 6.28138\times 10^{-11}\, a2'[t] + 5.28213\times 10^{-10}\, a3'[t]\right) + 5.5338\times 10^{-7}\, A\,\omega\, \mathrm{Cos}[t\,\omega]\, a3'[t] + 2.58787\times 10^{-10}\, a3'[t]^2$$

```
Needs["VariationalMethods`"]
VV1 = EulerEquations[Te[t] - Pe[t],
   {a0[t], a1[t], a2[t], a3[t], vR[t], vL[t]}, t] // Expand
```

$$\{0.000768644\, a0[t] - 0.000530519\, a0[t]^3 - 0.000119011\, a1[t] + 0.000307385\, a0[t]^2\, a1[t] - 0.00044458\, a0[t]\, a1[t]^2 + 0.0000510639\, a1[t]^3 - 0.000243088\, a2[t] + 0.000564005\, a0[t]^2\, a2[t] - 0.00109572\, a0[t]\, a1[t]\, a2[t] + 0.000263962\, a1[t]^2\, a2[t] - 0.00159304\, a0[t]\, a2[t]^2 + 0.000548443\, a1[t]\, a2[t]^2 + 0.000483091\, a2[t]^3 + 0.000428694\, a3[t] - 0.000932697\, a0[t]^2\, a3[t] + 0.000471842\, a0[t]\, a1[t]\, a3[t] - 0.000215956\, a1[t]^2\, a3[t] - 0.000295104\, a0[t]\, a2[t]\, a3[t] - 0.000328097\, a1[t]\, a2[t]\, a3[t] - 0.000473413\, a2[t]^2\, a3[t] - 0.00121384\, a0[t]\, a3[t]^2 + 0.000260163\, a1[t]\, a3[t]^2 - 0.000206983\, a2[t]\, a3[t]^2 - 0.000493648\, a3[t]^3 + 3.4445\times 10^{-6}\, A\,\omega^2\, \mathrm{Sin}[t\,\omega] + 4.27271\times 10^{-8}\, vL'[t] - 1.36672\times 10^{-7}\, a0[t]\, vR'[t] + 2.98283\times 10^{-8}\, a1[t]\, vR'[t] + 5.18485\times 10^{-8}\, a2[t]\, vR'[t] - 8.26299\times 10^{-8}\, a3[t]\, vR'[t] - 2.29394\times 10^{-9}\, a0''[t] - 1.79724\times 10^{-9}\, a1''[t] + 6.28138\times 10^{-11}\, a2''[t] - 5.28213\times 10^{-10}\, a3''[t] == 0,$$

$$
\begin{aligned}
&-0.000119011\, a0[t] + 0.000102462\, a0[t]^3 + 0.000550668\, a1[t] - 0.00044458\, a0[t]^2\, a1[t] + \\
&\quad 0.000153192\, a0[t]\, a1[t]^2 - 0.000263873\, a1[t]^3 + 0.000635506\, a2[t] - \\
&\quad 0.000547862\, a0[t]^2\, a2[t] + 0.000527923\, a0[t]\, a1[t]\, a2[t] - 0.000902742\, a1[t]^2\, a2[t] + \\
&\quad 0.000548443\, a0[t]\, a2[t]^2 - 0.00169386\, a1[t]\, a2[t]^2 - 0.00116149\, a2[t]^3 - \\
&\quad 0.000132159\, a3[t] + 0.000235921\, a0[t]^2\, a3[t] - 0.000431912\, a0[t]\, a1[t]\, a3[t] + \\
&\quad 0.000192014\, a1[t]^2\, a3[t] - 0.000328097\, a0[t]\, a2[t]\, a3[t] - \\
&\quad 0.000208907\, a1[t]\, a2[t]\, a3[t] - 0.000401984\, a2[t]^2\, a3[t] + \\
&\quad 0.000260163\, a0[t]\, a3[t]^2 - 0.000584369\, a1[t]\, a3[t]^2 - 0.00056388\, a2[t]\, a3[t]^2 + \\
&\quad 0.000126588\, a3[t]^3 + 4.04419\times 10^{-6}\, A\, \omega^2\, \mathrm{Sin}[t\,\omega] + 4.52955\times 10^{-8}\, vL'[t] + \\
&\quad 2.98283\times 10^{-8}\, a0[t]\, vR'[t] - 9.02749\times 10^{-8}\, a1[t]\, vR'[t] - 1.10432\times 10^{-7}\, a2[t]\, vR'[t] + \\
&\quad 2.04963\times 10^{-8}\, a3[t]\, vR'[t] - 1.79724\times 10^{-9}\, a0''[t] - 2.70305\times 10^{-9}\, a1''[t] == 0, \\
&-0.000243088\, a0[t] + 0.000188002\, a0[t]^3 + 0.000635506\, a1[t] - 0.000547862\, a0[t]^2\, a1[t] + \\
&\quad 0.000263962\, a0[t]\, a1[t]^2 - 0.000300914\, a1[t]^3 + 0.00208006\, a2[t] - \\
&\quad 0.00159304\, a0[t]^2\, a2[t] + 0.00109689\, a0[t]\, a1[t]\, a2[t] - 0.00169386\, a1[t]^2\, a2[t] + \\
&\quad 0.00144927\, a0[t]\, a2[t]^2 - 0.00348448\, a1[t]\, a2[t]^2 - 0.00380408\, a2[t]^3 + \\
&\quad 0.000537321\, a3[t] - 0.000147552\, a0[t]^2\, a3[t] - 0.000328097\, a0[t]\, a1[t]\, a3[t] - \\
&\quad 0.000104453\, a1[t]^2\, a3[t] - 0.000946825\, a0[t]\, a2[t]\, a3[t] - \\
&\quad 0.000803968\, a1[t]\, a2[t]\, a3[t] - 0.00311996\, a2[t]^2\, a3[t] - \\
&\quad 0.000206983\, a0[t]\, a3[t]^2 - 0.00056388\, a1[t]\, a3[t]^2 - 0.00288122\, a2[t]\, a3[t]^2 - \\
&\quad 0.000640063\, a3[t]^3 - 1.47141\times 10^{-6}\, A\, \omega^2\, \mathrm{Sin}[t\,\omega] + 1.00685\times 10^{-7}\, vL'[t] + \\
&\quad 5.18485\times 10^{-8}\, a0[t]\, vR'[t] - 1.10432\times 10^{-7}\, a1[t]\, vR'[t] - 3.62055\times 10^{-7}\, a2[t]\, vR'[t] - \\
&\quad 1.07715\times 10^{-7}\, a3[t]\, vR'[t] + 6.28138\times 10^{-11}\, a0''[t] - 1.32778\times 10^{-9}\, a2''[t] == 0, \\
&0.000428694\, a0[t] - 0.000310899\, a0[t]^3 - 0.000132159\, a1[t] + 0.000235921\, a0[t]^2\, a1[t] - \\
&\quad 0.000215956\, a0[t]\, a1[t]^2 + 0.0000640047\, a1[t]^3 + 0.000537321\, a2[t] - \\
&\quad 0.000147552\, a0[t]^2\, a2[t] - 0.000328097\, a0[t]\, a1[t]\, a2[t] - 0.000104453\, a1[t]^2\, a2[t] - \\
&\quad 0.000473413\, a0[t]\, a2[t]^2 - 0.000401984\, a1[t]\, a2[t]^2 - 0.00103999\, a2[t]^3 + \\
&\quad 0.00117907\, a3[t] - 0.00121384\, a0[t]^2\, a3[t] + 0.000520326\, a0[t]\, a1[t]\, a3[t] - \\
&\quad 0.000584369\, a1[t]^2\, a3[t] - 0.000413966\, a0[t]\, a2[t]\, a3[t] - \\
&\quad 0.00112776\, a1[t]\, a2[t]\, a3[t] - 0.00288122\, a2[t]^2\, a3[t] - 0.00148094\, a0[t]\, a3[t]^2 + \\
&\quad 0.000379765\, a1[t]\, a3[t]^2 - 0.00192019\, a2[t]\, a3[t]^2 - 0.00129405\, a3[t]^3 + \\
&\quad 5.5338\times 10^{-7}\, A\, \omega^2\, \mathrm{Sin}[t\,\omega] - 4.04297\times 10^{-8}\, vL'[t] - 8.26299\times 10^{-8}\, a0[t]\, vR'[t] + \\
&\quad 2.04963\times 10^{-8}\, a1[t]\, vR'[t] - 1.07715\times 10^{-7}\, a2[t]\, vR'[t] - \\
&\quad 2.14882\times 10^{-7}\, a3[t]\, vR'[t] - 5.28213\times 10^{-10}\, a0''[t] - 5.17574\times 10^{-10}\, a3''[t] == 0, \\
&1.36672\times 10^{-7}\, a0[t]\, a0'[t] - 2.98283\times 10^{-8}\, a1[t]\, a0'[t] - 5.18485\times 10^{-8}\, a2[t]\, a0'[t] + \\
&\quad 8.26299\times 10^{-8}\, a3[t]\, a0'[t] - 2.98283\times 10^{-8}\, a0[t]\, a1'[t] + \\
&\quad 9.02749\times 10^{-8}\, a1[t]\, a1'[t] + 1.10432\times 10^{-7}\, a2[t]\, a1'[t] - 2.04963\times 10^{-8}\, a3[t]\, a1'[t] - \\
&\quad 5.18485\times 10^{-8}\, a0[t]\, a2'[t] + 1.10432\times 10^{-7}\, a1[t]\, a2'[t] + 3.62055\times 10^{-7}\, a2[t]\, a2'[t] + \\
&\quad 1.07715\times 10^{-7}\, a3[t]\, a2'[t] + 8.26299\times 10^{-8}\, a0[t]\, a3'[t] - 2.04963\times 10^{-8}\, a1[t]\, a3'[t] + \\
&\quad 1.07715\times 10^{-7}\, a2[t]\, a3'[t] + 2.14882\times 10^{-7}\, a3[t]\, a3'[t] - 4.36504\times 10^{-8}\, vR''[t] == 0, \\
&-4.27271\times 10^{-8}\, a0'[t] - 4.52955\times 10^{-8}\, a1'[t] - 1.00685\times 10^{-7}\, a2'[t] + \\
&\quad 4.04297\times 10^{-8}\, a3'[t] - 2.18254\times 10^{-8}\, vL''[t] == 0\}
\end{aligned}
$$

```
PP = MatrixForm[VV1];
P1e = PP[[1, 1]];
P2e = PP[[1, 2]];
P3e = PP[[1, 3]];
P4e = PP[[1, 4]];
P1m = P1e[[1]];
P2m = P2e[[1]];
P3m = P3e[[1]];
P4m = P4e[[1]];

V1Lk = PP[[1, 5]];
V1Rk = PP[[1, 6]];
Vrm = V1Lk[[1]];
Vlm = V1Rk[[1]];
vlf = -Coefficient[Vlm, vL''[t]];
vrf = -Coefficient[Vrm, vR''[t]];
```

$$\text{Vint} = \begin{pmatrix} \text{Expand}\left[\frac{1}{\text{vlf}}\left(\text{Vlm} + \text{vlf vL''[t]} - \frac{\text{vL'[t]}}{R_{1l}}\right)\right] \\ \text{Expand}\left[\frac{1}{\text{vrf}}\left(\text{Vrm} + \text{vrf vR''[t]} - \frac{\text{vR'[t]}}{R_{1r}}\right)\right] \end{pmatrix} \text{ // Simplify}$$

$$\left\{\left\{0. - 1.95768\, a0'[t] - 2.07536\, a1'[t] - 4.6132\, a2'[t] + 1.85242\, a3'[t] - \frac{4.58182 \times 10^{7}\, vL'[t]}{R_{1l}}\right\},\right.$$

$$\left\{0. - 1.18781\, a2[t]\, a0'[t] + 1.89299\, a3[t]\, a0'[t] + 2.52992\, a2[t]\, a1'[t] - 0.469557\, a3[t]\, a1'[t] + 8.29442\, a2[t]\, a2'[t] + 2.46767\, a3[t]\, a2'[t] + a1[t]\,(-0.683345\, a0'[t] + 2.06813\, a1'[t] + 2.52992\, a2'[t] - 0.469557\, a3'[t]) + 2.46767\, a2[t]\, a3'[t] + 4.92279\, a3[t]\, a3'[t] + a0[t]\,(3.13107\, a0'[t] - 0.683345\, a1'[t] - 1.18781\, a2'[t] + 1.89299\, a3'[t]) - \frac{2.29093 \times 10^{7}\, vR'[t]}{R_{1r}}\right\}\Bigg\}$$

```
M = ( -Coefficient[P1m, a0''[t]]  -Coefficient[P1m, a1''[t]]  -Coefficient[P1m, a2''[t
      -Coefficient[P2m, a0''[t]]  -Coefficient[P2m, a1''[t]]                0
      -Coefficient[P3m, a0''[t]]                0              -Coefficient[P3m, a2''[t
      -Coefficient[P4m, a0''[t]]                0                           0

Pint =
   ( P1m + M[[1, 1]] a0''[t] + M[[1, 2]] a1''[t] + M[[1, 3]] a2''[t] + M[[1, 4]] a3''[t]
                     P2m + M[[2, 1]] a0''[t] + M[[2, 2]] a1''[t]
                     P3m + M[[3, 1]] a0''[t] + M[[3, 3]] a2''[t]
                     P4m + M[[4, 1]] a0''[t] + M[[4, 4]] a3''[t]                        );

VV3 = Expand[LinearSolve[M, Pint]]
```

```
{{716023. a0[t] - 489229. a0[t]^3 - 574962. a1[t] +
   603849. a0[t]^2 a1[t] - 563015. a0[t] a1[t]^2 + 263872. a1[t]^3 -
   2.00316×10^6 a2[t] + 1.80187×10^6 a0[t]^2 a2[t] - 1.90334×10^6 a0[t] a1[t] a2[t] +
   1.59926×10^6 a1[t]^2 a2[t] - 2.52459×10^6 a0[t] a2[t]^2 + 3.44769×10^6 a1[t] a2[t]^2 +
   3.83676×10^6 a2[t]^3 - 1.18746×10^6 a3[t] + 255426. a0[t]^2 a3[t] +
   381518. a0[t] a1[t] a3[t] + 444975. a1[t]^2 a3[t] + 539987. a0[t] a2[t] a3[t] +
   1.65861×10^6 a1[t] a2[t] a3[t] + 4.64469×10^6 a2[t]^2 a3[t] + 206090. a0[t] a3[t]^2 +
   420993. a1[t] a3[t]^2 + 3.57555×10^6 a2[t] a3[t]^2 + 1.27945×10^6 a3[t]^3 +
   217.584 A ω^2 Sin[t ω] + 105.283 vL'[t] - 125.195 a0[t] vR'[t] +
   114.396 a1[t] vR'[t] + 391.575 a2[t] vR'[t] + 211.782 a3[t] vR'[t]},
 {-520108. a0[t] + 363191. a0[t]^3 + 586009. a1[t] - 565969. a0[t]^2 a1[t] +
   431019. a0[t] a1[t]^2 - 273068. a1[t]^3 + 1.56699×10^6 a2[t] -
   1.40074×10^6 a0[t]^2 a2[t] + 1.46082×10^6 a0[t] a1[t] a2[t] -
   1.39731×10^6 a1[t]^2 a2[t] + 1.88148×10^6 a0[t] a2[t]^2 - 2.91899×10^6 a1[t] a2[t]^2 -
   2.98073×10^6 a2[t]^3 + 740644. a3[t] - 82551.5 a0[t]^2 a3[t] -
   413456. a0[t] a1[t] a3[t] - 224825. a1[t]^2 a3[t] - 480414. a0[t] a2[t] a3[t] -
   1.18008×10^6 a1[t] a2[t] a3[t] - 3.23694×10^6 a2[t]^2 a3[t] -
   40780.2 a0[t] a3[t]^2 - 496104. a1[t] a3[t]^2 - 2.58597×10^6 a2[t] a3[t]^2 -
   803868. a3[t]^3 + 1351.49 A ω^2 Sin[t ω] - 53.2451 vL'[t] + 94.2767 a0[t] vR'[t] -
   109.459 a1[t] vR'[t] - 301.21 a2[t] vR'[t] - 133.23 a3[t] vR'[t]},
 {-149206. a0[t] + 118447. a0[t]^3 + 451424. a1[t] - 384049. a0[t]^2 a1[t] +
   172165. a0[t] a1[t]^2 - 214147. a1[t]^3 + 1.47181×10^6 a2[t] -
   1.11454×10^6 a0[t]^2 a2[t] + 736066. a0[t] a1[t] a2[t] -
   1.20005×10^6 a1[t]^2 a2[t] + 972071. a0[t] a2[t]^2 - 2.46119×10^6 a1[t] a2[t]^2 -
   2.68349×10^6 a2[t]^3 + 348502. a3[t] - 99043.5 a0[t]^2 a3[t] -
   229054. a0[t] a1[t] a3[t] - 57617.2 a1[t]^2 a3[t] - 687545. a0[t] a2[t] a3[t] -
   527034. a1[t] a2[t] a3[t] - 2.13004×10^6 a2[t]^2 a3[t] - 146137. a0[t] a3[t]^2 -
   404763. a1[t] a3[t]^2 - 2.00081×10^6 a2[t] a3[t]^2 - 421528. a3[t]^3 -
   1097.88 A ω^2 Sin[t ω] + 80.8103 vL'[t] + 33.1264 a0[t] vR'[t] -
   77.7589 a1[t] vR'[t] - 254.153 a2[t] vR'[t] - 71.1054 a3[t] vR'[t]},
 {97534.6 a0[t] - 101400. a0[t]^3 + 331438. a1[t] - 160440. a0[t]^2 a1[t] +
   157342. a0[t] a1[t]^2 - 145634. a1[t]^3 + 3.08249×10^6 a2[t] -
   2.124×10^6 a0[t]^2 a2[t] + 1.30855×10^6 a0[t] a1[t] a2[t] - 1.83395×10^6 a1[t]^2 a2[t] +
   1.66181×10^6 a0[t] a2[t]^2 - 4.29523×10^6 a1[t] a2[t]^2 - 5.92498×10^6 a2[t]^3 +
   3.48994×10^6 a3[t] - 2.60593×10^6 a0[t]^2 a3[t] + 615956. a0[t] a1[t] a3[t] -
   1.58318×10^6 a1[t]^2 a3[t] - 1.35091×10^6 a0[t] a2[t] a3[t] -
   3.87164×10^6 a1[t] a2[t] a3[t] - 1.0307×10^7 a2[t]^2 a3[t] -
   3.07165×10^6 a0[t] a3[t]^2 + 304093. a1[t] a3[t]^2 - 7.35903×10^6 a2[t] a3[t]^2 -
   3.80597×10^6 a3[t]^3 + 847.124 A ω^2 Sin[t ω] - 185.562 vL'[t] - 31.8795 a0[t] vR'[t] -
   77.1471 a1[t] vR'[t] - 607.739 a2[t] vR'[t] - 631.308 a3[t] vR'[t]}}
```

```
AbaPotlink = ( Coefficient[VV3[[1, 1]], a0[t]] /. {a1[t] → 0, a2[t] → 0, a3[t] → 0, vR'[t]
               Coefficient[VV3[[2, 1]], a0[t]] /. {a1[t] → 0, a2[t] → 0, a3[t] → 0, vR'[t]
               Coefficient[VV3[[3, 1]], a0[t]] /. {a1[t] → 0, a2[t] → 0, a3[t] → 0, vR'[t]
               Coefficient[VV3[[4, 1]], a0[t]] /. {a1[t] → 0, a2[t] → 0, a3[t] → 0, vR'[t]
                                   Coefficient[Vint[[1, 1]], a0'[t]]
                                Coefficient[Vint[[2, 1]], a2[t] a0'[t]] )
```

{{716023., -489229., -574962., 603849., -563015., 263872.,
$-2.00316\times10^{6}$, $1.80187\times10^{6}$, $-1.90334\times10^{6}$, $1.59926\times10^{6}$, $-2.52459\times10^{6}$,
$3.44769\times10^{6}$, $3.83676\times10^{6}$, $-1.18746\times10^{6}$, 255426., 381518., 444975.,
539987., $1.65861\times10^{6}$, $4.64469\times10^{6}$, 206090., 420993., $3.57555\times10^{6}$,
$1.27945\times10^{6}$, 217.584, 105.283, -125.195, 114.396, 391.575, 211.782},
{-520108., 363191., 586009., -565969., 431019., -273068., $1.56699\times10^{6}$,
$-1.40074\times10^{6}$, $1.46082\times10^{6}$, $-1.39731\times10^{6}$, $1.88148\times10^{6}$, $-2.91899\times10^{6}$,
$-2.98073\times10^{6}$, 740644., -82551.5, -413456., -224825., -480414.,
$-1.18008\times10^{6}$, $-3.23694\times10^{6}$, -40780.2, -496104., $-2.58597\times10^{6}$,
-803868., 1351.49, -53.2451, 94.2767, -109.459, -301.21, -133.23},
{-149206., 118447., 451424., -384049., 172165., -214147., $1.47181\times10^{6}$,
$-1.11454\times10^{6}$, 736066., $-1.20005\times10^{6}$, 972071., $-2.46119\times10^{6}$,
$-2.68349\times10^{6}$, 348502., -99043.5, -229054., -57617.2, -687545.,
-527034., $-2.13004\times10^{6}$, -146137., -404763., $-2.00081\times10^{6}$,
-421528., -1097.88, 80.8103, 33.1264, -77.7589, -254.153, -71.1054},
{97534.6, -101400., 331438., -160440., 157342., -145634., $3.08249\times10^{6}$,
$-2.124\times10^{6}$, $1.30855\times10^{6}$, $-1.83395\times10^{6}$, $1.66181\times10^{6}$, $-4.29523\times10^{6}$,
$-5.92498\times10^{6}$, $3.48994\times10^{6}$, $-2.60593\times10^{6}$, 615956., $-1.58318\times10^{6}$, $-1.35091\times10^{6}$,
$-3.87164\times10^{6}$, $-1.0307\times10^{7}$, $-3.07165\times10^{6}$, 304093., $-7.35903\times10^{6}$,
$-3.80597\times10^{6}$, 847.124, -185.562, -31.8795, -77.1471, -607.739, -631.308},
{-1.95768, -2.07536, -4.6132, 1.85242, $-4.58182\times10^{7}$, 0, 0, 0,
0, 0, 0, 0, 0, 0, 0, 0, 0, 0, 0, 0, 0, 0, 0, 0, 0, 0, 0, 0, 0, 0, 0, 0},
{-1.18781, 1.89299, 2.52992, -0.469557, 8.29442, 2.46767, -0.683345,
2.06813, 2.52992, -0.469557, 3.13107, -0.683345, -1.18781, 1.89299,
2.46767, 4.92279, $-2.29093\times10^{7}$, 0, 0, 0, 0, 0, 0, 0, 0, 0, 0, 0, 0, 0}}

```
Export["C:\\Users\\louis\\Dropbox\\projectData\\LongLong\\p1o3\\abaFitlink.csv",
 AbaPotlink]
```

C:\Users\louis\Dropbox\projectData\LongLong\p1o3\abaFitlink.csv

```
Coefficient[VV3[[1, 1]], a2[t] a0[t] a1[t]]
```

$-1.90334\times10^{6}$

```
vlf
```

$2.18254\times10^{-8}$

# Appendix E

# Matlab programs

## E.1 FEA integral computation

This code inputs the raw data from the FEA mode calculations and computes integrals of stress, strain and strain energy for the different sections of the beam:

```
umax=-4.81e-5; %maximum end deflection at buckled equilibrium
P0=1.3; %compressive load at equilibrium
d31=2*(-75e-12); %piezoelectric coupling constant
epsilon=7.526e-9; %dielectric constant

eq(:,:,1)=equ(5952:10271,3:end); %load the equilibrium position data into a matrix
eq(:,:,2)=equ(10283:14602,3:end); %third index indicates which section of the beam
Seq(:,:)=equ(1:5940,3:end); %1: piezo1 in bimorph
eq(:,:,4)=equ(14614:18933,3:end); %2: piezo2 in bimorph
%3: single layer piezo
eq(:,1,:)=eq(:,1,:)*1e-9; %correct volume %4: steel bimorph shim
```

```
Seq(:,1)=Seq(:,1)*1e-9;

const(:,:,1)=Const(5952:10271,3:end); %load the constrained data into a matrix
const(:,:,2)=Const(10283:14602,3:end);
Sconst(:,:)=Const(1:5940,3:end);
const(:,:,4)=Const(14614:18933,3:end);

const(:,1,:)=const(:,1,:)*1e-9; %correct volume

m(:,:,1,1)=M1(5952:10271,3:end); %stress/strain from first mode
m(:,:,2,1)=M1(10283:14602,3:end);
Sm(:,:,1)=M1(1:5940,3:end);
m(:,:,4,1)=M1(14614:18933,3:end);

m(:,:,1,2)=M2(5952:10271,3:end); %stress/strain from mode 2
m(:,:,2,2)=M2(10283:14602,3:end);
Sm(:,:,2)=M2(1:5940,3:end);
m(:,:,4,2)=M2(14614:18933,3:end);

m(:,:,1,3)=M3(5952:10271,3:end); %stress/strain from mode 3
m(:,:,2,3)=M3(10283:14602,3:end);
Sm(:,:,3)=M3(1:5940,3:end);
m(:,:,4,3)=M3(14614:18933,3:end);

a1=31.71; %load required for no deflection compression
a2=P0-a1; %load at equilibrium
```

```
%rB is the integral of the strain of the bimorph in the equilibrium configuration
rB=eq(:,1,1)'*eq(:,2,1)+eq(:,1,2)'*eq(:,2,2)+eq(:,1,4)'*eq(:,2,4);
rBabs=eq(:,1,1)'*abs(eq(:,2,1))+eq(:,1,2)'*abs(eq(:,2,2))+eq(:,1,4)'*abs(eq(:,2,4));
rB1=eq(:,1,1)'*m(:,1,1,1)+eq(:,1,2)'*m(:,1,2,1)+eq(:,1,4)'*m(:,2,4,1);
rB1abs=eq(:,1,1)'*abs(m(:,1,1,1))+eq(:,1,2)'*abs(m(:,1,2,1))+eq(:,1,4)'*abs(m(:,1,4,1));
rB2=eq(:,1,1)'*m(:,1,1,2)+eq(:,1,2)'*m(:,1,2,2)+eq(:,1,4)'*m(:,2,4,2);
rB2abs=eq(:,1,1)'*abs(m(:,1,1,2))+eq(:,1,2)'*abs(m(:,1,2,2))+eq(:,1,4)'*abs(m(:,1,4,2));
rB3=eq(:,1,1)'*m(:,1,1,3)+eq(:,1,2)'*m(:,1,2,3)+eq(:,1,4)'*m(:,2,4,3);
rB3abs=eq(:,1,1)'*abs(m(:,1,1,3))+eq(:,1,2)'*abs(m(:,1,2,3))+eq(:,1,4)'*abs(m(:,1,4,3));

%rS is the integral of the strain of the single layer in the equilibrium configuration
rS=Seq(:,1)'*Seq(:,2);
rSabs=Seq(:,1)'*abs(Seq(:,2));
rS1=Seq(:,1)'*Sm(:,1,1);
rS1abs=Seq(:,1)'*abs(Sm(:,1,1));
rS2=Seq(:,1)'*Sm(:,1,2);
rS2abs=Seq(:,1)'*abs(Sm(:,1,2));
rS3=Seq(:,1)'*Sm(:,1,3);
rS3abs=Seq(:,1)'*abs(Sm(:,1,3));

%seB/S are the strain energy at the equilibrium in the bimorph/single
seB=.5*(eq(:,1,1)'*(eq(:,2,1).*eq(:,8,1))+eq(:,1,2)'*(eq(:,2,2).*eq(:,8,2))+eq(:,1,4)'*(eq(:,2,4).*eq(:,8,4)
seS=.5*(Seq(:,1)'*(Seq(:,2).*Seq(:,8)));
se0=const(:,1,1)'*const(:,14,1)+const(:,1,2)'*const(:,14,2)+const(:,1,4)'*const(:,14,4)+Sconst(:,1)'*Sco
set=eq(:,1,1)'*eq(:,14,1)+eq(:,1,2)'*eq(:,14,2)+eq(:,1,4)'*eq(:,14,4)+Seq(:,1)'*Seq(:,14);
```

```
se1=eq(:,1,1)'*m(:,13,1,1)+eq(:,1,2)'*m(:,13,2,1)+eq(:,1,4)'*m(:,13,4,1)+Seq(:,1)'*Sm(:,13,1);
se2=eq(:,1,1)'*m(:,13,1,2)+eq(:,1,2)'*m(:,13,2,2)+eq(:,1,4)'*m(:,13,4,2)+Seq(:,1)'*Sm(:,13,2);
se3=eq(:,1,1)'*m(:,13,1,3)+eq(:,1,2)'*m(:,13,2,3)+eq(:,1,4)'*m(:,13,4,3)+Seq(:,1)'*Sm(:,13,3);

%V1/2 are the volume of the piezoelectric elements in the bimorph/single
V1=(epsilon-(d31^2)/(15.2e9))*(sum(eq(:,1,1))+sum(eq(:,1,2)));
V3=(epsilon-(d31^2)/(15.2e9))*sum(Seq(:,1));

%d's are the difference between the integral of the strain in the two
%piezoelectric layers of the bimorph
d0=(eq(:,1,1)'*eq(:,2,1))-(eq(:,1,2)'*eq(:,2,2)); %a0=1
d1=eq(:,1,1)'*m(:,1,1,1)-eq(:,1,2)'*m(:,1,2,1); %a0,a1=1
d2=eq(:,1,1)'*m(:,1,1,2)-eq(:,1,2)'*m(:,1,2,2); %a0,a2=1
d3=eq(:,1,1)'*m(:,1,1,3)-eq(:,1,2)'*m(:,1,2,3); %a0,a3=1

mS=8000*sum(eq(:,1,4))/.08; %mass per unit length of the steel shim
mP=3750*sum(eq(:,1,1))/.08; %mass/length of piezo material

matlink=[rB se0 se1 se3 d0 d1 V1 mS a1;rS set se2 d31*(15.2e9) d2 d3 V3 mP a2]
```

## E.2 Model Time Simulation

This program inputs the data generated via mathematica, and simulates the time evolution of the system under the sinusoidal forcing as indicated by the amplitude and frequency variables.

```
global w A Rlr Rll matlink zeta f tf;

Rlr=2200; %resistive load on right (single layer) piezo
Rll=2200; %resistive load on left (bimorph) piezo
load abaFitlink.csv; %load the Mathematica model
matlink=abaFitlink;
zeta=[1e-11 9e-8 2e-7 2e-5]; %damping

options=odeset('Jacobian',@beam_jacAbaCross,'BDF','on','RelTol',1e-4,'AbsTol',1e-6);

Input=6.5;
f=39.2;
w=f*2*pi;
A=sqrt(Input/(w^3));
tf=0;

Y0=[1 0 0 0 0 0 0 0 0 0];

[T,Y]=ode15s(@beam_fnAbaCross,[0 3],Y0,options);
length(T)
Tt=T;
Yt=Y;
tf=T(end);
tet=T(end);
yet=Y(end,:);
Y0=Y(end,:);
```

```
options=odeset('Jacobian',@beam_jacAbaCross,'BDF','on','RelTol',1e-4,'AbsTol',1e-6,'Events',@(t,Y)
poincare(t,Y,f));

for i = 1:10
[T, Y, te, ye, ie]=ode15s(@beam_fnAbaCross,[0 1],Y0,options);
Tt=[Tt;T+tf];
Yt=[Yt;Y];
tet=[tet;te+tf];
yet=[yet;ye];
Y0=Y(end,:);
tf=tf+T(end);
end
```

# Bibliography


[1] S. Roundy, P. K. Wright, and J. M. Rabaey. *Energy Scavenging for Wireless Sensor Networks; with Special Focus on Vibrations*. Kluwer Academic Publisher, Boston, 2004.

[2] Y.C. Shu, I.C. Lien. Efficiency of energy conversion for a piezoelectric power harvesting system. *J. Micromech. Microeng.*, 16:2429-2438, 2006.

[3] D. Guyomar, M. Lallart. Recent progress in piezoelectric conversion and energy havesting using nonlinear electronic interfaces and issues with small scale implementation. *Micromachines*, 2:274-294, 2011.

[4] M. Shafer, E. Garcia. The power and efficiency limits of piezoelectric energy harvesting. *Journal of Vibration and Acoustics* 136:021007-1, 2014.

[5] D. A. W. Barton, S. G. Burrow, and L. R. Clare. Energy harvesting from vibrations with a nonlinear oscillator. *J. Vibration and Acoustics*, 2010. DETC2009-86841.

[6] Y. Hu, H. Xue, J. Yang, and Q. Jiang. Nonlinear behavior of a piezoelectric power harvester near resonance. *IEEE Transactions on Ultrasonics, Ferroelectrics, and Frequency Control*, 53:1387–1391, 2006.

[7] L. Liu and F. G. Yuan. Nonlinear vibration energy harvester using diamagnetic levitation. *Appl. Phys. Lett.*, 98:203507, 2011.

[8] B. P. Mann and N. D. Sims. Energy harvesting from the nonlinear oscillations of magnetic levitation. *J. Sound Vibration*, 319:515–530, 2009.

[9] B. Marinkovic and H. Koser. Smart sand - a wide bandwidth vibration energy harvesting platform. *Appl. Phys. Lett.*, 94:103505, 2009.

[10] F. Peano, G. Coppa, C. Serazio, F. Peinetti, and A. D'angola. Nonlinear oscillations in a MEMS energy scavenger. *Math. Comp. Model.*, 43:1412–1423, 2006.

[11] R. Ramlan, M. J. Brennan, B. R. Mace, and I. Kovacic. Potential benefits of a non-linear stiffness in an energy harvesting device. *Nonlinear Dyn.*, 59:545–558, 2010.

[12] S. C. Stanton, C. C. McGehee, and B. P. Mann. Reversible hysteresis for broadband magnetopiezoelastic energy harvesting. *Appl. Phys. Lett.*, 95:174103, 2009.

[13] F. C. Moon. *Chaotic Vibrations: An Introduction for Applied Scientists and Engineers* Wiley, USA, 1987.

[14] J. Guckenheimer and P. Holmes. *Nonlinear Oscillations, Dynamical Systems, and Bifurcations of Vector Fields*. Springer-Verlag, New York, 1983.

[15] L. Gu, C. Livermore. Impact-driven, frequency up-converting coupled vibration energy harvesting device for low frequency operation *Smart Mater. Struct.*, 20:045004, 2011.

[16] H. Liu, C. Lee, T. Kobayashi, C. J. Tay, C. Quan. Piezoelectric MEMS-based wideband energy harvesting systems using a frequency-up-conversion cantilever stopper. *Sensors and Actuators A:Physical*, 186:242-248, 2012.

[17] S. Jung, K.-S. Yun. Energy-harvesting device with mechanical frequency-up conversion mechanism for increased power efficiency and wideband operation. *Appl. Phys. Lett.*, 96:111906, 2010.

[18] F. Cottone, H. Vocca, and L. Gammaitoni. Nonlinear Energy Harvesting. *Phys. Rev. Lett.*, 94:164102, 2009.

[19] M. Daqaq. Transduction of a bistable inductive generator driven by white and exponentially correlated gaussian noise. *J. Sound and Vibration*, 330:2554–2564, 2011.

[20] A. Erturk, J. Hoffmann, and D. J. Inman. A piezomagnetoelastic structure for broadband vibration energy harvesting. *Appl. Phys. Lett.*, 94:254102, 2009.

[21] M. Ferrari, V. Ferrari, M. Guizzetti, B. Ando, S. Baglio, and C. Trigona. Improved energy harvesting from wideband vibrations by nonlinear piezoelectric converters. *Procedia Chemistry*, 1:1203–1206, 2009.

[22] L. Gammaitoni, I. Neri, and H. Vocca. Nonlinear oscillators for vibration energy harvesting. *Appl. Phys. Lett.*, 94:164102, 2009.

[23] S.-M. Jung and K.-S. Yun. Energy harvesting device with mechanical frequency-up conversion mechanism for increased power efficiency and wideband operation. *Appl. Phys. Lett.*, 96:111906, 2010.

[24] M. A. Karami and D. J. Inman. Powering pacemakers from heartbeat vibrations using linear and nonlinear energy harvesters. *Appl. Phys. Lett.*, 100:042901, 2012.

[25] G. Litak, M. I. Friswell, and S. Adhikari. Magnetopiezoelastic energy harvesting driven by random excitations. *Appl. Phys. Lett.*, 96:214103, 2010.

[26] B. P. Mann and B. A. Owens. Investigations of a nonlinear energy harvester with a bistable potential well. *J. Sound Vib.*, 329:1215–1226, 2010.

[27] C. R. McInnes, D. G. Gorman, and M. P. Cartmell. Enhanced vibrational energy harvesting using nonlinear stochastic resonance. *J. Sound Vibration*, 318:655–662, 2008.

[28] J. Moehlis, B. E. DeMartini, J. L. Rogers, and K. L. Turner. Exploiting nonlinearity to provide broadband energy harvesting. *Proceedings of the ASME 2009 Dynamic Systems and Control Conference*, 2009. DSCC2009-2542.

[29] S. C. Stanton, C. C. McGehee, and B. P. Mann. Nonlinear dynamics for broadband energy harvesting: Investigation of a bistable piezoelectric inertial generator. *Physica D*, 239:640–653, 2010.

[30] R. L. Harne, K.W. Wang. A review of the recent research on vibration energy harvesting via bistable systems. *Smart Mater. Struct.*, 22:023001, 2013.

[31] M. I. Friswell, S. Faruque, O. Bilgen, S. Adihikari, A. W. Lees, G. Litak. Non-linear piezoelectric vibration energy harvesting from a vertical cantilever beam with tip mass. *J. Intell. Material Sys. Struct.*, 23:1505-1521, 2012.

[32] M. F. Daqaq, R. Masana, A. Erturk, D. Quinn. On the role of nonlinearities in vibratory energy harvesting: a critical review and discussion. *Applied Mechanics Reviews* 66:040801-1, 2014.

[33] A. J. Sneller, P. Cette, B. P. Mann. Experimental investigation of a post-buckled piezoelectric beam with an attached central mass used to harvest energy. *Proc. IMechE Vol. 225 Part 1:J. Systems and Control Engr.* 225:497, 2011.

[34] A. Alomari, A. Batra. Experimental and Modelling study of a piezoelectric energy harvester unimorph cantilever arrays. *Sensors & Transducers* 192:37-43, 2015.

[35] I. Chun, H.-W. Lee, K.-H. Kwon. Micro electro-mechanical system piezoelectric cantilever array for a broadband vibration energy harvester. *J. Nanosci. Nanotech.* 14(12):9253-7, 2014.

[36] S. Zhengguo, L. Dongling, W. Zhiyu, Z. Xingqiang. The fabrication of vibration energy harvester arrays based on AIN piezoelectric film. *Journal of Semiconductors* 34(11):114013-1. 2013.

[37] D. Quinn, A. L. Triplett, L. A. Bergman, A. F. Vakakis. Comparing linear and essentially nonlinear vibration-based energy harvesting. *J. Vib. Acoust.* 133,011001: 2010.

[38] A. Erturk, D.J. Inman. *Piezoelectric Energy Harvesting.* Wiley, UK, 2011.

[39] F. Cottone, L. Gammaitoni, H. Vocca, M. Ferrari. Piezoelectric buckled beams for random vibration energy harvesting. *Smart Mater. Struct.*, 96:214103, 2012.

[40] S. A. Emam. A Theoretical and Experimental Study of Nonlinear Dynamics of Buckled Beams *Virginia Tech* Dissertation, 2007.

[41] A.H. Nayfeh, W. Kreider, T.J. Anderson. Investigation of natural frequencies and mode shapes of buckled beams. *AIAA Journal*, 6:33, 1995.

[42] R. Masana and M.F. Daqaq. Electromechanical modeling and nonlinear analysis of axially loaded energy harvesters *J. Vib. Acoust.*, 133:011007, 2010.

[43] L. Gammaitoni, I. Neri, and H. Vocca. Nonlinear oscillators for vibration energy havesting. *Appl. Phys. Lett.*, 94:164102, 2010.

[44] Standards Committee of the IEEE Ultrasonics, Ferroelectrics, and Frequency Control Society. *IEEE Standard on Piezoelectricity*, IEEE, New York, 1987.

[45] H. F. Tiersten. *Linear Piezoelectric Plate Vibrations* Plenum Press, New York, 1969.

[46] R. C. McMeeking. Unpublished notes on solid mechanics, from personal discussion. 2013.

[47] C. Fox. *An introduction to the calculus of variations* Courier Dover Publications, 1987.

[48] www.advancedcerametrics.com

[49] D. G. Aronson, M. A. Chory, G. R. Hall, and R. P. McGehee. Bifurcations from an invariant circle for two-parameter families of maps of the plane: a computer-assisted study. *Commun. Math. Phys.*, 83:303–354, 1982.

[50] J. Moehlis and E. Knobloch. Wrinkled tori and bursts due to resonant temporal forcing. *Phisica D*, 211:347–376, 2001.

[51] ABAQUS Documentation. Dassault Systems, *Providence, Rhode Island*, 2014.

[52] R. Szilard. *Theory and Analysis of Plates: Classical and Numerical Methods* Prentice-Hall Inc, *Englewood Cliffs, New Jersey*, 1974.

[53] Z. Levnajić, I. Mezić. Ergodic theory and visualization. I. Mesochronic plots for visualization of ergodic partition and invariant sets. *Chaos* 20:033114, 2010.

[54] E. Ott. *Chaos in Dynamical Systems* Cambridge University Press, USA, 1994.

[55] E. J. Doedel,T. F. Fairgrieve,B. Sandstede, A. R. Champneys, Y. A. Kuznetsov, X. Wang. AUTO-07P: Continuation and bifurcation software for ordinary differential equations. www.dam.brown.edu/people/sandsted/auto/auto07p.pdf, 2007.

[56] Predrag Cvitanović. *Universality in Chaos* CRC Press, USA, 1989.

[57] C. Grebogi, E. Ott, J.A. Yorke. Crises, sudden changes in chaotic attractors and transient chaos. *Physica D* 181-200, 1983.

[58] S. Roundy, P.K. Wright, J. Rabaey. A study of low level vibrations as a power source for wireless sensor nodes. *Comput. Commun.*, 26:1131-44, 2003.

[59] Y. Zhu, J. Zu, W. Su. Broadband energy harvesting through a piezoelectric beam subjected to dynamic compressive loading. *Smart Mater. Struct.*, 22:045007, 2013.

[60] S.B. Kim, J. Park, S.H. Kim, H. Ahn, H.C. Wikle, D.J. Kim. Modeling and evaluation of $d_{33}$ mode piezoelectric energy harvesters. *J. Micromech. Microeng.*, 22:105013, 2012.

[61] A.F. Arrieta, T. Delpero, A.E. Bergamini, P. Ermanni. Broadband vibration energy harvesting based on cantilevered piezoelectric bi-stable composites. *Appl. Phys. Lett.*, 102:173904, 2013.

[62] Y. Hu, Y. Xu. A wideband vibration energy harvester based on a folded asymmetric gapped cantilever. *Appl. Phys. Lett.*, 104:053902, 2014.

[63] C. Xu, Z. Liang, B. Ren, W. Di, H. Luo, D. Wang, K. Wang, Z. Chen. Bi-stable energy harvesting based on a simply supported piezoelectric buckled beam. *Appl. Phys. Lett.*, 114:114507, 2013.

[64] X. Gao, W.H. Shih, W.Y. Shih. Vibration energy harvesting using piezoelectric unimorph cantilevers with unequal piezoelectric and nonpiezoelectric lengths. *Appl. Phys. Lett.*, 97:233503, 2010.

[65] L. Van Blarigan, P. Danzl, J. Moehlis. A broadband vibrational energy harvester. *Appl. Phys. Lett.*, 100:253904, 2012.

[66] S. Roundy, P.K. Wright, and J.M. Rabey. Energy Scavenging for Wireless Sensor Networks; with Special Focus on Vibrations. *Kluwer Academic Publisher*, Boston, 2004.

[67] G. Litak, M.I. Friswell, and S. Adhikari. Magnetopiezoelastic energy harvesting driven by random excitations. *Appl. Phys. Lett.*, 96:214103, 2010.

[68] A. Erturk, J. Hoffmann, and D.J. Inman. A piezomagnetoelastic structure for broadband vibration energy harvesting. *Appl. Phys. Lett.*, 94:254102, 2010.

[69] J. Moehlis, B. E. DeMartini, J. L. Rogers, and K. L. Turner. Exploiting nonlinearity to provide broadband energy harvesting. *Proceedings of the ASME 2009 Dynamic Systems and Control Conference*, 2009. DSCC2009-2542.

[70] L. Van Blarigan, J. Moehlis, R. McMeeking. Low dimensional modeling of a non-uniform, buckled piezoelectric beam for vibrational energy harvesting. *Smart Mater. Struct* 24:065012, 2015.

[71] Y. Hu, H. Xue, and H. Hu. A piezoelectric power harvester with adjustable frequency through axial preloads. *Smart Materials and Structures*, 16:1961–1966, 2007.

[72] F. Cottone, H. Vocca, and L. Gammaitoni. Nonlinear energy harvesting. *Phys. Rev. Lett.*, 102:080601, 2009.

[73] A. Erturk and D. J. Inman. Broadband piezoelectric power generation on high-energy orbits of the bistable Duffing oscillator with electromechanical coupling. *J. Sound and Vibration*, 330:2339–2353, 2011.

[74] D. D. Quinn, A. L. Triplett, A. F. Vakakis, and L. A. Bergman. Energy harvesting from impulsive loads using internal essential nonlinearities. *J. Vib. Acoust.*, 133:011004, 2011.